



**Search for Long-Lived Neutral Particles decaying to  
Photons and Missing Transverse Energy in  $pp$  Collisions at  
 $\sqrt{S} = 8$  TeV**

A DISSERTATION  
SUBMITTED TO THE FACULTY OF THE GRADUATE SCHOOL  
OF THE UNIVERSITY OF MINNESOTA  
BY

**Tambe Ebai Norbert**

IN PARTIAL FULFILLMENT OF THE REQUIREMENTS  
FOR THE DEGREE OF  
Doctor of Philosophy

**Prof. Yuichi Kubota**

**August, 2015**

**© Tambe Ebai Norbert 2015  
ALL RIGHTS RESERVED**

# Acknowledgements

# Dedication

What ever it is that doesnt workout, get up...I think youve got to realized that there is no personal ambition you have which can be extinguished by anybody else...Only YOU by giving up your dreams can extinguish them. And if your dreams doesnt work out EXACTLY like you intended, it will still take you someplace interesting and you will make a DIFFERENCE. So, DONT be AFRAID TO FAIL because you probably will whether you are afraid to or not and it's scary. You just gotta get out. The world belongs to tomorrow not yesterday. Dont give anybody else permission to take your life away, just keep living and keep giving and never make the perfect enemy the good.Never think that what Im doing is too little to make a difference, THAT'S NOT TRUE!, THAT'S NOT TRUE! Do something everyday. Someday, for all of us, it will be our last day and what would matter will be all the steps we took along the way and what they amounted to, NOT the home run we hit on day X. I wish you well.

US Pres Bill Clinton, Dallas, TX

*No, I have nothing against Mr. Einstein. He is a kind person and has done many good things, some of which will become part of the music. I will write to him and try to explain that the ether exists, and that its particles are what keep the Universe in harmony, and the life in eternity.*

Nikola Tesla

*The Universe is unbiased, she chooses to reveal herself to whomever she wants.*

Tambe E. Norbert

## Abstract

We have performed a search for events with delayed photons and large missing transverse momentum from the decay of neutral long-lived particles produced in proton-proton collisions with a center of mass energy,  $\sqrt{S} = 8$  TeV at the LHC. Capitalizing on the excellent timing resolution of the CMS electromagnetic calorimeter, we searched for events with delayed photons using the measured photon arrival time at the electromagnetic calorimeter. We observed a single event, consistent with our background expectations from the standard model and proceed to set limits on the cross section,  $\sigma_{\tilde{\chi}_1^0} > 0.02$  pb, for the production and decay of the lightest neutralino ( $\tilde{\chi}_1^0$ ) with mass,  $m_{\tilde{\chi}_1^0} \geq 235$  GeV/ $c^2$ , and lifetime,  $\tau_{\tilde{\chi}_1^0} \geq 35$  ns, according to a R-parity conserving Gauge Mediated Supersymmetry Breaking model. We show, for the first time, that using only timing information from the CMS electromagnetic calorimeter, the CMS detector is sensitive to neutralinos with lifetimes up to 40 ns and masses up to 260 GeV/ $c^2$ . A description of timing measurement by the electromagnetic calorimeter and its performance is presented.

# Contents

<b>Acknowledgements</b>	<b>i</b>
<b>Dedication</b>	<b>ii</b>
<b>Abstract</b>	<b>iii</b>
<b>List of Tables</b>	<b>viii</b>
<b>List of Figures</b>	<b>x</b>
<b>1 Introduction</b>	<b>1</b>
<b>2 Phenomenology of Long-Lived Particles</b>	<b>3</b>
2.1 The Standard Model . . . . .	3
2.1.1 Fermions . . . . .	3
2.1.2 Bosons . . . . .	4
2.1.3 Spontaneous Symmetry Breaking . . . . .	4
2.1.4 Beyond Standard Model Physics . . . . .	9
2.2 Supersymmetry . . . . .	12
2.2.1 The Minimal Supersymmetric Standard Model . . . . .	12
2.2.2 Gauge Mediated Supersymmetry Breaking Models . . . . .	17
2.3 Long-Lived Neutral Particles in GMSB Models . . . . .	19
2.3.1 Benchmark Scenario . . . . .	20
2.3.2 Signal Modeling . . . . .	25
2.3.3 Lightest Neutralino's Lifetime . . . . .	28

2.4	Previous Search Experiments . . . . .	32
<b>3</b>	<b>Hadron Collider and Detector</b>	<b>34</b>
3.1	Large Hadron Collider . . . . .	34
3.1.1	Overview . . . . .	34
3.1.2	Colliding Energy . . . . .	35
3.1.3	Luminosity . . . . .	36
3.1.4	LHC Bunch Structure . . . . .	37
3.2	Compact Muon Solenoid . . . . .	41
3.2.1	Overview . . . . .	41
3.2.2	Calorimeter . . . . .	43
3.2.3	Muon Chambers . . . . .	48
3.2.4	Triggering . . . . .	50
<b>4</b>	<b>Time Reconstruction and Resolution</b>	<b>51</b>
4.1	Electromagnetic Calorimeter Readout Electronics . . . . .	51
4.2	Time Reconstruction . . . . .	53
4.3	ECAL Time Performance from Test Beam . . . . .	55
4.3.1	ECAL Time Resolution . . . . .	55
4.4	ECAL Time Performance from Collision . . . . .	57
4.4.1	Time Calibrations . . . . .	58
4.4.2	Time Bias . . . . .	62
4.4.3	ECAL Time Performance With Z Bosons . . . . .	63
<b>5</b>	<b>Event Reconstruction</b>	<b>67</b>
5.1	Event Reconstruction Overview . . . . .	67
5.2	Supercluster Reconstruction . . . . .	67
5.3	Track and Vertex Reconstruction . . . . .	69
5.4	Photon and Electron Reconstruction . . . . .	70
5.5	Muon Reconstruction . . . . .	71
5.6	Particle Flow Algorithm . . . . .	72
5.7	Jet Reconstruction . . . . .	73
5.8	Missing Transverse Energy Reconstruction . . . . .	74

5.9	Anomalous Signals . . . . .	75
<b>6</b>	<b>Search for Long-Lived Neutral Particles</b>	<b>77</b>
6.1	Analysis Strategy . . . . .	77
6.1.1	Signal and Background Events . . . . .	77
6.1.2	Samples . . . . .	78
6.2	ECAL Timing . . . . .	80
6.2.1	Photon Time Measurement . . . . .	80
6.2.2	Satellite Bunches . . . . .	83
6.2.3	$E_T^{\text{miss}}$ Adjustments . . . . .	84
6.3	Event Selection . . . . .	85
6.3.1	Trigger Selection . . . . .	85
6.3.2	Offline Selection . . . . .	87
6.4	Background Estimation . . . . .	91
6.4.1	Collision Background . . . . .	92
6.4.2	Non-Collision Background . . . . .	93
6.4.3	Event Vetoing . . . . .	98
6.4.4	Background Estimation with ABDC Method . . . . .	101
6.4.5	Background Estimation Cross Check . . . . .	105
6.5	Systematic Studies . . . . .	111
6.6	Results . . . . .	113
<b>7</b>	<b>Statistical Analysis</b>	<b>115</b>
7.1	Limit Computation . . . . .	115
7.1.1	CLs Technique . . . . .	116
7.1.2	Statistical Test Formalism . . . . .	117
7.1.3	Test Statistics and $p$ -values . . . . .	119
<b>8</b>	<b>Limit Interpretation</b>	<b>123</b>
8.1	Signal Efficiency and Acceptance . . . . .	123
<b>9</b>	<b>Conclusion</b>	<b>128</b>
	<b>Bibliography</b>	<b>129</b>

<b>Appendix A. Glossary and Acronyms</b>	<b>134</b>
A.1 Glossary . . . . .	134
A.2 Acronyms . . . . .	135
A.3 Analysis How To and Data Samples . . . . .	136
A.3.1 Check Out Software Packages . . . . .	136
A.3.2 Data Samples . . . . .	136

# List of Tables

2.1	Fermions of the SM. Particle symbols are explained in text. . . . .	8
2.2	Interaction mediating vector bosons in the SM and the characteristic lifetime of the interaction. . . . .	8
2.3	Particles in the MSSM. SUSY particles (sparticles) have a “~” on the symbol . . . . .	13
2.4	Gauge and mass eigenstates of SUSY particles in the Minimal Supersymmetric SM (MSSM). . . . .	13
3.1	LHC operation parameter conditions during RUN 1, 2010-2013 . . . . .	40
3.2	CMS detector material, [29], and resolution(Time resolution: $N \approx 35$ ns, $\bar{C} \approx 0.070$ ns [49]) . . . . .	43
4.1	ECAL timing resolution absolute time and single precision for 2011 and 2012 of LHC Run 1. . . . .	66
6.1	Signal GMSB SPS8 Monte Carlo samples for different $\Lambda$ with $50\text{ cm} < c\tau < 1000\text{ cm}$ and Branching Ratios (BR). . . . .	79
6.2	The $\gamma +$ jets samples for $\hat{p}_T$ from $50\text{ GeV}/c$ to $800\text{ GeV}/c$ . . . . .	79
6.3	The photon identification and selection criteria used in this analysis . . . . .	90
6.4	The Jet ID and MET selection used in this analysis . . . . .	90
6.5	Summary of missing transverse expectation for events with out-of-time photons. . . . .	100
6.6	Definition of ABCD regions used for estimating non-collision background events in the signal region D. Events must satisfy the $\cancel{E}_T > 60\text{ GeV}$ selection requirement, which reduces collision background events significantly.	101

6.7	A,B,C,D,E,F regions used for estimating collision background events with out-of-time photons contamination the regions B and D of Table 6.6. Here, events must satisfy $\cancel{E}_T > 60 \text{ GeV}$ , selection requirement. . . . .	103
6.8	Event yields used in validating the ABCD background estimation method using 0 and 1-jet events sample. Halo/cosmic/spikes yields are obtained from tagged events. All events must pass photon, jet and $E_T^{\text{miss}}$ selection requirements. . . . .	104
6.9	Number of Z boson events with di-electron invariant mass, $76 < m_{e^+e^-} < 100 \text{ GeV}/c^2$ ) in the in-time and out-of-time Z boson samples. . . . .	108
6.10	Summary of systematic uncertainties for signal efficiency and background estimation in this analysis and applied to our final results. . . . .	112
6.11	Event yields used in our final background estimation for signal candidate events with at least a single photon and at least 2 jets, $\cancel{E}_T^\gamma > 60 \text{ GeV}$ , and $\cancel{E}_T > 60 \text{ GeV}$ . . . . .	114
8.1	Final number for $\Lambda = 180 \text{ TeV}$ GMSB SPS8 MC signal events events passing our selection cuts. . . . .	124
A.1	Acronyms . . . . .	135
A.2	Data samples and their corresponding integrated luminosity totaling $19.1 \text{ fb}^{-1}$ used in the our delayed photon search analysis . . . . .	136

# List of Figures

2.1	Higgs boson ‘‘Mexican hat’’ potential, $V(\phi^*\phi) = \mu^2(\phi^*\phi) + \lambda(\phi^*\phi)^2$ , which leads to spontaneous symmetry breaking with choice of parameters $\mu^2 < 0$ , $\lambda > 0$ . . . . .	7
2.2	Fermions and bosons and their interactions in the SM. All bosons (except the Higgs) mediate interactions between fermions. . . . .	7
2.3	Higgs mass contributions arising from the Higgs field coupling to fermions (a) and scalar (b) fields. . . . .	10
2.4	Cross section against SUSY sparticle mass for producing supersymmetric particles in different modes of interactions at the LHC. More supersymmetric particles are produced through strong interaction, $pp \rightarrow \tilde{g}\tilde{g}$ , processes than the any other process. . . . .	16
2.5	Feynman diagrams of Gravitino-Gaugino ( $(\lambda, A)$ ) ( <i>left</i> ) and Gravitino-Scalar ( $(\psi, \phi)$ ) ( <i>right</i> ) couplings. The coupling strength goes like $\frac{1}{\sqrt{F}}$ . .	19
2.6	SUSY mass spectra for benchmark SPS8 model: $\Lambda = 100$ TeV (left) and $\Lambda = 180$ TeV (right) with $C_{grav} = 93.5$ . SUSY particle mass increases with $\Lambda$ . . . . .	22
2.7	Feynmann diagrams for neutralino production from the cascade decay of a produced gluino ( <i>top</i> ) and squark ( <i>bottom</i> ). The final event has a single ( <i>left diagrams</i> ) or double photons ( <i>right diagrams</i> ) neutralino decay at LHC. . . . .	24
2.8	Number of photons (top left), Number of jets (top right) and $E_T^{\text{miss}}$ (bottom) for events with $\tilde{\chi}_1^0$ decay to $\gamma$ and $\tilde{G}$ for different $c\tau = 2000$ mm, 4000 mm, 6000 mm points of $\Lambda = 180$ TeV of the SPS8 model. A $\gamma+\text{jet}$ with $120 < p_T < 170$ GeV/c sample shown for comparison with the signal samples. . . . .	28

2.9	Neutralino transverse momentum ( $p_T^{\tilde{\chi}_1^0}$ ) distribution (top left) and transverse distance traveled (top right). Transverse momentum (bottom left) and time (bottom right) of photon from neutralino decay for different $\Lambda$ and $c\tau$ points in GMSB SPS8 model. . . . .	30
2.10	Schematic diagram showing $\tilde{\chi}_1^0 \rightarrow \gamma + \tilde{G}$ decay topology within the ECAL volume of the CMS detector ( <i>Left</i> ). The estimated photon arrival time at ECAL from the decay of $\tilde{\chi}_1^0$ in the SPS8 model with $m_{\tilde{\chi}_1^0} = 256 \text{ GeV}/c^2$ and $c\tau = 600 \text{ cm}$ ( <i>Right</i> ). . . . .	31
2.11	Neutralino lifetime and mass upper limit from ATLAS(left) and CMS(right) 7 TeV analysis with non-pointing photons and MET. . . . .	33
3.1	Schematic diagram showing the full Large hadron Collider. . . . .	35
3.2	Cumulative luminosity versus day delivered to (blue), and recorded by CMS (orange) during stable beams and for p-p collisions at 8 TeV center-of-mass energy in 2012. . . . .	37
3.3	Longitudinal Profile taken with Longitudinal Density Monitor (LDM) detector showing definition of Ghost/Satellite bunches with respect to main bunches. . . . .	38
3.4	(left)Arrival time distribution(red) of ATLAS MBTS for LHC fill 1533 during 2010 Pb-Pb run and LDM profile(black) for Beam2(same for Beam1). (Right) Timing of Clusters in the CMS endcap calorimeters for fill 1089:Left: EEP detector(left side of IP $z > 0$ ) Right: EEM detector( right side of IP, $z < 0$ ). Plots from ATLAS [38] and CMS, [39] . . . . .	39
3.5	CMS Detector showing the different subdetectors and their material. . .	42
3.6	CMS detector schematic view with definition of $x - y - z$ coordinates. .	42
3.7	Schematic diagram of CMS calorimetry system with HCAL enclosing ECAL in the Barrel and Endcap regions. . . . .	44
3.8	Layout of the CMS electromagnetic calorimeter showing the arrangement of crystal modules, supermodules in the barrel with the preshower in front of endcap with supercrystals. . . . .	49
3.9	Cross section view showing the coverage range of CMS sub-detectors and their longitudinal distance from the IP. . . . .	49

4.1	Schematic diagram of the ECAL electronics readout for a single channel (left) and the entire Trigger Tower (TT) or Front End (FE) Card (right). . . . .	53
4.2	(a) A measured ECAL pulse shape for a single channel. (b) $\mathbf{T} - \mathbf{T}_{\max}$ Vs $R(T)$ relationship whose inverse is $T(R)$ . Solid line is pulse shape from test beam while dots are typical 10 discrete samples corresponding to signal from proton-proton collision. . . . .	54
4.3	Difference in the time measurements as a function of $A_{eff}/\sigma_n$ of two crystals sharing an energy and belonging to the same electromagnetic shower obtained during electron test beam measurements. The single crystal energy scales for barrel (EB) and endcap (EE) is overlaid. The fitted results give $N = (35.1 \pm 0.2)$ ns and $\bar{C} = (20 \pm 4)$ ns. . . . .	57
4.4	<i>Top 3:</i> Time calibration maps showing the distribution of mean time for each channel/PbWO <sub>4</sub> crystal in EB (top) and EE (below: EE-(left), EE+(right)) before calibration. <i>Bottom 3:</i> Time calibration maps showing the distribution of mean time after calibration. After calibration most crystals have an average time of zero( <b>GREEN</b> ). . . . .	60
4.5	Distribution of mean time ( $\mu$ )[ <i>top row</i> ] and time deviation ( $\sigma$ )[ <i>bottom row</i> ] as a function of crystal energy for EB prior (left) and after (right) time bias corrections depending on energy have been applied. . . . .	63
4.6	Ecal time difference between the two reconstructed electrons in $Z \rightarrow e^-e^+$ decay. The electron time is the seed (crystal with highest energy deposit) time with additional correction due to the time of flight of the electron in EB and EE. . . . .	64
4.7	Ecal absolute time of a single reconstructed electron in $Z \rightarrow e^-e^+$ decay. The electron time is the seed (crystal with highest energy deposit)time of the electron in EB and EE. . . . .	65
4.8	Timing resolution from: <i>left:</i> Two most energetic crystals in the same FE electronics, <i>right:</i> Two most energetic crystals belonging to different FE electronics, as a function of effective amplitude( $A_{eff} = A_1A_2/\sqrt{A_1^2 + A_2^2}$ ) normalized to noise in EB. Both crystals are from reconstructed electrons in $Z \rightarrow e^-e^+$ events. . . . .	66

5.1	Superclustering algorithm direction (left) in the $(\eta, \phi)$ plane in EB and fraction (right) of electromagnetic shower energy coverage in a crystal energy matrix. . . . .	68
5.2	Illustration of muons from proton-proton collision, cosmic rays and beam halo. (a) Muons from collision propagating from the center and moving outwards, (b) Cosmic muons traveling through the detector leaving signals in opposite hemispheres of the muon system, (c) Cosmic muons leaving signals in the tracker and opposite hemispheres, (d) cosmic muons entering and leaving the detector without passing through the muon detector layers, (e) beam halo muons penetrating the detector and leaving signals in the endcaps and (f) Cosmic muons entering the detector through the endcap (EE) and leaving through the barrel (EB). This can happen in the reverse way; EB to EE. . . . .	72
6.1	Seed (black) and Average (blue) times as the measured photon time. . . . .	81
6.2	The $\chi^2$ Vs photon ECAL time plot showing spikes misidentified as photons have very large $\chi^2$ and negative ECAL time. The region of $\chi^2 > 4$ is mostly dominated by spikes events. . . . .	82
6.3	ECAL time distributions of in-time photons from MC $\gamma +$ jets (blue) and data (red) samples before (left) and after (right) we adjusted the photon time from MC. . . . .	83
6.4	ECAL timing distribution of photons in barrel (EB), endcap (EE) and all of ECAL (ALL ECAL) with $p_T > 50$ GeV from data. A 2.5 ns delay timing structure is observed in endcaps. . . . .	84
6.5	Our HLT trigger efficiency turn-on curves in event $\cancel{E}_T$ (left) and photon $p_T$ (right). The $\gamma +$ jets samples require photon $p_T > 170$ GeV/c. . . . .	87
6.6	Comparing ECAL time distribution of events with different jet multiplicity from small sample of data and a single GMSB $\Lambda = 180$ TeV and $c\tau = 6000$ mm sample. Accepted photons must have $p_T > 60$ GeV and belong to barrel and encaps. . . . .	89
6.7	ECAL time against $\eta$ (left) and ECAL time against $\phi$ (right) for photons with $p_T > 60$ GeV from data. . . . .	91

6.8	ECAL time <i>vs</i> $\Delta\phi(\text{CSC Seg}, \gamma)$ (left) for in time (black) and out-of-time (red and blue) photons. Photon ECAL time $V.s \eta$ (right), expected halo-induced photon time is shown as two red lines. . . . .	95
6.9	Scatter plot showing $\Delta\eta(\text{DT Seg}, \gamma)$ against $\Delta\phi(\text{DT Seg}, \gamma)$ for out-of-time ( $t_\gamma > 2$ ns and $t_\gamma < -3$ ns) photons (right) compared to in-time( $ t_\gamma  < 1$ ns) photons (left). Cosmic photon candidates have small $\Delta\eta$ and $\Delta\phi$ . . . . .	96
6.10	Scatter plot of $\Delta\eta(\text{DT Seg}, \gamma)$ against $\Delta\phi(\text{DT Seg}, \gamma)$ for photons from pure cosmic muon data. Small $\Delta\eta$ and $\Delta\phi$ are cosmic photons. . . . .	96
6.11	<i>Number of crystals</i> belonging to a photon supercluster (left) plot for in-time photon candidates (black), spike-seeded photon candidates (magenta) and halo-induced photon candidates (red). The spike-seeded photon candidates are selected using a swiss-cross variable ( $1-E_4/E_1$ ) (right), shown comparing in-time photons ( $ t_\gamma  < 1.0$ ) to spike candidate sample selected using $S_{\text{Minor}}$ . . . . .	98
6.12	Photon ECAL time, for a data sample of 0 and 1-jet events, showing our tagging performance for non-collision background events. . . . .	99
6.13	Di-electron mass distribution (left) and the time (right) of the two electron candidates for the signal, $76 < m_{e^+e^-} < 100 \text{ GeV}/c^2$ , of Z boson sample. Events are from the <b>Single/DoubleElectron</b> data sample. . . . .	106
6.14	ECAL time $V.s \eta$ (top plots) and $V.s \phi$ (bottom plots) for electromagnetic particle candidates from <b>SinglePhoton</b> data sample (left) compared to electromagnetic particle candidates from the <b>Single/DoubleElectron</b> data sample (right). All electromagnetic particle candidates are in barrel. Most of the electromagnetic particles with “cross-shape” and at $\phi = 0, \pm\pi$ , are halo-induced photons. . . . .	107

6.15 Di-electron invariant mass and polynomial fit (red) for sideband sample ( $50 < m_{e^+e^-} < 76 \text{ GeV}/c^2$ and $100 < m_{e^+e^-} < 130 \text{ GeV}/c^2$ ). Di-electron invariant mass and polynomial fit (blue) for in-time ( $ t  < 2 \text{ ns}$ ) Z candidates ( <i>top right</i> ). Di-electron invariant mass and polynomial fit for out-of-time ( $t < -3 \text{ ns}$ ) Z candidates ( <i>bottom left</i> ). Di-electron invariant mass and polynomial fit for out-of-time ( $t > 3 \text{ ns}$ ) Z candidates ( <i>bottom right</i> ). The fits are used to estimated the number of true Z bosons in the int-time and out-of-time Z candidate samples. . . . .	110
7.1 Sampling distributions for $f(t_\mu \mu)$ showing how one extracts the $p$ -vlaues. left: is the using a analytic of the Asymptotic method and right: is from the HybridNew method. . . . .	120
7.2 Distribution of $p$ -vlaues showing how upper limit on $\mu$ is extracted for a given threshold probability. . . . .	122
8.1 The reconstruction and selection efficiency (left) $\times$ Acceptance ( $t > 3 \text{ ns}$ ) (right) against transverse decay length in laboratory frame for different $c\tau$ points. . . . .	124
8.2 Neutralino production cross section against proper delay length upper limit interpretation in SPS8 model. (Left) $\Lambda = 100 \text{ TeV}$ , (Right)(left) $\Lambda = 180 \text{ TeV}$ . . . . .	125
8.3 Neutralino production cross section against neutralino mass upper limit at 95% confidence levels interpretation in SPS8 model.(Left) $C\tau = 11000 \text{ mm}$ , (Right) $C\tau = 6000 \text{ mm}$ . . . . .	126
8.4 Neutralino two dimensional exclusion limit of neutralino mass ( $\Lambda$ ) against proper delay length upper limit interpretation in SPS8 model in the decay $\tilde{\chi}_1^0 \rightarrow \gamma + \tilde{G}$ with limits from previous experiments shown. . . . .	127

# Chapter 1

## Introduction

The search for a Long-Lived Neutral Particle (LLNP) produced in  $pp$  collisions at  $\sqrt{S} = 8$  TeV by the Large Hadron Collider (LHC) on data recorded by the Compact Muon Solenoid (CMS) detector is presented in this thesis.

The Standard Model (SM) describes the interactions of fundamental particles with unmatched precision and has been very successful in terms of all its predictions of new particles and their properties agreeing with experiments. However, there are strong indications that the SM is incomplete. For example, the SM does not include gravity in its formulation and describes only visible matter, which is about 5 times less abundant than the total matter in the universe. The rest of the matter in the universe is referred to as Dark Matter (DM) [1, 2, 3], because we have very little understanding of it.

There are many extensions to the SM where DM and other new phenomena are described. LLNPs, which are not described by the SM, are predicted to exist by many models generally referred to as Beyond the Standard Model (BSM) models. These LLNPs can decay into stable, neutral particles which are good candidates for DM particles and if they have low enough mass, may be produced and detected at the LHC. The signature for the decay of a LLNP, is the presence of Missing Transverse Energy (MET), which indicates the escape of an undetected candidate DM particle, and an electromagnetic particle, like a photon, in the same event. The combination of a late photon, which is detected late with respect to LHC  $pp$  collision times, and large MET is the central idea in the search presented in this thesis.

The LHC completed a successful first long operation in 2012. Data from  $pp$  collisions

during this period of operation (LHC RUN 1) was recorded by the CMS detector. The CMS detector was fully operational for nearly all of this period. The Electromagnetic Calorimeter (ECAL) recorded the arrival time and energy of electromagnetic particles produced from  $pp$  collisions with excellent resolution. This resolution was maintained through out the entire LHC RUN 1 by continuous energy and timing performance monitoring and calibration. The search for LLNPs in this data is presented here.

Understanding the signature of a LLNP in the CMS detector is provided by using samples of events generated in a Monte Carlo simulation of the production and decay of LLNPs.

This thesis is organized as follows: A brief introduction of the standard model, Supersymmetry (SUSY) and the description of GMSB models,[16], with LLNPs is presented in Chapters 2.

In Chapter 3, the LHC and CMS particle detector are described with an emphasis on the sub-detectors used in our search for LLNPs.

A description of the photon timing measurements made using the ECAL and its performance is discussed in Chapter 4, while the reconstruction of events and their constituent particles are described in Chapter 5, where the definition and measurement of quantities like MET and jets are presented.

Chapter 6 describes the search method in detail including the data samples used, observables, event selection requirements and background estimation techniques. The systematics arising from signal efficiency and acceptance in our signal event selection are also discussed in this chapter. In Chapter 7, we describe the statistical methods used to estimate the precision of the measurement.

Limits on the product of the production cross sections and the branching ratio for different lifetimes and masses of a LLNP is discussed in Chapter 8. The interpretation of our results in terms of the possible extensions to the SM by our analysis is also discussed in this chapter and in Chapter 9 the conclusions are presented.

## Chapter 2

# Phenomenology of Long-Lived Particles

### 2.1 The Standard Model

The Standard Model (SM) is a mathematical description of the fundamental components of matter and their interactions. Fermions are the building blocks of matter and their interaction is mediated by vector bosons. The SM describes the interactions of fermions through, the weak, electromagnetic and strong interactions but does not describe gravity. Fermions and bosons get their mass by interacting with a scalar boson in a process of spontaneous gauge symmetry breaking,[6].

#### 2.1.1 Fermions

Half-integer spin ( $\frac{1}{2}\hbar$ ) particles called *fermions* exist in nature, together with their anti-particles (particle with opposite charge), as either leptons ( $\ell$ ) or quarks ( $q$ ). Fermions come in 3 *generations* or *flavors* and are arranged in a mass hierarchy, where the third generation fermions are the heaviest. The third and second generation fermions are meta-stable decaying to the first generation fermions which are stable. The heaviest SM fermion, which is the **top** quark ( $t$ ) has a mass of  $m_t = 173 \text{ GeV}/c^2$ , and a lifetime of about  $10^{-24}$  seconds.

Quarks carry fractional electric charges and participate in weak and electromagnetic

interactions and also in strong interactions, since in addition to the electric charge and a *color* charge. Each generation of quarks is a pair of an “*up-type*” and a “*down-type*” quark. The *Up-type* quarks (**up** (u), **charm** (c), **top** (t)) have a charge of  $+\frac{2}{3}$ , while the *down-type* quarks (**down** (d), **strange** (s), **bottom** (b)) have a charge of  $-\frac{1}{3}$ . Quarks do not exist as free particles in nature but as bound states of quarks and anti-quarks in the form of composite particles called *Hadrons*.

Leptons on the other hand exist free in nature and come in pairs consisting of a given lepton flavor and its corresponding neutrino. Leptons from all 3 generations (**electron** (e), **muon** ( $\mu$ ), **tau** ( $\tau$ )) have a charge of  $-1$ , while their corresponding neutrinos (**electron neutrino** ( $\nu_e$ ), **muon neutrino** ( $\nu_\mu$ ), **tau neutrino** ( $\nu_\tau$ ) ) have a charge of  $0$ . Leptons can participate only in weak and electromagnetic interactions. In Table 2.1, we present a summary of the fermions in each generation arranged according to the SM.

### 2.1.2 Bosons

*Bosons* have integer spins and they exists in nature in two types: scalar ( $0\hbar$ ) and vector ( $1\hbar$ ) bosons. Vector bosons are responsible for mediating the interactions between fermions and the only scalar boson (Higgs boson), discovered so far, provides mass to both fermions and bosons.

The vector bosons  $W^\pm$  (charged) and  $Z$  (neutral) are massive and mediate the *weak* interactions, while the massless vector bosons: *photon* ( $\gamma$ ) and *8 gluons* (g) mediate the *electromagnetic* and *strong* interactions, respectively [6, 7]. A summary of the interactions in the SM and their corresponding mediating vector bosons is presented in Table 2.2. The characteristic lifetimes of a particle decay involving each of the interactions is also shown in the Table. The longest lifetimes are characteristic of the weak interactions, explained partly because the mediating vector bosons is massive or the interaction strength is weakest.

### 2.1.3 Spontaneous Symmetry Breaking

In the SM, the weak, electromagnetic and strong interactions can be described using *gauge* symmetries and a *conserved quantum number* associated to the symmetry. The

gauge symmetry of the SM is a combination of 3 different gauge symmetries

$$SU(3)_C \otimes SU(2)_L \otimes U(1)_Y. \quad (2.1)$$

where,  $SU(3)_C$  is the gauge symmetry describing strong interactions with *color* ( $C$ ) charge as its conserved quantum quantity. Quarks participate in strong interactions mediated by 8 gluons because of the color charge

$SU(2)_L \otimes U(1)_Y$  is the gauge symmetry describing the weak and electromagnetic interactions also known as the *electro-weak* interaction and the conserved quantum number derived from a combination of conserved quantum numbers: *isospin* ( $T_3$ ) of  $SU(2)_L$  and *hypercharge* ( $Y$ ) of  $U(1)_Y$  symmetry. After the spontaneous breaking of this electro-weak symmetry ( $SU(2)_L \otimes U(1)_Y \rightarrow U(1)_Q$ ), the resulting conserved quantum number describing the electromagnetic interaction which is based on the  $U(1)_Q$  symmetry, is the electric charge,  $Q$ . The electric charge is related to  $T_3$  and  $Y$  through the relation

$$Q = T_3 + \frac{Y}{2}. \quad (2.2)$$

Corresponding to the  $SU(2) \otimes U(1)$  symmetry, are 4 massless vector bosons or *eigen* states,  $W_\mu^{1,2,3}, B_\mu$ , which combine to form the physical electro-weak vector bosons or *mass* states,  $W^\pm, Z, \gamma$ . These mass states are related to the eigenstates through a rotation which is expressed as

$$W^\pm = \frac{W_\mu^1 \pm iW_\mu^2}{\sqrt{2}}, \quad \begin{pmatrix} \gamma \\ Z \end{pmatrix} = \begin{pmatrix} \cos \theta_w & \sin \theta_w \\ -\sin \theta_w & \cos \theta_w \end{pmatrix} \begin{pmatrix} B_\mu \\ W_\mu^3 \end{pmatrix} \quad (2.3)$$

The angle,  $\theta_w$ , known as the *Weinberg angle*, relates the physical electric charge,  $e$ , to the coupling strengths,  $g$  and  $g'$  of  $SU(2)_L$  and  $U(1)_Y$  gauge symmetries, respectively, in a relation given as  $e = g \sin \theta_w = g' \cos \theta_w$ . This angle is one of the input parameters of the SM and has been measured from experiments to be equal to 28.726 degrees, which is equal to the arc cosine of the ratio of the mass of the  $W$  boson to that of the  $Z$  boson.

According to the SM, the only way to realize the massive vector bosons and explain how fermions get their mass is through the *Higgs mechanism*, [8], and involves

spontaneously breaking the gauge symmetry of the SM, expressed as

$$SU(3)_C \otimes SU(2)_L \otimes U(1)_Y \xrightarrow{SSB \text{ into}} SU(3)_C \otimes U(1)_Q. \quad (2.4)$$

In the SM, spontaneous symmetry breaking is realized through the potential of a spin-0 complex scalar field called the *Higgs boson*. The Higgs boson takes the representation of an weak isospin *doublet*. Its potential,  $V(\phi^*, \phi) = \mu^2(\phi^*\phi) + \lambda(\phi^*\phi)^2$ , is written in terms of the Higgs field ( $\phi$ ) and its complex conjugate ( $\phi^*$ ), where  $\mu$  and  $\lambda$  are parameters. Among the many possible choices of configuration for this potential, only one particular configuration, represented by the choice of the parameters:  $\mu^2 < 0$  and  $\lambda > 0$ , such that the minimum value of this potential, or the *Vacuum Expectation Value* (VEV) of the Higgs field,  $|\phi_0| = \sqrt{\frac{-\mu^2}{\lambda}} = \nu = 246 \text{ GeV}$ , spontaneously breaks the  $SU(2)_L \otimes U(1)_Y$  symmetry into a  $U(1)$  symmetry. This particular configuration of the potential of the Higgs field is shown in Figure 2.1.

Fermions acquire their mass through their interaction with the Higgs field and the fermion's mass,  $m_f$ , is proportional to the strength of its interaction (Yukawa coupling  $\lambda_f$ ) with the Higgs field. The relationship between the masses of the fermions and the W,Z masses is given in Equation 2.5.

The massive vector bosons, Z and  $W^\pm$ , obtain their mass,  $m_Z = 91 \text{ GeV}/c^2$  and  $m_{W^\pm} = 80 \text{ GeV}/c^2$ , respectively, by engulfing or “*eating*” the available massless components (*Nambu-Goldstone bosons*) of the complex Higgs doublet. Out of the four scalar fields, only one physically massive scalar particle *Higgs boson* remains. The masses of the charge and neutral vector bosons, given in Equation 2.5, are connected through the cosine of the *Weinberg angle*.

$$m_f = \lambda_f \frac{\nu}{\sqrt{2}}, \quad \frac{m_{W^\pm}}{m_Z} = \frac{\frac{1}{2}\nu g}{\frac{1}{2}\nu\sqrt{g^2 + g'^2}} = \cos\theta_w \quad (2.5)$$

It took nearly 40 years for the Higgs boson to be discovered after its prediction in the 1960s. The Higgs boson was discovered at CERN on July 04, 2012, through its decay into two photons,  $H \rightarrow \gamma\gamma$ , and a pair of Z bosons,  $H \rightarrow ZZ$ , channels. Its mass has been measured to be,  $m_H = 125 \pm 0.21 \text{ GeV}/c^2$ . As shown in Figure 2.2, every SM particle interacts with the Higgs boson either directly or indirectly as in the case for photons

and gluons.

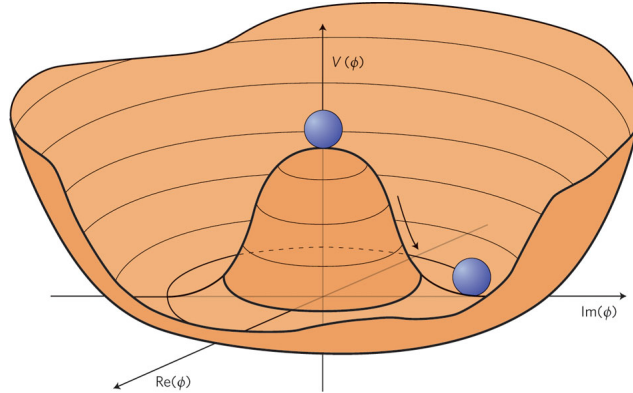


Figure 2.1: Higgs boson “Mexican hat” potential,  $V(\phi^*\phi) = \mu^2(\phi^*\phi) + \lambda(\phi^*\phi)^2$ , which leads to spontaneous symmetry breaking with choice of parameters  $\mu^2 < 0$ ,  $\lambda > 0$ .

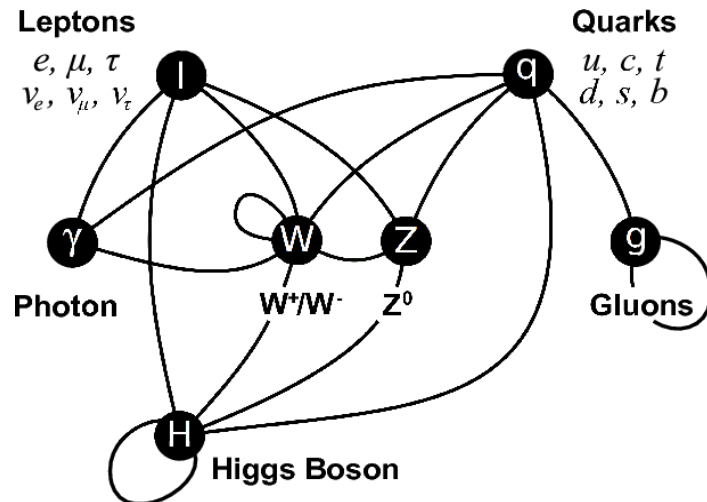


Figure 2.2: Fermions and bosons and their interactions in the SM. All bosons (except the Higgs) mediate interactions between fermions.

<b>Fermions</b>	<b>Generation</b>			<b>Charge</b>
	First	Second	Third	
Leptons	$\begin{pmatrix} e^- \\ \nu_e \end{pmatrix}$	$\begin{pmatrix} \mu^- \\ \nu_\mu \end{pmatrix}$	$\begin{pmatrix} \tau^- \\ \nu_\tau \end{pmatrix}$	$\begin{pmatrix} -1 \\ 0 \end{pmatrix}$
Quarks	$\begin{pmatrix} u \\ d \end{pmatrix}$	$\begin{pmatrix} c \\ s \end{pmatrix}$	$\begin{pmatrix} t \\ b \end{pmatrix}$	$\begin{pmatrix} +\frac{2}{3} \\ -\frac{1}{3} \end{pmatrix}$

Table 2.1: Fermions of the SM. Particle symbols are explained in text.

<b>Bosons</b>	<b>Interaction</b>	<b>Symmetry</b>	<b>Characteristic Lifetime</b>
$W^\pm, Z$	Weak	$SU(2)_L \otimes U(1)_Y$	$10^{-8}$ to $10^{-13}$ seconds
$\gamma$	Electromagnetic	$U(1)_Q$	$10^{-14}$ to $10^{-20}$ seconds
$g$	Strong	$SU(3)_C$	$< 10^{-22}$ seconds

Table 2.2: Interaction mediating vector bosons in the SM and the characteristic lifetime of the interaction.

### 2.1.4 Beyond Standard Model Physics

The Higgs boson is a crucial component in the formulation and experimental success of the SM, yet the SM itself provides no explanation for the above choice of parameters ( $\mu^2 < 0$  and  $\lambda > 0$ ) of the Higg's potential or whether there is only one type of Higgs field with which all fermions couple to obtain their mass. Some Beyond the Standard Model (BSM) models, like *Supersymmetry*, allow for the possibility of more than one Higgs field and predicts the existence of additional particles to those in the SM. The following are some of the reasons for the interest in BSM physics, particularly Supersymmetry:

#### The Hierarchy Problem

Predictions of the Higgs boson's mass,  $m_H^2$ , by the SM, include corrections to the Higgs boson's mass,  $\delta m_f^2$ , from its coupling with fermion. These corrections from first order interaction (1-loop level) of the Higgs boson with fermions are computed using the Feynman diagram shown in Figure 2.3(a) and given as

$$\delta m_f^2 = \frac{1}{16\pi^2} |\lambda_f|^2 \left( -2\Lambda^2 + 6m_f^2 \ln \left( \frac{\Lambda}{m_f} \right) + \dots \right) \quad (2.6)$$

where,  $\lambda_f$  is the coupling parameter of the Higgs boson to fermions with the interaction Lagrangian density written as  $\lambda_f H \bar{f} f$ .  $\Lambda$  represents an arbitrary high energy scale (of the order  $10^{18}$  GeV) known as the *cut-off* energy scale. Because  $\Lambda = 10^{18}$  GeV is very large, we would expect the correction to the Higgs boson's mass to also be very large eventually making the Higgs boson's mass,  $m_H^2$ , to be very large. However, the Higgs boson's mass measured from experiment is only about  $125$  GeV/c<sup>2</sup>. A dilemma thus arises, if one is to trust SM predictions of the Higgs boson's mass, why are all these large corrections to the Higgs boson's mass not observed in experiments? The SM cannot provide an explanation for this. This problem is known as the *Hierarchy problem*.



Figure 2.3: Higgs mass contributions arising from the Higgs field coupling to fermions (a) and scalar (b) fields.

SUSY, on the other hand, provides a plausible explanation as to why these corrections are not observed in experiments. In SUSY models, there are in addition to the scalar Higgs boson new supersymmetric scalar particles, which are yet to be observed, that can also couple to the Higgs field as shown in the 1-loop Feynman diagram in Figure 2.3(b). The contributions to the Higgs boson's mass from these new scalar supersymmetric particles,  $\delta m_S^2$ , is computed at the order of 1-loop and given as

$$\delta m_S^2 = \frac{1}{16\pi^2} |\lambda_S|^2 \left( \Lambda^2 - 2m_S^2 \ln \left( \frac{\Lambda}{m_S} \right) + \dots \right) \quad (2.7)$$

where  $\lambda_S$  is also the coupling constant of the Higgs field to the new scalar particle given as,  $\lambda_S H S \bar{S}$ . An interesting observation comparing Equations 2.6 to Equation 2.7, up to the  $\Lambda^2$ -terms is that their signs are different. The opposite sign corrections to the Higgs boson's mass cancel each other and as a result their net contribution to the Higgs mass,  $m_H^2$  is zero. This cancellation which happens at all orders of corrections is the reason why one does not observe very large Higgs boson mass from experiment.

### Dark Matter and Long-Lived Particles

There is ample evidence [1], that dark matter (matter which does not interact with light) exists in the universe, and if this form of matter is made of particles, then the lifetime of a dark matter particle must be comparable to the age of the universe. Furthermore, it must also be neutral. Such neutral stable particles are not part of the SM. Therefore, dark matter particles must certainly posses a new kind of interaction.

*Long-Lived Neutral Particles* (LLNP) which are meta-stable (particles that are stable for a period of time and then decay) and can decay into possible dark matter particles

through new kind of interactions also do not exist in the SM. These LLNPs are predicted, by BSM models, to have lifetimes longer than the characteristic lifetimes of particles and interactions in Table 2.2. In addition to Supersymmetry providing a possible explanation for stability of the Higgs boson's mass, it also predicts the existence of LLNPs, which can decay into dark matter candidate particles with lifetime beyond those of the SM [2, 3, 16, 4, 5, 18]. These LLNPs decay into dark matter candidate particles through new kind of interactions. Such predictions from Supersymmetry have motivated many of the studies of Supersymmetry as an interesting candidate among many models beyond the SM, in both theory and experiment. It is certainly a motivation for the study presented in this thesis.

## 2.2 Supersymmetry

Supersymmetry (SUSY) relates space-time symmetries (rotation and translation) to gauge symmetries ( $SU(3)_C \otimes SU(2)_L \otimes U(1)_Y$ ) [10, 11]. The generators of SUSY,  $Q$ , transform fermions to bosons and bosons to fermions;

$$Q|\text{Fermion}\rangle = |\text{Boson}\rangle, \quad Q|\text{Boson}\rangle = |\text{Fermion}\rangle, \quad (2.8)$$

and as a consequence, the fermions and their corresponding bosons have the same mass.

### 2.2.1 The Minimal Supersymmetric Standard Model

The *Minimal Supersymmetric Standard Model* (MSSM) uses only one SUSY generator,  $Q$ , in its formulation as an extension of the SM, to include the supersymmetric partners of the particles in the SM. The number of fundamental particles in the MSSM is obviously doubled, however, the gauge symmetries are the same. Supersymmetric particles and their SM counterparts differ by a half-integer in spin ( $s$ ). Bosons (fermions) in the SM have superpartners which are fermions (bosons).

Two complex Higgs doublets are required in the MSSM,  $\mathbf{H_d} = (H_1^0, H_1^-)$  and  $\mathbf{H_u} = (H_2^+, H_2^0)$  to give mass to the **down**-typed quarks (and leptons) and to the **up**-typed quarks, respectively. Particles interact with the Higgs bosons through a superpotential through dimensionless Yukawa couplings to acquire masses. Details of the nature of these interactions and spontaneous SUSY breaking can be found in [12, 13, 15].

The names of supersymmetric particles are derived from their SM counterparts by adding an “ $s$ ” in front of the SM particle name. For example, a *selectron* is the supersymmetric partner of the electron, *squarks* are the supersymmetric partners of SM quarks. The symbol of SUSY particles carry the “ $\sim$ ” sign above the symbol. For example if  $q$  is a SM particle then its supersymmetric partner is written as  $\tilde{q}$ . Superpartners of bosons are indicated with the suffix “-ino”, as in *wino* and *gluinos*.

The superpartners of SM fermions are scalars called *sfermions* ( $\tilde{l}$ ), sneutrinos ( $\tilde{\nu}$ ) and squarks ( $\tilde{q}$ ) while *gluinos* ( $\tilde{g}$ ) are the superpartners of the massless gauge bosons of strong interaction, gluons. The vector bosons ( $W^\pm, W^0, B$ ) have fermionic superpartners called *Winos* and *Binos*.

Standard Model			Supersymmetry		
Particle	Symbol	Spin	Particle	Symbol	Spin
quark	$q$	$\frac{1}{2}$	squark	$\tilde{q}$	0
lepton	$\ell$	$\frac{1}{2}$	slepton	$\tilde{\ell}$	0
W Bosons	$W^\pm, W^0$	1	Wino	$\tilde{W}^\pm, \tilde{W}^0$	$\frac{1}{2}$
B Boson	$B$	1	Bino	$\tilde{B}$	$\frac{1}{2}$
gluon	$g$	1	gluino	$\tilde{g}$	$\frac{1}{2}$
Higgs Bosons	$H \times 4$	0	higgsino	$\tilde{H} \times 4$	$\frac{1}{2}$
Graviton	$G$	2	gravitino	$\tilde{G}$	$\frac{3}{2}$

Table 2.3: Particles in the MSSM. SUSY particles (sparticles) have a “~” on the symbol

Particle Names	Gauge eigenstates	Mass eigenstates
squark	$\tilde{q}$	$\tilde{q}$
slepton	$\tilde{\ell}$	$\tilde{\ell}$
Neutralinos	$\tilde{W}^0, \tilde{B}^0, \tilde{H}_1^0, \tilde{H}_2^0$	$\tilde{\chi}_1^0, \tilde{\chi}_2^0, \tilde{\chi}_3^0, \tilde{\chi}_4^0$
Charginos	$\tilde{W}^+, \tilde{W}^-, \tilde{H}^+, \tilde{H}^-$	$\tilde{\chi}_1^\pm, \tilde{\chi}_2^\pm$
Higgs bosons	$H_1^0, H_2^0, H_1^-, H_2^+$	$h^0, H^0, A^0, H^\pm$
gluino	$\tilde{g}$	$\tilde{g}$
Gravitino	$\tilde{G}$	$\tilde{G}$

Table 2.4: Gauge and mass eigenstates of SUSY particles in the Minimal Supersymmetric SM (MSSM).

The superpartners of these Higgs bosons ( $H_1^0, H_2^0, H_1^-, H_2^+$ ) are fermions called *higgsinos* ( $\tilde{H}_1^0, \tilde{H}_1^-, \tilde{H}_2^0, \tilde{H}_2^+$ ) while the superpartners of the gauge bosons are called *gauginos* ( $\tilde{B}^0, \tilde{W}^0, \tilde{W}^-, \tilde{W}^+$ ). The neutral gauginos and higgsinos ( $\tilde{B}^0, \tilde{W}^0, \tilde{H}_1^0, \tilde{H}_2^0$ ) mix together to form four neutral fermions called *Neutralinos* ( $\tilde{\chi}_1^0, \tilde{\chi}_2^0, \tilde{\chi}_3^0, \tilde{\chi}_4^0$ ), and the charged gauginos and higgsinos ( $\tilde{W}^-, \tilde{W}^+, \tilde{H}_1^-, \tilde{H}_2^+$ ) mix together to form four charged fermions called *Charginos* ( $\tilde{\chi}_1^\pm, \tilde{\chi}_2^\pm$ ). The mass of the neutralinos and charginos depend on the mixing parameters of these gauginos and higgsinos and is model dependent.

We summarize in Tables 2.3 and 2.4 particles in the MSSM and how they relate to their SM partners. The gauge and mass eigen mass states of fermionic supersymmetric particles in the MSSM is also shown.

### R-Parity

In supersymmetry, it is, in principle, acceptable to include terms in the MSSM Lagrangian density which may not be conserved quantum numbers like the *baryon* ( $B$ ) and *lepton* ( $L$ ) numbers. For example, a consequence of adding such a term is that predictions of the proton's lifetime is much shorter than measured in experiments. Since no such phenomenon which violate these quantum numbers have been observed in experiments, SUSY models are constructed with the introduction of an additional matter symmetry called *R-Parity*, which relates the quarks to leptons through the baryon and lepton numbers. R-parity is defined as

$$R_P = (-1)^{3(B-L)+2S} \quad (2.9)$$

where,  $S$  is the particle's spin. SM particles like quarks have an *even* R-parity,  $R_P = 1$ , while supersymmetric particles like squarks have odd parity  $R_P = -1$ .

The phenomenological consequence of R-parity are the following: first, in the decay of supersymmetric particles, the lightest SUSY particle (LSP) have odd parity,  $R_P = -1$ , it is electrically neutral and considered to be absolutely stable. This makes the LSP a good dark matter candidate particle [2, 5], second, every supersymmetric particle produced will eventually decay into an odd number of LSPs, third, supersymmetric particles can only be produced in pairs. This phenomenological consequences make *R-parity Conserving* (RPC) SUSY models very attractive for experimental studies.

## Cross Sections, Decay Rate and Branching Ratio

### Cross Section

The cross section of producing a particle at a collider, like the LHC, is the probability that the proton beams will collide and interact in a certain way to produce the particle. The cross sections provides a way of counting the number of the particle produced when these proton beams collide. The cross section of producing a supersymmetric particle at the LHC depends on the following: the available energy of the proton beams compared to the mass of the particle, the type of interaction or size of the couplings during collision and the flux of the proton beams. Since the predicted mass of supersymmetric particles is higher than that of SM particles, we expect very few supersymmetric particles, if any, to be produced at the LHC, and even fewer supersymmetric particles for massive particles. The typical cross section of producing a supersymmetry particle at the LHC is of the order of  $1 \text{ pb} = 10^{-12} \times 10^{-24} \text{ cm}^2$  or at times  $1 \text{ fb} = 10^{-15} \times 10^{-24} \text{ cm}^2$  for extremely rare SUSY processes which can be compared to that for a standard model process, like, the production of the Z or  $W^\pm$  bosons which is of the order of a few  $nb = 10^{-9} \times 10^{-24} \text{ cm}^2$ .

Supersymmetric particles are most likely to be produced at the LHC, through the process of strong interactions ( $pp \rightarrow \tilde{g}\tilde{g}, \tilde{q}\tilde{q}$ ) than electro-weak interactions processes ( $pp \rightarrow \tilde{\chi}^\pm\tilde{\chi}^\mp, \tilde{\chi}^0\tilde{\chi}^\pm$ ), since the cross section for strong interaction processes is larger. Figure 2.4, shows the cross section, on the vertical y-axis, against the mass of the supersymmetric particle, on the horizontal x-axis. With  $20 \text{ fb}^{-1}$  of LHC integrated luminosity (relates the cross section and the rate of particle produced) of data from proton-proton ( $pp$ ) collisions at  $\sqrt{S} = 8 \text{ TeV}$ , we expect to see more events (vertical z-axis) with supersymmetric particles produced at the LHC through strong interactions than electro-weak interactions for a given SUSY sparticle mass.

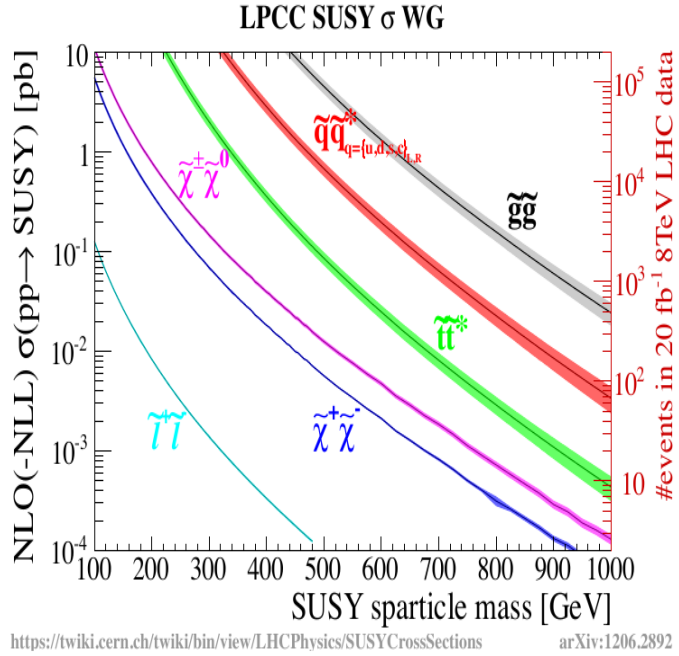


Figure 2.4: Cross section against SUSY sparticle mass for producing supersymmetric particles in different modes of interactions at the LHC. More supersymmetric particles are produced through strong interaction,  $pp \rightarrow \tilde{g}\tilde{g}$ , processes than the any other process.

### Decay Rate and Branching Ratio

After the production of a SUSY sparticle, the particle may decay either immediately after it was produced to live for a while before it decays. The rate at which the SUSY sparticle decays is called the *decay width* ( $\Gamma$ ) and it is related to the mean lifetime ( $\tau$ ) through the relation

$$\tau = \frac{\hbar}{\Gamma}. \quad (2.10)$$

Since the decay width depends on the coupling or the mass difference between the SUSY sparticle and its decay products, SUSY particles with small mass differences of large coupling to the daughter particles has smaller decay width and therefore have long lifetimes. The final products of the decay depends on the branching ratio for a given decay channel. In R-parity conserving models, SUSY sparticles are produced in pairs and each decay through a cascade decay process into the LSP and its SM partner.

A SUSY sparticle may decay through strong interactions in which case its mean lifetime

is about  $10^{-17}$  to  $10^{-25}$  seconds, through electromagnetic interactions in which case its mean lifetime maybe between  $10^{-20}$  seconds to about  $10^{-14}$  seconds and through weak interactions in which case its mean lifetime maybe vary from  $10^{-13}$  seconds to  $10^{-8}$  seconds.

By Long-lived particles, we are interested in particles decays through none of the SM interactions and has a typical mean lifetime ranging from a few nanoseconds to hundreds of a nanosecond. These are the kind of long-lived particles we study in this thesis.

### 2.2.2 Gauge Mediated Supersymmetry Breaking Models

A consequence of SUSY is that supersymmetric particles and their SM partners must have the same mass. However, because no supersymmetric particle have been observed with the same mass as SM particles, it means SUSY is not an exact symmetry of nature and must be broken. SUSY breaking should happen such that the mass of supersymmetric particles are higher than their standard model counterparts. The two ways of breaking SUSY are explicit and spontaneous breaking. Similar to the motivation of spontaneous symmetry breaking through the Higgs mechanism in the SM, spontaneous SUSY breaking is theoretically favored because it preserves renormalisability also in the MSSM. SUSY breaking is realized by introducing SUSY-breaking terms known as *soft breaking terms* to the Lagrangian density, which ensures that coupling constants which may lead to quadratic divergence are not introduced and the mass of the supersymmetric particles can be at about the TeV energy scale [13, 14, 15]. In theory SUSY breaking happens in the so-called *Hidden Sector* [14], and can be mediated to the MSSM sector through interactions which do not change the flavor of the particles called *flavor blind interactions* e.g. gauge interactions [16]. SUSY models based on gauge interactions mediating SUSY breaking from hidden sector to MSSM sector are called *Gauge Mediated Supersymmetry Breaking* (GMSB) models. GMSB models are interesting at an experimental level because they predict the existence of long-lived particles which can decay into light gravitino, a spin-3/2 superpartner of the graviton field, which is a good candidate dark matter particle since it is stable and neutral.

Gauge Mediated Supersymmetry Breaking (GMSB) models are based on the idea that *Messenger* particles through gauge interactions are responsible for mediating SUSY breaking from the *hidden sector* to the visible or MSSM sector. The energy scale

of the hidden sector, which is the Vacuum Expectation Value (VEV) of scalar fields responsible for SUSY breaking (some kind of *superHiggs mechanism*, [14]) is denoted by a fundamental parameter,  $\mathbf{F}$ , also known as the *Fundamental SUSY Breaking Parameter*. The mass of the messenger particle,  $\mathbf{M}_{\text{mess}}$ , is related to  $\mathbf{F}$  through an *effective SUSY* breaking energy scale parameter,  $\Lambda$ , at the MSSM level. This relationship can be written as  $\mathbf{F}/\Lambda = \mathbf{M}_{\text{mess}}$  and  $\Lambda$  can be interpreted as the energy scale at which SUSY breaking is felt by the MSSM particles.

For a given choice of the value of  $\mathbf{F}$ , the mass spectrum of all supersymmetric particles including the Lightest SUSY Particle (LSP) is well defined. Since the value of  $\mathbf{F}$  is not known and can vary, the mass of the LSP can also vary. This variation of the fundamental SUSY breaking scale or equivalently the mass of the LSP is parametrized by a scaling parameter,  $C_{\text{grav}}$ .

In GMSB models and in SUSY models in general, the value of the VEVs,  $v_u$  and  $v_d$ , of the two Higgs doublets in the MSSM is not known and is therefore an additional parameter,  $\tan(\beta)$ , in most models. This parameter relates the VEVs;  $\tan(\beta) = \frac{v_u}{v_d}$ . Another parameter,  $\text{sgn}(\mu)$ , defines the sign, which is arbitrary, of the parameter  $\mu$  in the Higgs Boson's potential.

Thus, in GMSB models there are only (compared to the SM which has at least 19) 5 input parameters given as

$$\{\Lambda, \mathbf{M}_{\text{mess}}, \mathbf{N}_5, \tan(\beta), \text{sgn}(\mu), C_{\text{grav}}\} \quad (2.11)$$

where,  $\mathbf{N}_5$  is the number of messenger particles mediating SUSY breaking. Different choices for the values of these parameters will represent different scenarios for GMSB models.

A unique feature in GMSB models is that the mass of the Lightest SUSY Particle (LSP) can be made (through  $C_{\text{grav}}$ ) to be as light as possible in order for a model prediction of the mass of the dark matter candidate particle to agree with bounds from cosmology. In GMSB models, the LSP is most certainly the gravitino ( $\tilde{G}$ ) as long as,  $\mathbf{M}_{\text{mess}}$  is very small compared to  $M_{Pl}$ , the energy scale where gravitational interactions become relevant. The gravitino's mass,  $m_{\tilde{G}}$ , can be expressed in terms of the parameter

$C_{grav}$  and  $M_{Pl}$  as

$$m_{\tilde{G}} = C_{grav} \cdot \frac{\Delta M_{mess}}{\sqrt{3} M_{pl}} \quad (2.12)$$

where,  $M_{Pl} = 1.3 \times 10^{19} \text{ GeV}/c^2$ . By varying the scaling parameter,  $C_{grav}$ , the mass of the gravitino will also vary and the decay rate of the Next-to-Lightest-Supersymmetric Particle (NLSP) to the gravitino will also vary. Varying the decay rate will vary the lifetime of the NLSP from decaying immediately or promptly to being long-lived. The decay rate of the NLSP to the gravitino depends on the mass difference between the NLSP and the gravitino and also on the coupling or strength of its interaction with the gravitino, [16, 17].

### 2.3 Long-Lived Neutral Particles in GMSB Models

In GMSB, *gravitino-scalar-chiral fermion* ( $(\psi, \tilde{G}, \phi)$ ) and *gravitino-gaugino-gauge boson* ( $(\lambda, \tilde{G}, A)$ ) interactions, between the gravitino and its partners in the same supermultiplet, shown in Figure 2.5, are present. These interactions allow for any supersymmetric particle,  $\tilde{P}$ , to decay to its SM partner,  $P$ , and the gravitino ( $\tilde{G}$ ), with its decay rate suppressed because of the nature of the interaction coupling strength contributing as  $\frac{1}{\sqrt{F}}$ .

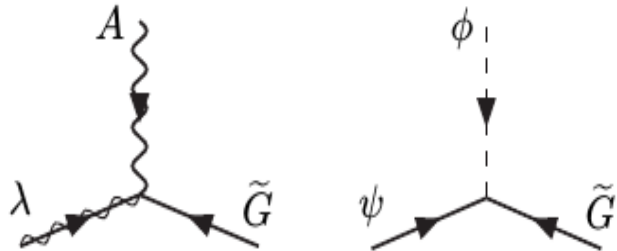


Figure 2.5: Feynman diagrams of Gravitino-Gaugino ( $(\lambda, A)$ ) (left) and Gravitino-Scalar ( $(\psi, \phi)$ ) (right) couplings. The coupling strength goes like  $\frac{1}{\sqrt{F}}$

The decay rate for  $\tilde{P} \rightarrow P + \tilde{G}$  can be computed as

$$\Gamma(\tilde{P} \rightarrow P + \tilde{G}) = \frac{m_{\tilde{P}}^5}{16\pi F^2} \left(1 - \frac{m_P^2}{m_{\tilde{P}}^2}\right)^2 \quad (2.13)$$

where, the terms in the the decay rate are due to the nature of the interaction and also from the kinematic phase space integral where the mass of the gravitino can be neglected in the computation.

The decay width is larger for smaller values of fundamental SUSY breaking parameter,  $F$  or equivalently for smaller gravitino masses,  $m_{\tilde{G}}$ . If we re-write the fundamental SUSY breaking scale as  $F = C_{grav} \cdot m_{\tilde{G}} \sqrt{3} M_{pl}$ , we see that for different values of  $C_{grav}$ , which signifies changing the mass of the gravitino or the fundamental SUSY breaking scale, the decay width can also be vary. Thus, by varying the decay width, we can vary the lifetime of the supersymmetric particle  $\tilde{P}$ , for fixed mass, from being prompt to being long-lived.

In a scenario where the, SUSY particle  $\tilde{P}$  is not the Next-To-Lightest Supersymmetric Particle (NLSP), the decay,  $\tilde{P} \rightarrow P + \tilde{G}$ , suffers from competition with other probably favorable decay channels and this process is not competitive enough to happen at a collider experiment. However, if  $\tilde{P}$  is the NLSP, then there is no competition and this decay is always sure to happen at a collider.

It is important to observe here that, because the decay rate is large for smaller values of the fundamental SUSY breaking scale or equivalently smaller gravitino mass for a fixed lightest neutralino mass, if  $m_{NLSP}$  is of the order of 100 GeV or more and  $\sqrt{F} \ll 1000$  TeV, meaning  $m_{\tilde{G}} \leq 1$  keV, then the above decay rate is of the order that can be observed at hadron collider detectors.

### 2.3.1 Benchmark Scenario

In this thesis, we focus on a benchmark working model of R-parity conserving GMSB models called the *Snowmass Point and Slopes* (SPS8),[18]. In the SPS8 model, the following choice of GMSB parameters are made:

$$M_{mess} = 2\Lambda \quad \tan(\beta) = 15 \quad N_5 = 1 \quad (2.14)$$

where  $\Lambda$  and  $C_{grav}$  are the free to vary.

The LSP is the gravitino ( $\tilde{G}$ ) and the lightest neutralino ( $\tilde{\chi}_1^0$ ) is the NLSP. Since the  $\tilde{\chi}_1^0$  is a mixture of the supersymmetric particles Bino ( $\tilde{B}^0$ ), Wino ( $\tilde{W}^0$ ), higgsino ( $\tilde{H}_u^0, \tilde{H}_d^0$ ), its decay to its SM partner and the gravitino will depend on the choice of parameters which affect the mixing. Since the parameters:  $\Lambda$ ,  $\tan \beta$ , and  $sgn(\mu)$  do affect the mixing, these parameters have been chosen in the SPS8 model to maximize the branching ratio involving the decay of the  $\tilde{\chi}_1^0$  to a photon ( $\gamma$ ) and a gravitino over the other possible SM partners: Z boson,  $Z'$  and a higgs boson ( $h$ ), [17].

Thus, this thesis duels on the search for decay of the lightest neutralino,  $\tilde{\chi}_1^0$ , as a LLNP, to a photon and the gravitino,  $\tilde{\chi}_1^0 \rightarrow \gamma + \tilde{G}$ . By varying  $\Lambda$  and  $C_{grav}$ , we study the production and decay of  $\tilde{\chi}_1^0$  for different masses and lifetimes.

### Supersymmetric Particle Mass Spectra

The masses of all supersymmetric particles (sparticles) is determined by the effective SUSY breaking energy scale parameter,  $\Lambda$  and increases with increasing values of  $\Lambda$ . Shown in Figure 2.6 , the sparticle mass spectra for  $\Lambda = 100$  TeV (left plot) and  $\Lambda = 180$  TeV (right plot) with the same values of  $C_{grav} = 93.5$  computed according to the SPS8 model. As observed in the Figure, the masses of the sparticles, including the mass of the lightest neutralino,  $\tilde{\chi}_1^0$ , is larger for  $\Lambda = 180$  TeV ( $m_{\tilde{\chi}_1^0} = 256$  GeV/ $c^2$ ) (right plot) than for  $\Lambda = 100$  TeV ( $m_{\tilde{\chi}_1^0} = 140$  GeV/ $c^2$ ) (left plot). This means that, in order to expand our search include heavier lightest neutralinos, we must scan large values of  $\Lambda$ .

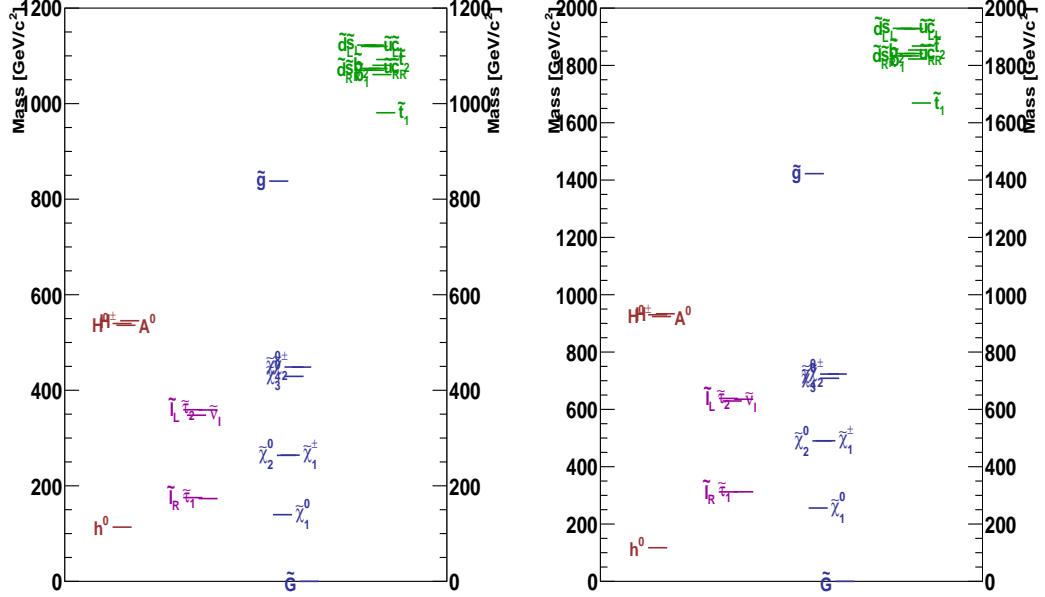


Figure 2.6: SUSY mass spectra for benchmark SPS8 model:  $\Lambda = 100 \text{ TeV}$  (left) and  $\Lambda = 180 \text{ TeV}$  (right) with  $C_{grav} = 93.5$ . SUSY particle mass increases with  $\Lambda$

### Lightest Neutralino as Long-Lived Neutral Particle

The lifetime of the lightest neutralino,  $\tilde{\chi}_1^0$ , in its decay;  $\tilde{\chi}_1^0 \rightarrow \gamma + \tilde{G}$ , expressed in terms of its mass,  $m_{\tilde{\chi}_1^0}$  and the supersymmetry breaking scale,  $\mathbf{F}$ , is given as

$$c\tau_{\tilde{\chi}_1^0} \approx \left( \frac{m_{\tilde{\chi}_1^0}}{\text{GeV}} \right)^{-5} \left( \frac{\sqrt{\mathbf{F}}}{\text{TeV}} \right)^4 \quad (2.15)$$

and in terms of the parameter changing the  $\tilde{\chi}_1^0$  lifetime,  $C_{grav}$ , Equation 2.15 becomes

$$c\tau_{\tilde{\chi}_1^0} \approx C_{grav}^2 \left( \frac{m_{\tilde{\chi}_1^0}}{\text{GeV}} \right)^{-5} \left( \frac{\sqrt{\Lambda \cdot M_{\text{mess}}}}{\text{TeV}} \right)^4. \quad (2.16)$$

Thus, by changing the value of  $C_{grav}$ , we change the lifetime of  $\tilde{\chi}_1^0$ , similar to changing the value of  $\Lambda$ , we get  $\tilde{\chi}_1^0$  with different masses.

The probability for a neutralino ( $\tilde{\chi}_1^0$ ), produced with energy  $E_{\tilde{\chi}_1^0}$  and mass  $m_{\tilde{\chi}_1^0}$  to travel a distance  $x$  before decaying to a photon and gravitino in the laboratory frame can be expressed as  $\mathcal{P}(x) = 1 - \exp\left(-\frac{x}{L}\right)$ , where the distance traveled in a particle

detector by the neutralino is given by Equation 2.17.

$$L = \left( c\tau_{\tilde{\chi}_1^0} \right) \cdot (\beta\gamma)_{\tilde{\chi}_1^0} \quad (2.17)$$

From Equation 2.17, it is clear that this distance depends on two main factors. The boost factor,  $(\beta\gamma)_{\tilde{\chi}_1^0} = \frac{|\vec{p}_{\tilde{\chi}_1^0}|}{m_{\tilde{\chi}_1^0}} = \sqrt{\left(\frac{E_{\tilde{\chi}_1^0}}{m_{\tilde{\chi}_1^0}}\right)^2 - 1}$ , which indicates how fast the neutralino is traveling before it decays. For slow moving neutralino,  $(\beta\gamma)_{\tilde{\chi}_1^0} \ll 1$ .

In this theses, we are interested in the production of the lightest neutralino from strong interaction processes like  $pp \rightarrow \tilde{g}\tilde{g}, \tilde{q}\tilde{q}$ , as these processes have a higher production cross section at the LHC. These are called direct production processes, where the  $\tilde{\chi}_1^0$  is a product of the *cascade decay* of squarks ( $\tilde{q}$ ), excited squarks ( $\tilde{q}^*$ ) and gluinos ( $\tilde{g}$ ). The Feynmann diagrams in Figure 2.7 represent the different  $\tilde{\chi}_1^0$  production processes at the LHC, through the cascade decay of gluinos and squarks. The final state may include two photons (left Feynmann diagrams) and two gravitinos if both  $\tilde{\chi}_1^0$  decay to a photon and a gravitino or just a single photon (right Feynmann diagrams) if only one  $\tilde{\chi}_1^0$  decay to a photon and gravitino.

Our signal, are events produced at the LHC with at least a single photon which is late, with respect to LHC  $pp$  collision times and large Missing Transverse Energy or MET. The MET is due to the presence of at least a single gravitino which escapes undetected. The Squarks and gluinos could directly decay into gravitinos and their SM partners, however, as explained previously, the direct decay to gravitino channel is in a competition with other channels which are most favorable and eventually lead to the gravitino decay through the  $\tilde{\chi}_1^0$ .

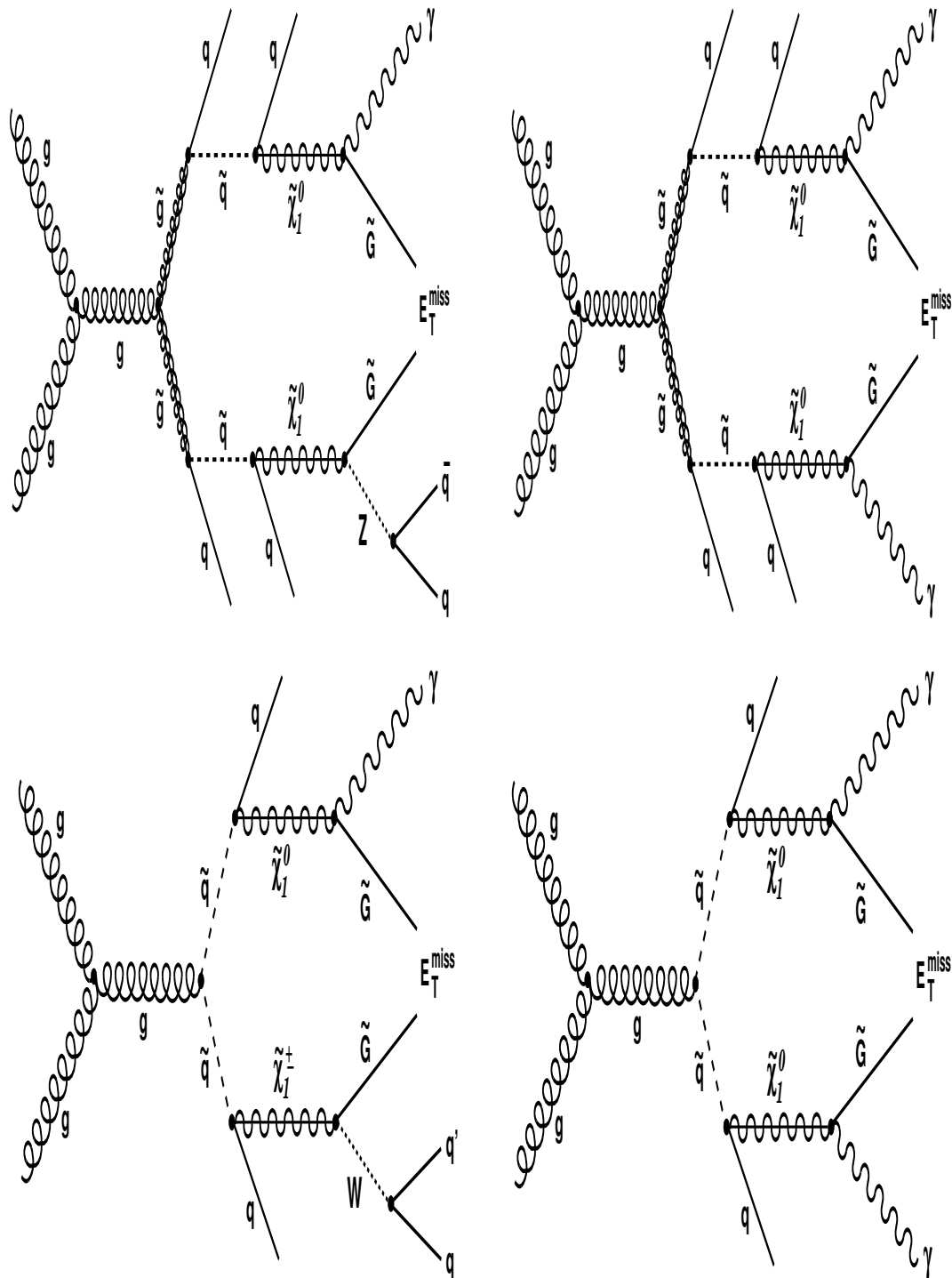


Figure 2.7: Feynmann diagrams for neutralino production from the cascade decay of a produced gluino (top) and squark (bottom). The final event has a single (left diagrams) or double photons (right diagrams) neutralino decay at LHC.

The photon arrival time at the detector from the  $\tilde{\chi}_1^0$  decay depends on the  $\tilde{\chi}_1^0$  lifetime  $c\tau$ , and the whether the  $\tilde{\chi}_1^0$  is produced with a high (moving fast) boost or low boost (moving slow). This means that the momentum ( $p_{\tilde{\chi}_1^0}$ ) of the  $\tilde{\chi}_1^0$  during production from gluino or squarks decays must be much smaller than its mass,  $m_{\tilde{\chi}_1^0}$ . Lightest neutralinos ( $\tilde{\chi}_1^0$ s) produced such that the  $\tilde{\chi}_1^0$  is moving slow,  $p_{\tilde{\chi}_1^0}/m_{\tilde{\chi}_1^0} \ll 1$ , are definitely good candidates for producing photons which arrive the detector late. Since  $\mathbf{A}$ , determines the mass of gluino ( $\tilde{g}$ ), squarks ( $\tilde{q}$ ) which decay to the  $\tilde{\chi}_1^0$ . Therefore the momentum of  $\tilde{\chi}_1^0$  ( $p_{\tilde{\chi}_1^0}$ ) is determined by the masses of gluino and squarks. If the gluino or squark decays to the neutralino in association with a many gluons and quarks seen in the detector as *jets*, then the neutralino momentum is small with the ratio  $p_{\tilde{\chi}_1^0}/m_{\tilde{\chi}_1^0} \ll 1$ . This means the  $\tilde{\chi}_1^0$  produced with low boost or moving slow and therefore the photon from its decay arrives late at the detector compared to proton-proton collision times. However, if the gluino or squark is decays with less number of jets, then the  $\tilde{\chi}_1^0$  momentum is not small and is produced with significant boost that it leaves the detector without decay.

The other factor is the inherent long lifetime,  $c\tau_{\tilde{\chi}_1^0}$ , of the  $\tilde{\chi}_1^0$ .  $\tilde{\chi}_1^0$ s with significant  $c\tau_{\tilde{\chi}_1^0}$ , would travel some distance in the detector before they decay, and therefore the resulting photon has a chance of arriving late at the detector. If  $c\tau_{\tilde{\chi}_1^0}$  is very short, which is similar to cases where the parameter,  $C_{grav} \approx 1$ , and the  $\tilde{\chi}_1^0$  decay is prompt, the photon cannot be easily described as “late” using only its arrival time at the detector, as its lifetime is very short.

### 2.3.2 Signal Modeling

We produced simulated high-energy-physics signal events according to the SPS8 benchmark model using general-purpose event generators based on Monte Carlo (MC) methods of numerical computations. The process of event generation starts with the production of *SUSY Les Houches Accord* (SLHA) files using a SUSY software package called **ISASUSY**[20]. These SLHA files contain the masses, interaction couplings, decay widths and all possible decay channels and their Branching Ratio (*BR*) of every supersymmetric particles. Each file also contain the value of the fundamental GMSB model parameters;

$$\left\{ \mathbf{A}, \mathbf{M}_{mess}, \mathbf{N}_5, \tan(\beta), sgn(\mu), C_{grav} \right\} \quad (2.18)$$

spanning all the possible, in terms of particle kinematics, supersymmetric particle production and decay configurations or phase space, as defined by the model, in the production of events. In the SPS8 model, the choice of parameters is such that

$$\text{sgn}(\mu) = 1, \tan(\beta) = 15, \mathbf{N}_5 = 1, \mathbf{M}_{\text{mess}} = 2\Lambda, \quad (2.19)$$

where  $C_{grav}$  and  $\Lambda$  are not fixed . By varying, respectively,  $C_{grav}$  and  $\Lambda$ , we can exploit different decay scenarios where the  $\tilde{\chi}_1^0$  has a different lifetime and mass. For a specific choice of  $C_{grav}$  and  $\Lambda$ , we produce a signal sample where the events have a mean lifetime ( $c\tau$ ) and mass of the  $\tilde{\chi}_1^0$ . A special software package called **HDECAY**, is used to handle the decay of all supersymmetric particles including the  $\tilde{\chi}_1^0$ .

The signal events are generated according to the processes described by the Feynmann diagrams in Figure 2.7 using particle generators based on Monte Carlo simulations. The produced  $\tilde{\chi}_1^0$  cascade decay of the gluino/squarks;

$$p + p \rightarrow \tilde{g}\tilde{g}, \tilde{q}\tilde{q} \rightarrow [\text{1 or 2 cascade decays}] \rightarrow 2\tilde{\chi}_1^0 + \text{jets} \rightarrow 2\gamma + 2\tilde{G} + \text{jets}, \quad (2.20)$$

is allowed to decay to either  $\gamma$ ,  $Z$  bosons,  $H$ ,  $e^+e^-$ , and the  $\tilde{G}$ . However, its decay to a  $\gamma$  and  $\tilde{G}$  is the dominant mode of decay with a branching fraction for single photon decay channel,  $\tilde{\chi}_1^0 \rightarrow \gamma + \tilde{G}$ , about 83 to 94%. We observed that 97 to 99% of all our simulated signal events contain at least a single photon. We use **PYTHIA-6** [21] as the MC event generator. It takes as input an SLHA file and generates events of supersymetric particles, produced at the LHC  $pp$  collider with center of mass energy,  $\sqrt{S} = 8$  TeV. The interaction of these supersymmetric particles with the CMS detector is simulated using the **GEANT4** [22], particle detector simulation software. A full physics event is reconstructed from energy deposits (hits) in the CMS detector using the CMS event reconstruction Software (CMSSW). To minimize any disagreement between MC and data, we use the same CMSSW release version (**CMSSW\_5\_3\_29**) in the MC event reconstruction with the same detector conditions as the recorded data.

We perform some sanity checks that the signal samples have been correctly generated by **PYTHIA-6**, by looking at the number of photons,  $E_T^{\text{miss}}$  and number of jets in each signal event. We also measured the mean lifetime of the  $\tilde{\chi}_1^0$  by fitting the distribution

of the  $\tilde{\chi}_1^0$  lifetime computed from its transverse distance traveled before decay. This distance is computed using its production and decay vertices. Comparing the mean lifetime,  $c\tau$ , obtained from the fit, to its theory value supposedly used in the event generation, we are able to check that each signal sample has been properly generated. We also observed that most of the events had at least a single photon (left plot) and at least 2 jets (right plot) shown in the top plots of Figure 2.9. Comparing different signal samples with  $c\tau = 2000 \text{ mm}, 4000 \text{ mm}, 6000 \text{ mm}$  of  $\Lambda = 180 \text{ TeV}$  and a  $\gamma +$  jet with  $120 < \hat{p}_T < 170 \text{ GeV}/c$  sample, we observed that the  $E_T^{\text{miss}}$  (shown in the bottom plot of the same figure) from signal events was larger than the  $E_T^{\text{miss}}$  of events from the  $\gamma +$  jet sample agreeing with our expectation that the  $\gamma +$  jet sample has mostly fake  $E_T^{\text{miss}}$  while signal samples have large  $E_T^{\text{miss}}$  due to the  $\tilde{\chi}_1^0$  decay to gravitino.

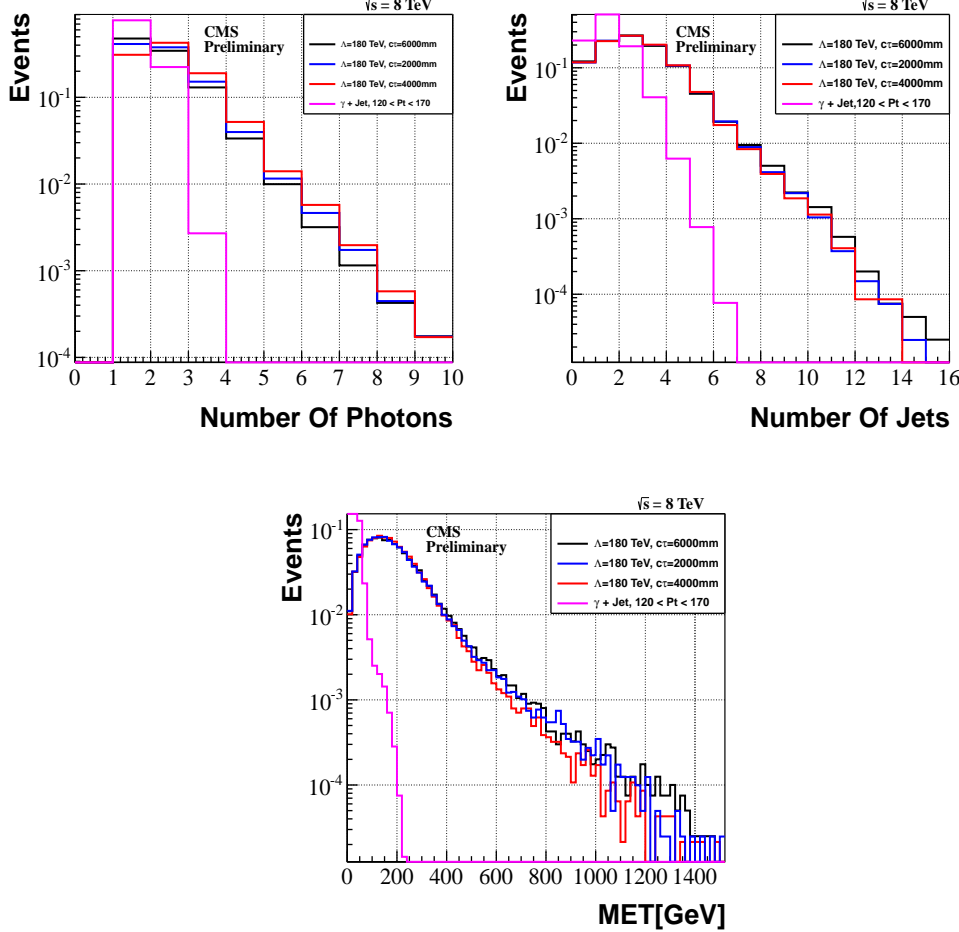


Figure 2.8: Number of photons (top left), Number of jets (top right) and  $E_T^{\text{miss}}$  (bottom) for events with  $\tilde{\chi}_1^0$  decay to  $\gamma$  and  $\tilde{G}$  for different  $c\tau = 2000 \text{ mm}, 4000 \text{ mm}, 6000 \text{ mm}$  points of  $\Lambda = 180 \text{ TeV}$  of the SPS8 model. A  $\gamma+\text{jet}$  with  $120 < p_T < 170 \text{ GeV}/c$  sample shown for comparison with the signal samples.

### 2.3.3 Lightest Neutralino's Lifetime

The distance traveled, in the CMS detector, by the  $\tilde{\chi}_1^0$  before it decays, mentioned previously section 2.3.1, is given as

$$L = (c\tau_{\tilde{\chi}_1^0}) \cdot (\gamma\beta) = (c\tau_{\tilde{\chi}_1^0}) \cdot \left( \frac{p}{m_{\tilde{\chi}_1^0}} \right). \quad (2.21)$$

This distance depends on the momentum ( $p$ ) and mean lifetime ( $c\tau_{\tilde{\chi}_1^0}$ ) of the  $\tilde{\chi}_1^0$ . Large values of  $c\tau_{\tilde{\chi}_1^0}$  means, this distance is large and if larger than the ECAL radius, can be interpreted as the  $\tilde{\chi}_1^0$  traveled outside the ECAL volume before it decayed, making detecting the delayed photon no longer possible. On the other hand, small values of  $c\tau_{\tilde{\chi}_1^0} < 10$  cm means the  $\tilde{\chi}_1^0$  decayed early and the photon is not late enough such that its detection using ECAL time measurements alone is not reliable. High- $p$  values means the  $\tilde{\chi}_1^0$  is boosted and could travel out of the ECAL before it decay, making the photon again undetectable. On the other hand, low- $p$  values means the  $\tilde{\chi}_1^0$  is less boosted and traveling slow enough for its decay to happen inside the ECAL volume and the photon delayed arriving at ECAL. In Figure 2.9, we show a distribution of the momentum of the  $\tilde{\chi}_1^0$  in the transverse ( $x - y$ ) plane (transverse momentum ( $p_T^{\tilde{\chi}_1^0}$ )), the  $\tilde{\chi}_1^0$  transverse distance traveled before it decay, the transverse momentum of the photon ( $p_T^\gamma$ ) and photon's estimated time ( $T_\gamma$ ) using only generator level information. These distributions are for different  $\Lambda$  and  $c\tau_{\tilde{\chi}_1^0}$  points of the SPS8 model. We observed that, the  $p_T^{\tilde{\chi}_1^0}$  increases with increase values of  $\Lambda$ , from  $\Lambda = 100$  TeV to 220 TeV, which agrees with our expectation. As  $\Lambda$  increases along with the masses of the gluino/squark and  $\tilde{\chi}_1^0$ , the  $p_T^{\tilde{\chi}_1^0}$  also increases since a massive gluino/squark decay into the  $\tilde{\chi}_1^0$ . In the same way, increasing the mass of  $\tilde{\chi}_1^0$  ( $m_{\tilde{\chi}_1^0}$ ) through increasing  $\Lambda$ , leads to increase in the photon  $p_T$ . For a given value of  $\Lambda = 180$  TeV, which means  $p_T^{\tilde{\chi}_1^0}$  is fixed, the transverse distance traveled by the  $\tilde{\chi}_1^0$  before decay (shown in the top right plot of Figure 2.9) and photon time (shown in the bottom right plot of the same figure) increased with increasing value of  $\tilde{\chi}_1^0$  mean lifetime,  $c\tau = 50$  cm to 600 cm in the same way, qualitatively. These observations support our expectation that the photon is delayed primarily because of the long lifetime of the  $\tilde{\chi}_1^0$ . However, one can argue that this is not entirely true and we will exploit this further in a detailed study of the source of delayed photons in the next section.

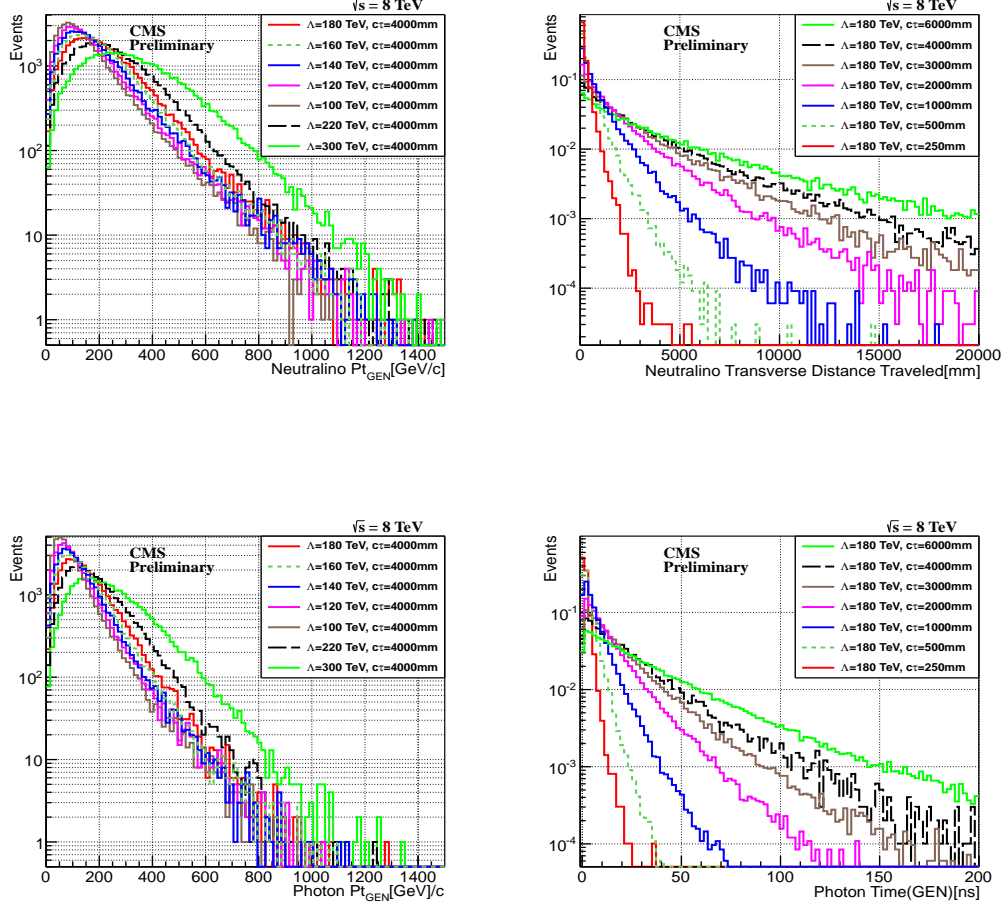


Figure 2.9: Neutralino transverse momentum ( $p_T^{\tilde{\chi}_1^0}$ ) distribution (top left) and transverse distance traveled (top right). Transverse momentum (bottom left) and time (bottom right) of photon from neutralino decay for different  $\Lambda$  and  $c\tau$  points in GMSB SPS8 model.

The photon from the decay of  $\tilde{\chi}_1^0$  can arrive late at ECAL for either one of the following reasons: first, because the  $\tilde{\chi}_1^0$  is traveling slow i.e. with boost,  $\beta = \frac{p_{\tilde{\chi}_1^0}}{m_{\tilde{\chi}_1^0}} << 1$ , and second, because the  $\tilde{\chi}_1^0$  was produced with significant boost such that the photon traveled to ECAL through a non-direct flight path from the nominal  $pp$  interaction point. We distinguish between these two sources of delayed photons by estimating the photon arrival time at ECAL in each scenario using the distance traveled by  $\tilde{\chi}_1^0$  before decay

and the distance traveled by the photon from the decay point to the point of detection at ECAL. Figure 2.10 (left) is a schematic representation showing how we estimate the photon arrival time at ECAL in each of the possible travel flight path representing the different source of delayed photons. The estimated photon arrival ECAL time in each scenario is given as follows:

- For slow moving neutralinos:  $\Delta t_1 = (L1/c\beta) - (L1/c)$
- For non-direct traveled flight path:  $\Delta t_2 = (L1 + L2 - L3)/c$
- ECAL measured time =  $\Delta t_1 + \Delta t_2$

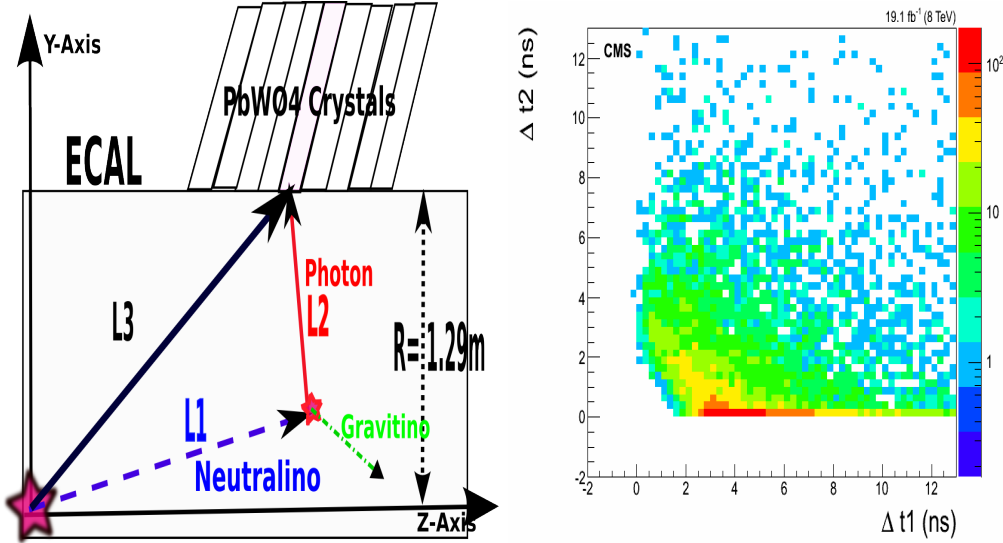


Figure 2.10: Schematic diagram showing  $\tilde{\chi}_1^0 \rightarrow \gamma + \tilde{G}$  decay topology within the ECAL volume of the CMS detector (Left). The estimated photon arrival time at ECAL from the decay of  $\tilde{\chi}_1^0$  in the SPS8 model with  $m_{\tilde{\chi}_1^0} = 256 \text{ GeV}/c^2$  and  $c\tau = 600 \text{ cm}$  (Right).

The  $\tilde{\chi}_1^0$  is traveling with velocity,  $v = c\beta$ , where  $c$  is the speed of light in vacuum. The distribution of the estimated photon ECAL arrival times  $\Delta t_1$  and  $\Delta t_2$ , is plotted shown in Figure 2.10(right), where the color intensity represents the photon population. We observed that most of the late arrival time photons are from the decay of slow moving  $\tilde{\chi}_1^0$  compared to those from non-direct flight path to ECAL. This proves that a good number of  $\tilde{\chi}_1^0$  produced with low momentum such that the ratio  $\frac{p_{\tilde{\chi}_1^0}}{m_{\tilde{\chi}_1^0}} \ll 1$  produced

most of our detectable delayed photons, using ECAL time measurements. While  $\tilde{\chi}_1^0$  with very long lifetimes ( $c\tau$ ) produced with high momentum will very likely escape the ECAL without detection unless their decay happens within the ECAL volume such that the delayed photon arrives at the ECAL in a non-direct flight path.

## 2.4 Previous Search Experiments

The have been other search experiments for LLNPs decaying to photons and missing transverse energy. The results have been interpreted int the context of the SPS8 benchmark models and other GMSB models. The results from DO, CDF, CMS and ATLAS,[23, 24, 25, 26, 27] experiments on the search for  $\tilde{\chi}_1^0$  as the NLSP decaying to photon and gravitino are shown in Figure 2.11. These results show that within the SPS8 model,  $\tilde{\chi}_1^0$  s with mass  $m_{\tilde{\chi}_1^0} \leq 245$  GeV and mean lifetime,  $c\tau_{\tilde{\chi}_1^0} \leq 6000$  mm are excluded at hadron colliders, based on the particle signal and background definitions used in these experiments. The plot on the left of Figure 2.11 are exclusion results with the mass of  $\tilde{\chi}_1^0$  or effective SUSY breaking scale  $\Lambda$  on the horizontal x-axis and the  $\tilde{\chi}_1^0$  lifetime,  $c\tau_{\tilde{\chi}_1^0}$  on the vertical y-axis from data recorded by the ATLAS experiment at  $pp$  with center of mass,  $\sqrt{S} = 7$  TeV. The plot on the left is for CMS experiment, with the same  $pp$  collision energy. The shaded regions are the excluded regions where the search results came out negative. We will discuss in detail these results in Chapter 8 when we compare our results to these results.

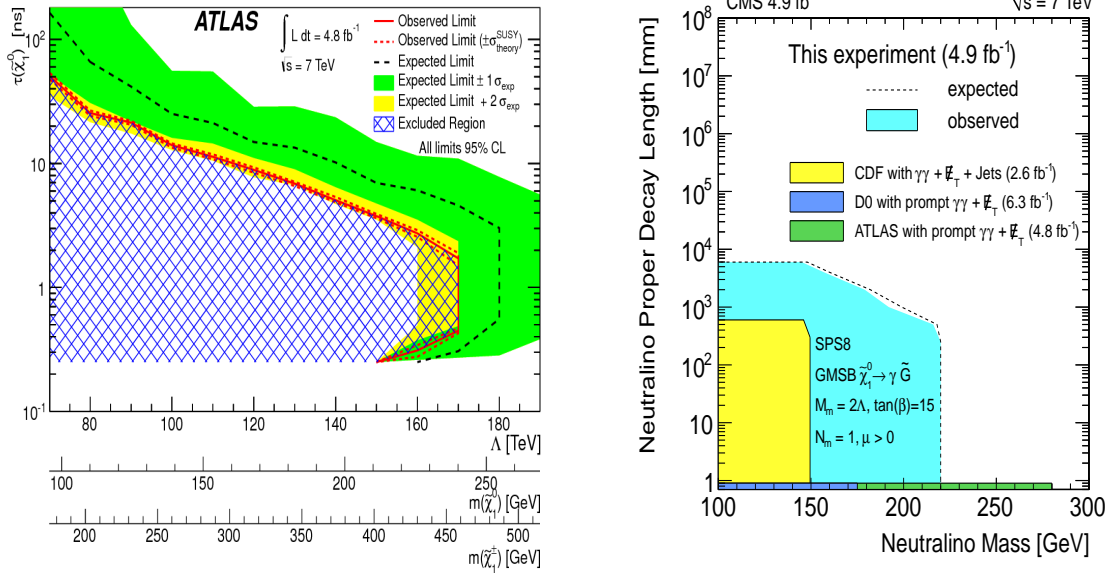


Figure 2.11: Neutralino lifetime and mass upper limit from ATLAS(left) and CMS(right) 7 TeV analysis with non-pointing photons and MET.

## Chapter 3

# Hadron Collider and Detector

The Large Hadron Collider (LHC) is a circular particle accelerator at CERN, accelerating two beams of either protons or ions through a circular ring in opposite directions and eventually colliding them at a collision point. Located at one of these collision points, is a general purpose multi-particle detector called the Compact Muon Solenoid (CMS). A detailed description of the LHC and CMS detector can be found in [28] and [29], respectively.

### 3.1 Large Hadron Collider

#### 3.1.1 Overview

The LHC accelerates and collides proton and heavy ion beams with a center of mass energy,  $\sqrt{S}$ , of 14 TeV. It is located across the border between France and Switzerland and hosted by the European Organization for Nuclear Research (CERN). The LHC uses powerful superconducting magnets to control and maintain the circulation of the beams in its circular ring of nearly 27 km in circumference. The circulating beams gain energy as they are transferred from the Booster and eventually into the LHC synchrotron where at 7 TeV they are steered by focusing magnets to a head-on collision against each other at a collision point. Figure 3.1 shows the LHC and the different stages of proton beam acceleration prior to collision.

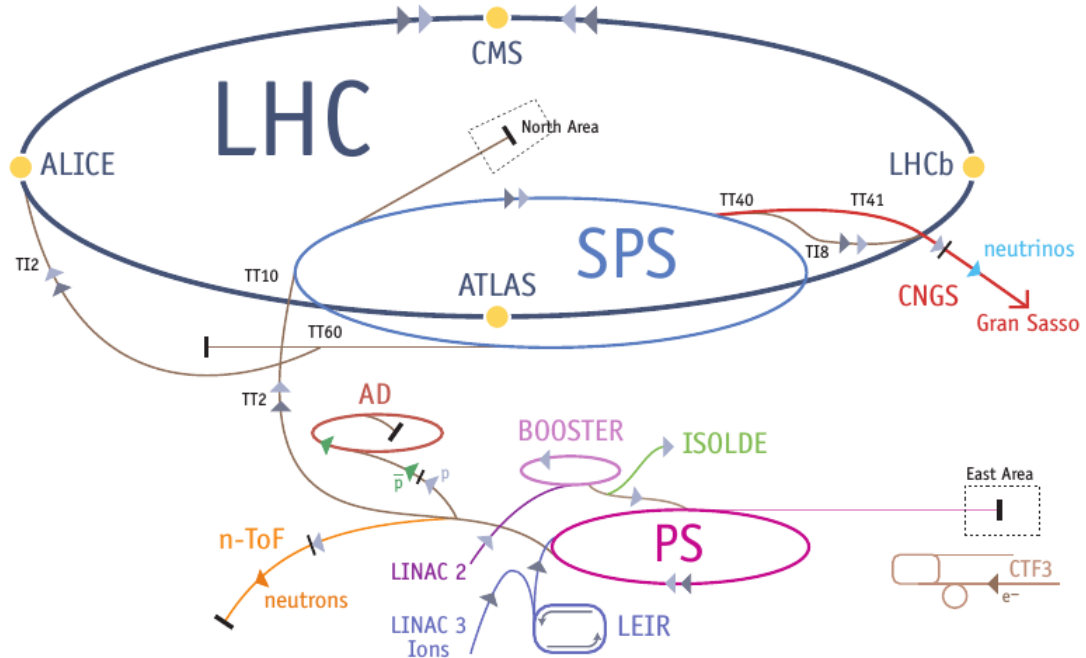


Figure 3.1: Schematic diagram showing the full Large hadron Collider.

### 3.1.2 Colliding Energy

Protons which are hydrogen ions from hydrogen gas where the orbiting electron has been stripped away are inserted into a linear accelerator called *LINAC 2*. Using the electromagnetic fields in Radio Frequency (RF) cavities, these protons are accelerated to an energy of 50 MeV creating a stream of particles called *proton beams* which are arranged in packets known as *bunches*. The proton beams from the LINAC 2 are injected into the circular *Proton Synchrotron Booster* (PSB) where they gain acceleration by passing many times through a cavity with their energy slowly increasing after each pass. The PSB accelerates the protons up to 1.4 GeV and injects them into the *Proton Synchrotron* (PS) which increases their energy to 25 GeV. These protons, traveling at 99.93% the speed of light at this stage, are sent to the *Super Proton Synchrotron* (SPS) and further accelerated to an energy of 450 GeV. The 450 GeV proton beams are finally transferred into the LHC ring (split into two beams accelerating in a clockwise and anti-clockwise direction) where they are accelerated for about 20 minutes to their nominal

energy of 7 TeV. By now the protons are traveling with the speed of 99.9999% the speed of light and powerful bending magnets are used to keep the beams traveling in the circular LHC ring.

In a circular particle collider like the LHC, the energy available to make new particles, known as the *center of mass* (COM) energy, denoted by  $\sqrt{S}$ , is simply the sum of the energy of the two beams i.e.  $\sqrt{S} = E_{\text{beam1}} + E_{\text{beam2}}$ . This is larger than that for fixed target colliders which is  $\sqrt{E_{\text{beam}}}$ . For example, in the LHC, each beam is designed to have an energy of 7 TeV making  $\sqrt{S} = 14 \text{ TeV}$ .

### 3.1.3 Luminosity

In colliding beams experiments, the center of mass energy available for the production of new effects is very important. However, the number of useful interactions producing effects (events) is equally important, especially in cases where the probability (also known as cross section,  $\sigma$ ) of producing rare events is very small. The quantity which measures the ability of a particle accelerator to produce the events from the required number of interactions is called *luminosity*. The luminosity is also the proportionality factor between the number of events per second and the cross section. Luminosity ( $\mathcal{L}$ ) is therefore a measure of the number of collisions that can be produced in a collider per squared area per second. The cross section is calculated from theory while the luminosity depends on factors ranging from the flux i.e. number of particles per second of the beams, the beam sizes at collision, and the frequency of collision. For physics experiments, the integrated luminosity which is total luminosity over a given period of time usually a year gives the amount of data that has been recorded by a given detector.

Using the luminosity ( $\mathcal{L}$ ) and the cross section ( $\sigma_p$ ) of a given process, we can calculate event rate ( $\mathcal{R}$ ) or the number of events per second produced in proton collisions by the given interaction process. By calculating the event rate, we are measuring a given cross section ( $\sigma_p$ ) through  $(\sigma_p = \frac{\mathcal{R}}{\mathcal{L}})$  in order to prove or disprove theories which make prediction on  $\sigma_p$ .

$$\mathcal{R} = \mathcal{L} \cdot \sigma_p \quad (3.1)$$

In CMS we have a “recorded” and “delivered” luminosity. Delivered luminosity refers to the luminosity delivered by LHC to CMS and one would expect this to be equal to

the amount recorded. However, there are instances where the CMS detector is unable to take data either because the data acquisition chain (DAC) or one of the CMS sub-detectors is temporarily down and also trigger dead time. Figure 3.2 shows the total integrated luminosity delivered by LHC and recorded using the CMS detector during the 8 TeV proton-proton collision by the LHC.

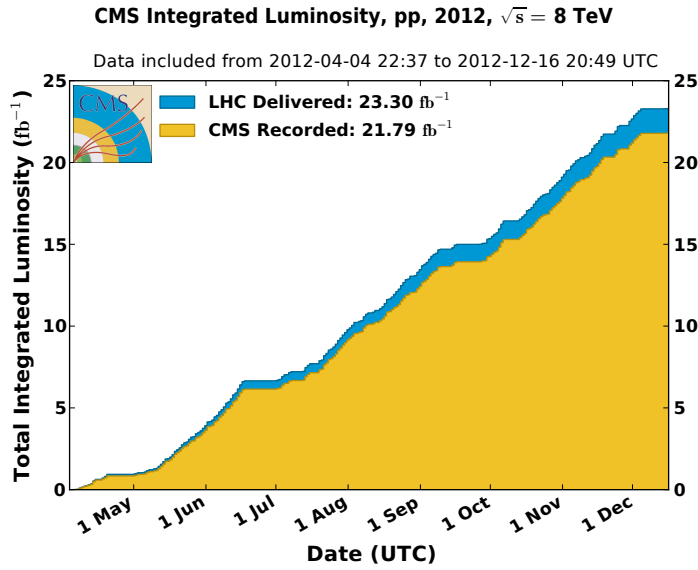


Figure 3.2: Cumulative luminosity versus day delivered to (blue), and recorded by CMS (orange) during stable beams and for p-p collisions at 8 TeV center-of-mass energy in 2012.

### 3.1.4 LHC Bunch Structure

Each LHC proton bunch is placed inside an RF buckets during beam filling. The filling scheme is such that not all RF buckets have proton bunches. Those empty buckets or beam gaps are necessary to avoid parasitic collision near IP and to make room for beam dump and beam halos known as beam cleaning. The separation in time between two buckets/bunches filled or unfilled is approximately 2.5 ns. There are about  $10^{11}$  protons per bunch during filling and acceleration. However, during filling and eventual bunch splitting at PS, it is possible that some empty buckets are filled with a much smaller proton population compared to the main bunch. These buckets with few protons can be either trailing the main bunch by  $\Delta t = 2.5, 5.0, 7.5, \dots$  ns, or leading the main bunch by  $\Delta t = -2.5, -5.0, -7.5, \dots$  ns. If these less populated bunches are 2.5 to 3.0 ns spaced

in time from each other, they are referred to as *satellite* bunches and if 5.0 ns, they are referred to as *ghost* bunches. Figure 3.3 shows ghost and satellite bunches and a main proton bunch.

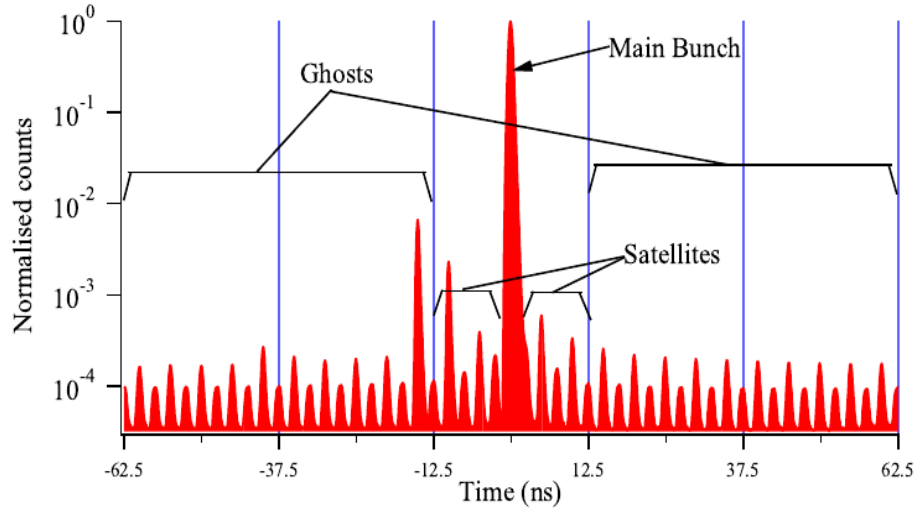


Figure 3.3: Longitudinal Profile taken with Longitudinal Density Monitor (LDM) detector showing definition of Ghost/Satellite bunches with respect to main bunches.

The presence of ghost/satellite bunches increases the uncertainty in LHC luminosity measurements and can also generate proton-proton interactions near but not at the collision region. Effects on ghost/satellite bunches on instantaneous luminosity measurements have been studied using CMS, ATLAS and ALICE detectors. Their results showing clear observation of physics events produced from ghost and satellite bunch collisions is shown in figure 3.4. CMS uses energy deposits in the endcap calorimeters to observe time space which is consistent with the expectation from ghost/satellite bunches while in ATLAS uses the Longitudinal Density Monitor (LDM) detector to study ghost/satellite bunches.

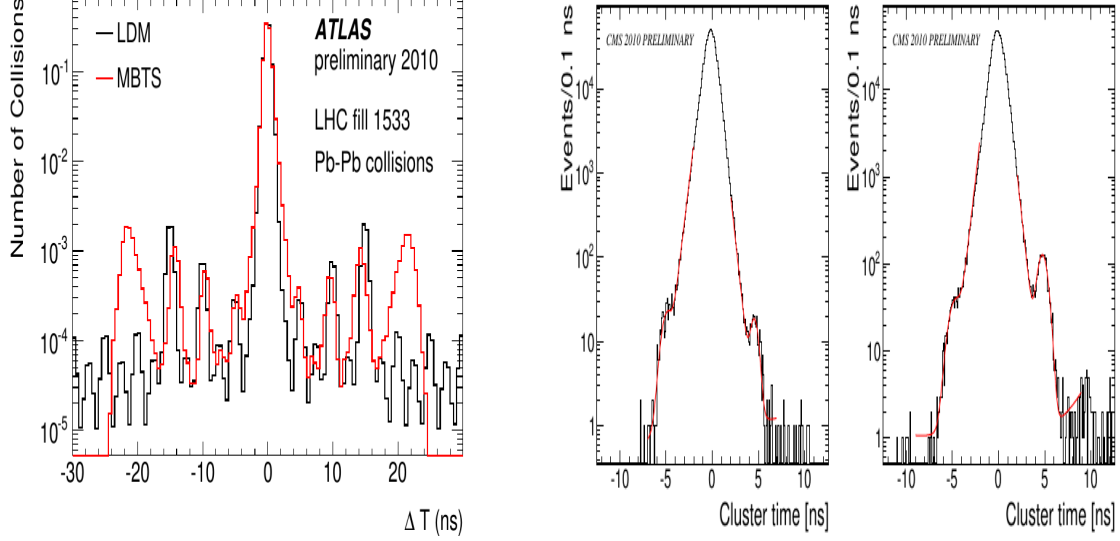


Figure 3.4: (left) Arrival time distribution(red) of ATLAS MBTS for LHC fill 1533 during 2010 Pb-Pb run and LDM profile(black) for Beam2(same for Beam1).  
 (Right) Timing of Clusters in the CMS endcap calorimeters for fill 1089:Left: EEP detector(left side of IP  $z > 0$ ) Right: EEM detector( right side of IP,  $z < 0$ ). Plots from ATLAS [38] and CMS, [39]

Table 3.1 gives a summary of the LHC design conditions compared to the conditions used during the LHC RUN 1 operation.

LHC Operation Parameters 2010-2013

Parameter	2010 value	2011 Value	2012/13 Value	Design Value
Beam energy[TeV]	3.5	3.5	4.0	7
$\beta^*$ in IP 5[m]	3.5	1.0	0.6	0.55
Bunch spacing [ns]	150	75/50	50	25
Number of bunches	368	1380	1380	2808
Protons/bunch	$1.2 \times 10^{11}$	$1.45 \times 10^{11}$	$1.7 \times 10^{11}$	$1.15 \times 10^{11}$
Normalised emittance[mm.rad]	$\approx 2.0$	$\approx 2.4$	$\approx 2.5$	3.75
Peak luminosity[ $cm^{-2}s^{-1}$ ]	$2.1 \times 10^{32}$	$3.7 \times 10^{33}$	$3.7 \times 10^{33}$	$1 \times 10^{34}$
Evts/bunch crossing	4	17	37	19
Stored Beam energy(MJ)	$\approx 28$	$\approx 110$	$\approx 140$	$\approx 362$
Int. Luminosity by CMS[ $pb^{-1}$ ]				-
Circumference[km]	26.659	26.659	26.659	26.659
Dipole Magnet B[T]	8.33	8.33	8.33	8.33

Table 3.1: LHC operation parameter conditions during RUN 1, 2010-2013

## 3.2 Compact Muon Solenoid

### 3.2.1 Overview

The Compact Muon Solenoid (CMS) is one of the multi-purpose particle detectors at the LHC proton collision point. It is a modern particle detector design for many different particle detection capability. The main feature of the CMS is the presence of a superconducting solenoid of 6 m internal diameter providing a field of 3.8 T for measuring a charge particle's momentum as the particle bends under the influence of this field traveling in the detector. This magnetic field encloses an entirely silicon pixel and strip tracker detector use for vertex finding and for detecting and reconstructing the tracks of charged particles, a lead-tungstate scintillating-crystals electromagnetic calorimeter (ECAL) and a brass-scintillating sampling hadron calorimeter (HCAL). Very long lived particles like muons are measured in gas-ionization detectors embedded in the flux-return iron-yoke located at the outermost section of the detector. It has a simple cylindrical structure consisting of barrel and endcap detectors and an extensive forward calorimetry and detectors to provide a near  $4\pi$  solid angle coverage assuring good hermetic particle detection. The CMS apparatus has an overall length of 21.6 m, a diameter of 14.6 m, and weighs 12,500 tons. Figure 3.5 shows the CMS detector indicating the different sub-detectors and their material design type. We provide a performance summary and material type of each sub-detector in Table 3.2 of the CMS detector. The CMS uses a coordinate system with the origin coinciding with the center of the detector where proton-proton or nominal collision occurs. This point is commonly referred to as the *interaction point* (IP). The direction of  $x$ ,  $y$ , and  $z$ -axes are as shown in figure 3.6. However, for particle identification, CMS uses a more convenient coordinate system based on the polar coordinates. In this polar coordinate system, the azimuthal angle,  $\phi$ , is measured in the  $x - y$  plane, where  $\phi = 0$ , is the  $x$ -axis and  $\phi = \pi/2$ , the  $y$ -axis. The radial distance in this plane is denoted  $R$  and the polar angle  $\theta$  measured from the  $z$ -axis is related to *pseudo-rapidity*,  $\eta$ , through the relation;  $\eta = -\ln \tan(\frac{\theta}{2})$ . The coordinate system  $(\eta, \phi)$  and its radial distance  $R$  identifies a point in the cylindrical volume of the CMS detector. In the coming sections, we describe the geometry, material characteristics and functionality of the CMS subdetectors used in our analysis.

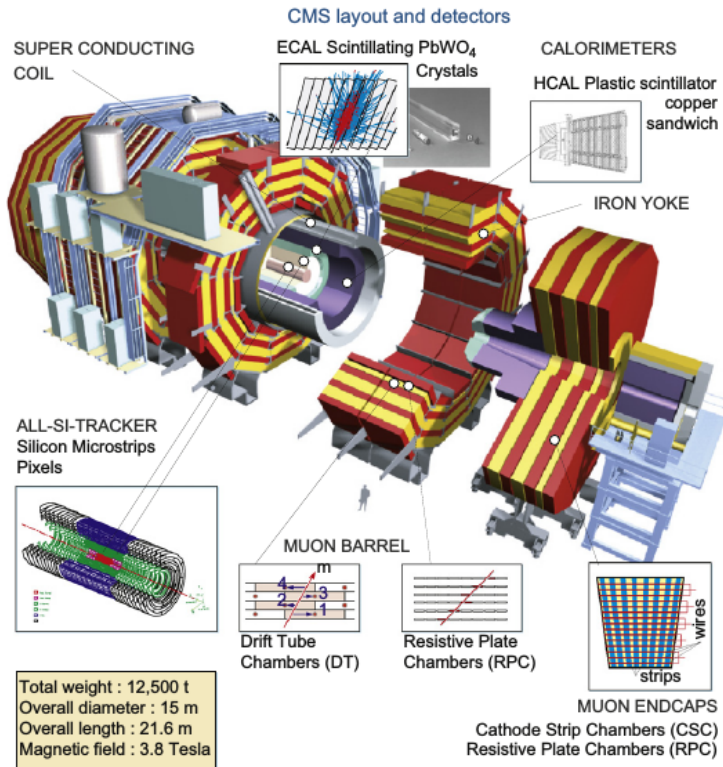


Figure 3.5: CMS Detector showing the different subdetectors and their material.

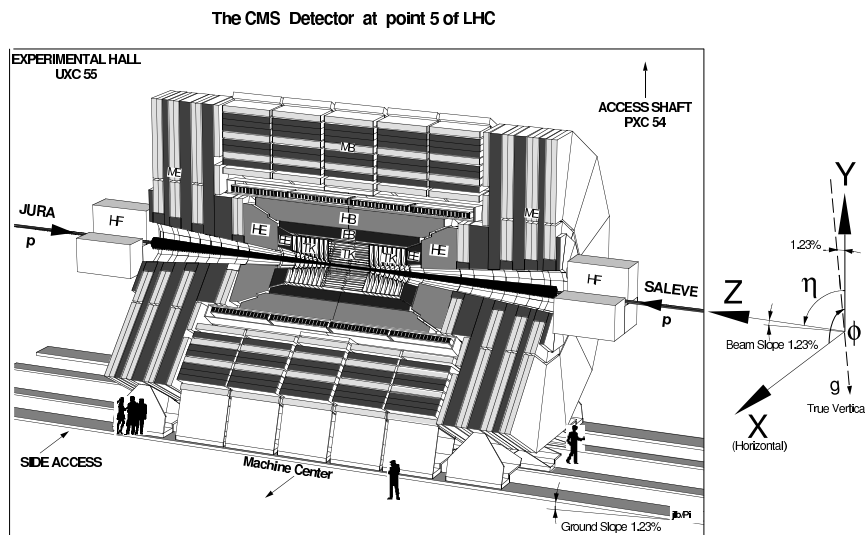


Figure 3.6: CMS detector schematic view with definition of  $x - y - z$  coordinates.

### CMS Detector and Resolution

Subdetector	Quantity	Resolution	Uses
Tracker	Momentum[GeV/c]	$\sigma_T/p_T \approx 1.5 \times 10^{-4} p_T + 0.005$	Silicon Pixels and Strips
ECAL	Energy[GeV]	$\sigma/E \approx 3\%/E + 0.003$	PbWO <sub>4</sub> Crystals
ECAL	Time[ns]	$\sigma(\Delta t) = \frac{N}{A_{eff}/\sigma_n} \oplus \sqrt{2}\bar{C}$	PbWO <sub>4</sub> Crystals
HCAL	Energy[GeV]	$\sigma/E \approx 100\%/E + 0.05$	Brass + Scintillator
Muon Chambers	Momentum[GeV/c]	$\sigma_T/p_T \approx 1\% \quad 50 \text{ GeV to } 10\% \quad 1 \text{ TeV}$	inner tracker + Muon Systems
Magnetic field	B-field strength[T]	3.8 T + 2 T	Solenoid + Return Yoke
Triggers	On/Off-line	Levels	L1(On-line) +HLT(Off-line)(L2+L3)

Table 3.2: CMS detector material, [29], and resolution(Time resolution:  $N \approx 35$  ns,  $\bar{C} \approx 0.070$  ns [49])

#### 3.2.2 Calorimeter

A CMS calorimeter absorbs a good fraction of energy of an incident particle and produces a signal with an amplitude proportional to the energy absorbed. This absorption is through the cascade production of secondary particles with energy of the incident particle directly proportional to the number of secondary particles produced. There are two types of calorimeters choices used in the CMS detector; the *Electromagnetic calorimeter* (ECAL); for absorbing the energy of electromagnetic particles such as photons and electrons and a *Hadronic calorimeter* (HCAL) made of more than one type of material for stopping and absorbing the energy of hadrons such as kaons and pions through strong interactions. The combined calorimeter detectors of CMS covers a region in  $|\eta| < 5$  making it nearly hermetic for good missing energy measurements. The ECAL

and HCAL are arranged in a nested fashion shown in figure 3.7 so that electromagnetic particles can be distinguished from hadronic particles by comparing the depth of the particle shower penetration in both calorimeters.

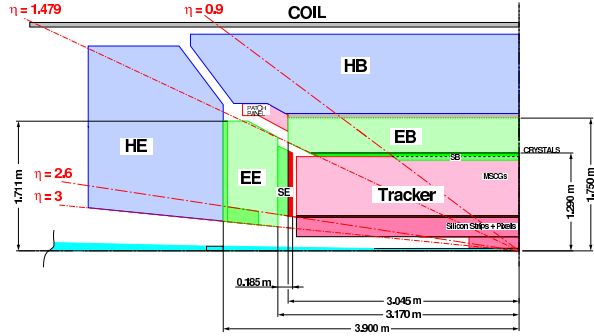


Figure 3.7: Schematic diagram of CMS calorimetry system with HCAL enclosing ECAL in the Barrel and Endcap regions.

### Electromagnetic Calorimeter

The electromagnetic calorimeter (ECAL) detects photons and electrons. High energy photons and electrons are detected through their interaction with the lead tungstate ( $\text{PbWO}_4$ ) crystals. During this interaction which happens either through electromagnetic showering or electron-positron pair production (*bremsstrahlung*), the incoming photon or electron deposit practically almost all of its energy. There are 75848 crystals in total mounted in a cylindrical geometry, with a barrel (EB) and an endcap (EE) structure. The choice of  $\text{PbWO}_4$  crystals as calorimetry material by CMS for operation in the LHC environment is because of its a high density ( $8.28 \text{ g/cm}^3$ ), short radiation length ( $X_0=0.89 \text{ cm}$ ) and a small Molière radius (22 cm). In a high radiation dose and fast timing (25 ns proton bunch spacing) environment like the LHC,  $\text{PbWO}_4$  crystals is preferred to other crystal materials for its high radiation resistance and a scintillation decay time which is comparable to the LHC bunch crossing interval of 25 ns and about 80% of the light is emitted in 25 ns. The probability of an electromagnetic object with high energy to interact either through *Bremsstrahlung* or *pair production* with the material in ECAL is proportional to the nuclear charge,  $Z$ , of the material.  $\text{PbWO}_4$  is a high  $Z$  material and this makes it once more the preferred material choice for electromagnetic calorimetry by CMS. The small Molière radius ensures that on average about

95 % of the electromagnetic shower energy is contained within a crystal crystal volume of about 9 crystals. This reduces the transverse spread of the electromagnetic cascade from multiple scattering of electrons and helps improve on the estimation of the transverse position of impact of an incident particle. It also provides a fine granularity for measuring the particle's energy by providing fewer overlap of particle signals. Its dense nature also allows for the electromagnetic shower to develop early and therefore likely to be fully contained within a compact device like CMS.

The EB section of the ECAL covers a pseudo-rapidity of  $|\eta| < 1.479$ . It has 61,200 crystals providing a granularity of 360 degree fold in  $\phi$  and  $(2 \times 85)$ -fold in  $\eta$ . The crystals are mounted in a quasi-projective geometry so that their axes make an angle of 3% with respect to a line vector from the nominal interaction vertex in  $\eta$  and  $\phi$  directions. This avoids cracks aligned with a particle's trajectory. A crystal in EB is approximately  $0.0174 \times 0.0174$  in  $\eta - \phi$  or  $22 \times 22 \text{ mm}^2$  at its front face and  $26 \times 26 \text{ mm}^2$  at its rear face. Each crystal is 230 mm long corresponding to about  $25.8 X_0$  radiation lengths. The crystal's radial distance measuring from the center of the face of the crystal to the beam line is 1.29 m. A number of crystals are placed in a thin-walled alveolar structure made with aluminum forming a *submodule*. Each submodule is arranged into 4 modules of different types according to their  $\eta$  position. There are about 400 to 500 crystals in each module and these 4 combined make one *supermodule* containing 1700 crystals. To reduce crystal reflective lost, the aluminum surface is coated to avoid oxidation leading to coloration. On the rear end of each EB crystal, two *Avalanche Photodiodes* (APD) is glued to collect the scintillating light from the crystals converting light into charge current which is further collected by the read-out electronics.

The endcap sector covers a pseudo-rapidity region of  $1.479 < |\eta| < 3.0$  with a Preshower (ES) detector made of silicon strip sensors interleaved with lead placed immediately in front of it. The purpose of the preshower is to identify photons from the decay of neutral pion,  $\pi^0 \rightarrow \gamma\gamma$  and also to help separate photons producing electrons through pair production from photons not producing electrons before their arrival at the EE. The endcap located on the  $+z$  side of the nominal interaction is denoted EE+ while the other located on the  $-z$  side is denoted as EE-. The longitudinal distance between the IP and the center of the surface of the EE crystals is 3.154 cm. Each endcap is divided into two halves called *Dees* with each Dee holding 3662 crystals. Crystals in EE with identical shape

are grouped into  $5 \times 5$  units called *supercrystals* (SC). The crystals in the SC form an  $x - y$  grid. Each crystal is 220 mm ( $24.7 X_o$ ) in length and has a front face and rear cross section of  $28.62 \times 28.62$  square mm and  $30 \times 30$  square mm, respectively. Vacuum Phototriodes (VPT) instead of APDs is glued on the rear face of each crystal for scintillating light conversion into electrical signals. The VPT is used in the EE because of its high resistance to radiation and smooth operation in a strong magnetic field environment. These APDs and VPTs are used because of their high gain relative to regular photodiodes with no gain and the fact that they are not affected by the high magnetic field. Although the light yield for  $\text{PbWO}_4$  crystals is rather low ( $\approx 70$  photons/ MeV), these photo-detectors have internal gain (50 for APDs and 10 for VPTs) and quantum efficiency of 75 % for APDs and 20 % for VPTs of the emission wavelength. This makes it possible that signals from incident particles with energies of a few to high GeV longer than noise.

The signals from the APDs and VPTs are digitized by voltage-sensitive analogue-to-digital converters and through fibre-optic links transported as light signals to the counting room located adjacent to the experimental cavern.

The energy resolution and geometry structure of the ECAL ensures that the photon or electron's arrival energy, time, position and even the direction through the shape of its electromagnetic shower in the crystals can be identified and measured with good precision.

### **Hadronic Calorimeter**

The CMS Hadron Calorimeter (HCAL) is comprised of four distinct subdetectors: the Barrel (HB), the Endcap (HE), the Outer Barrel (HO), and the Forward (HF). Unlike the ECAL, the HB, HE and HO subdetectors are scintillator-sampling calorimeters with embedded wavelength shifting fibers (WLS). HB, HE and HO uses brass plates as the inactive material and plastic scintillator with WLS as the active material. The brass plate is used for absorbing the hadronic shower which comprise of an *electromagnetic*(particles like  $\pi^0$ s,  $\eta$ s and other mesons generated in the absorption process and decay to  $\gamma$ s which develop electromagnetic (em) showers) and *non-electromagnetic* components. The plastic scintilator is divided into 16  $\eta$  sectors resulting in segmentation of  $\Delta\eta \times \Delta\phi = 0.087 \times 0.087$ . It was chosen for its long-term stability and moderate

radiation hardness. energy. The scintillating light through the WLS brings the light to hybrid photodiodes (HPDs) in the HB and HE. HPDs which have high electrical noise and will be replaced with silicon photon multipliers (SiPM) which have low noise during the current CMS detector upgrade. The HB and HE combine cover a region in pseudo-rapidity of  $|\eta| < 3$ . The HB covering the region  $|\eta| < 1.3$ , is divided into two-half barrel (HB+ and HB-) sections each composed of 18 identical  $20^\circ$  wedges in  $\phi$ . Each wedge is made of flat brass alloy and steel(only front and back plates) absorber plate. HE covers  $1.3 < \eta < 3.1$  and has plastic scintillation tiles with granularity of  $\Delta\eta \times \Delta\phi = 0.087 \times 0.087$  for  $|\eta| < 1.6$  and  $\Delta\eta \times \Delta\phi = 0.17 \times 0.17$  for  $|\eta| > 1.6$ . The HO is an extension of HB outside the solenoid and thus utilizes the solenoid coil as an additional absorber. It is used to identify the starting shower and to measure the shower energy deposited after HB. The first active layer of the scintillating tiles is situated directly behind the ECAL in order to actively sample low energy showering particles from the support material between the ECAL and HCAL.

The HF occupies a pseudo-rapidity region of  $3 < |\eta| < 5$ . Its purpose is to provide a closer to  $4\pi$  hermetic phase space coverage required for missing transverse energy calculation or MET. MET is the established signal for very weakly interacting particles like neutrino and supersymmetric particles like gravitino which travel through the detector undetected. HF consists of radiation hard quartz fibers embedded in steel absorbers running parallel to the beam axis. The signal from Cherenkov light emitted in the quartz fibers in response to charged particles makes it possible to detect all charge particles in the forward region. The HF calorimeter has long and short fibers for better sampling and to distinguish showers generated by electrons and photons from those generated by hadrons. The choice of quartz fibers is because of its high resistance to the high radiation in the forward detectors and its fast production of light through Cherenkov process.

For  $|\eta| < 1.48$ , the HCAL cells map on to  $5 \times 5$  ECAL crystal arrays to form calorimeter towers projecting outwards from near the nominal interaction point. In each tower, the energy in ECAL and HCAL cells is summed to define the calorimeter energy tower. The energy ratio of an HCAL tower to an ECAL in a calorimeter energy tower can be used to improve photons and electron identification.

### 3.2.3 Muon Chambers

Muons unlike electrons and hadrons do not deposit most of their energy in the calorimeters. They are capable of traveling across the entire CMS detector into the muon chambers. Muons produce tracks which run across the CMS detector starting from the silicon pixel and strip subdetector closest to the IP called the *Tracker* and depositing very little fraction of their energy in the calorimeters unto the muon chambers. The muon chambers use the process of ionization and a 2 T magnetic field from the return iron yokes (bending the tracks of charge particles) to measure the momentum of charged particles. The three different types of muon chambers used by the CMS are: the drift tubes (DT) chambers in the barrel, cathode strip chambers (CSC) in the endcaps and resistive plate chambers (RPC) glued to the DT and CSC chambers. Four layers or stations of DT/RPC and CSC/RPC are embedded in an interleaved style with the iron yoke for track reconstruction and triggering. Figure 3.9 is a longitudinal view of the CMS detector showing the position of the muon stations. The DT and CSC record track segments characterized by the position of the track and the bending angle. This information is used to determine the precise transverse momentum and charge of particles during particle reconstruction. The RPCs(DTs and CSC will also be used after the current detector upgrade) are dedicated L1 trigger chambers used to determine the candidate muon's approximate transverse momentum and proton bunch crossing number. The RPC has a timing resolution of about 3 ns.

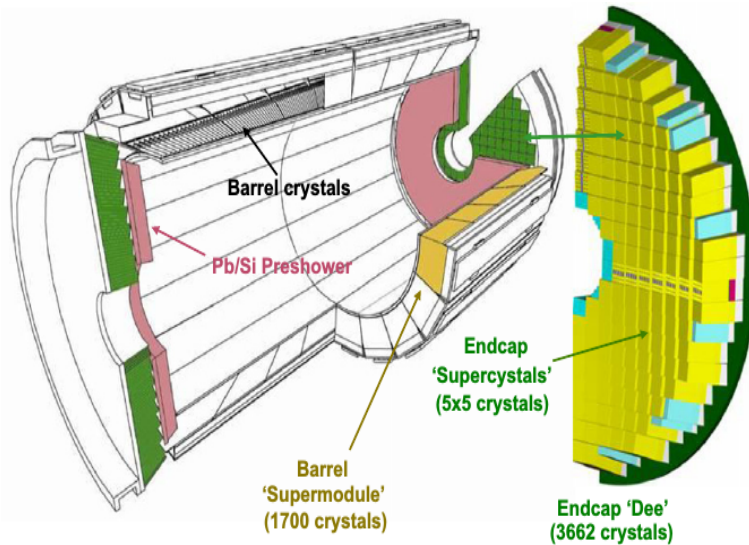


Figure 3.8: Layout of the CMS electromagnetic calorimeter showing the arrangement of crystal modules, supermodules in the barrel with the preshower in front of endcap with supercrystals.

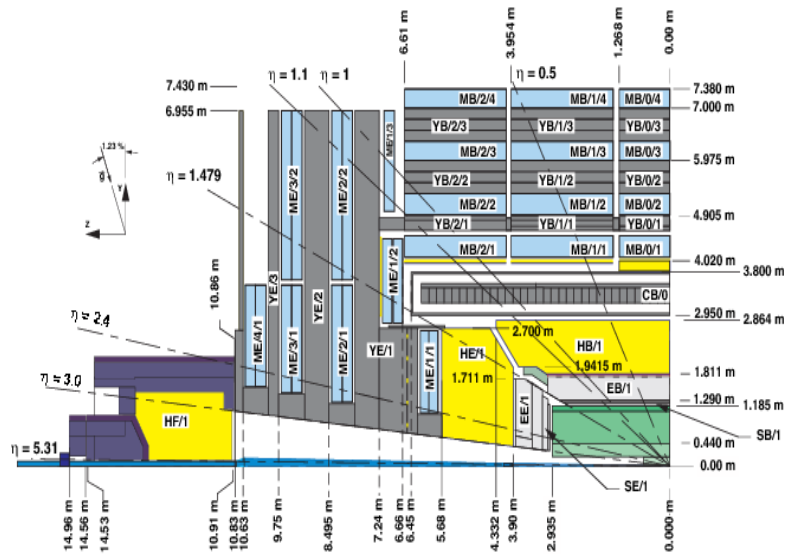


Figure 3.9: Cross section view showing the coverage range of CMS sub-detectors and their longitudinal distance from the IP.

### 3.2.4 Triggering

In CMS, there are a billion interactions including *pile up* (PU) happening each second. This means data from each 25 ns proton-proton collision has to be processed and stored before the next collision happens. Also, since not all these collisions produce interesting physics events, we have to be capable of selecting only interesting physics events produced from proton-proton collisions with sufficient energy. The process of selecting such interesting events is called *triggering*. CMS uses a two level triggering system for selecting interesting events produced with enough energy from collisions. The comprise of the *Level-1* (L1) and *High Level Triggers* (HLT) triggers.

The L1 triggers is a hardware designed electronics system implemented in FPGA and ASIC technology and uses information from the calorimeter, muon trigger and a global trigger board. The global trigger board makes the final decision based on the calorimeter and muon triggers to reject or keep an event for further processing at the HLT trigger. The L1 trigger is responsible for selecting the best 100,000 events/second from the initial 1 billions events/second produced.

The HLT is a software comprised of implemented selection algorithms running on a farm of more than 1000 standard computers. These complex algorithms include instructions like, match tracks to hits from the muon chambers, select energy deposits above a certain threshold in the calorimeters with no tracks for electromagnetic objects, and begins the first step of event selection. Just like the L1 trigger, the HLT uses assimilated and synchronized information from different parts of the CMS detector to create the entire event. By the time this selection process is complete, there are now only 100 events/second with the remaining 99,900 thrown away. Taking an average event size to be 1 Megabyte, in a stable and effective LHC proton collision period of a year or  $10^7$  seconds, CMS produces about a Petabyte of data which is stored and used later for offline physics analysis.

## Chapter 4

# Time Reconstruction and Resolution

### ECAL Time Overview

The Electromagnetic Calorimeter (ECAL) was designed to precisely measure the energy of electrons and photons with a target barrel resolution of 0.5% for photons with energy more than 50 GeV. In addition to energy measurements, the combination of fast scintillation for PbWO<sub>4</sub> crystals, the electronic pulse shaping and sampling rate of 40 MHz allow for excellent time measurements. The time measured by each channel is reconstructed from 10 discrete samples of the digitized analog pulse height using a time reconstruction algorithm. A pulse shaping chip in each channel, matching the pulse shape with less than 1% non-linearity, ensures a linear and uniform pulse height from among all the channels in ECAL [40, 41, 42].

#### 4.1 Electromagnetic Calorimeter Readout Electronics

The scintillating light from the PbWO<sub>4</sub> crystals is readout and converted into electric charge using Avalanche Photo-Diodes (APD) and Vacuum Photo-Triodes (VPT) in the barrel and endcap detector regions, respectively.

The ECAL electronics readout and control system comprise of a Front End (FE) and an Off Detector (OD) electronics. The FE electronics, made with radiation-hard ASIC

chips to withstand the high radiation dose from collisions are installed inside the detector volume at the back of ECAL, while the OD electronics, responsible for trigger primitive generation, event triggering and timing control is in the upper counting room. The FE electronics is connected to the OD electronics by 100 m radiation hard Gigabit Optical fiber Links (GOL) for transporting the optical data stream. Among the ASIC chips of the FE board, is a Clock and Control Unit (CCU) chip which enables the exchange of control information between the OD and the FE electronics through a Clock and Control link.

Each FE receives signals from a group of crystals typically forming a  $5 \times 5$  crystals matrix. A FE board, shown in right schematic diagram of Figure 4.1, hosts five Very Front End (VFE) boards with each VFE board holding five analog channels. Each channel, shown in the left schematic diagram of Figure 4.1, consists of a Multi-Gain Pre-Amplifier (MGPA) and 12 bit Analog-to-Digital Converted (ADC), which are used to amplify, shape and digitize the signal coming from the Photo-Diodes.

The MGPA chip uses 3 gain ranges with gain ratios of 1, 6 and 12 to span the overall dynamic range of the signal which can go from a few MeV up to TeV. Equipped with a Capacitor-Resistor-Resistor-Capacitor (CR-RC) filter with a pulse shaping time of 40 ns and less than 1% of non-linearity, the MGPA ensures a linearity and pulse shape matching across all three ranges which allows for precise pulse shape reconstruction.

The required readout and precision performance demands a multi range 12-bit ADC chip with a sampling frequency of 40 MHz to digitize the analog pulse signal of the highest unsaturated range into 10 discrete samples, with an electronic noise of about 40 MeV.

The digitized data are stored in pipeline buffers until a Trigger Level 1 (LV1) accept decision is made. At the same time the digitized data are sent to a digital signal processing FERNIX chip which performs Trigger Primitive Generation (TPG) for the LV1 trigger system. The TPs are sent to the Trigger Concentration Card (TCC) on the OD electronics at a rate of 1 word/25 ns. Upon a positive trigger LV1 decision, the data samples corresponding to a single event are transferred to primary event buffers which are eventually merged and sent to the Data Concentration Card (DCC) through readout links at 800 Mbps. The crystal readout data from the FE board is collected by the OD electronics DCC.

The OD board hosts the DCC, TCC and a Clock and Control System card (CCS). The TCC completes TPG process by combining the TPs generated and transmit them to the regional Calorimeter Trigger system while the CCS is tasked primarily with distributing fast timing signals (LHC 40 MHz clock and trigger commands) to the FE and OD electronics and to synchronize their operation. A common clock distribution serving  $5 \times 5$  readout unit of the FE reduces any needed channel-to-channel synchronization.

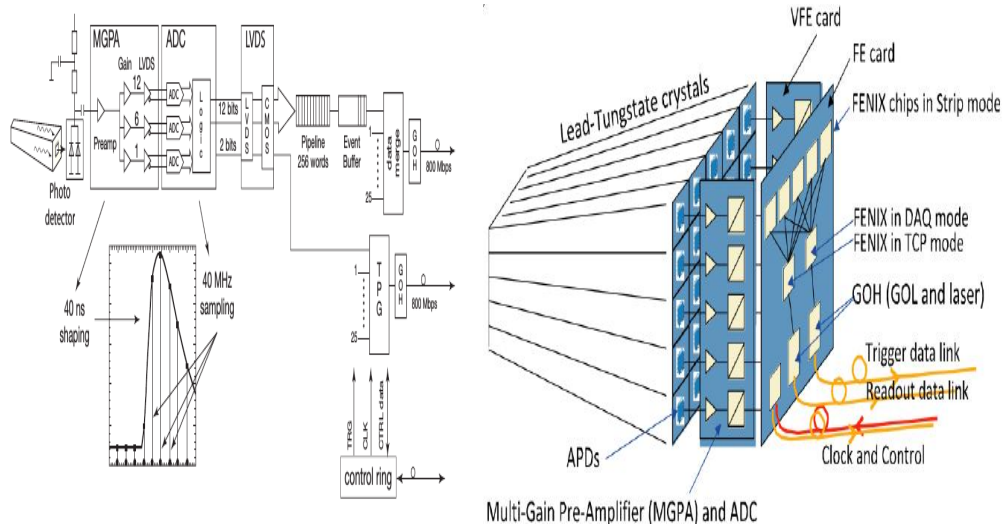


Figure 4.1: Schematic diagram of the ECAL electronics readout for a single channel (left) and the entire Trigger Tower (TT) or Front End (FE) Card (right).

## 4.2 Time Reconstruction

An analog pulse shape from a single channel is shown in Figure 4.2(a). Overlaying the pulse shape are typical 10 digitized samples in red. The first three samples are taken in the absence of a signal and correspond to the pedestal. The ADC chip responsible for the digitization, has a sampling frequency of 40 MHz, i.e. one sample is made every 25 ns, which is the same rate as the LHC proton-proton bunch collision frequency of one bunch crossing every 25 ns, and a total time of 250 ns corresponding to the 10 digitized samples is covered. In addition, the timing phase of sampling within the 25 ns interval is adjusted so that the maximum of the signal pulse shape corresponds to one of the samplings to within 1 ns. A time reconstruction algorithm uses the 10 digitized samples

to measure the time of a single channel by finding the precise time,  $\mathbf{T}_{\max}$ , corresponding to the maximum of the pulse shape [43, 44].

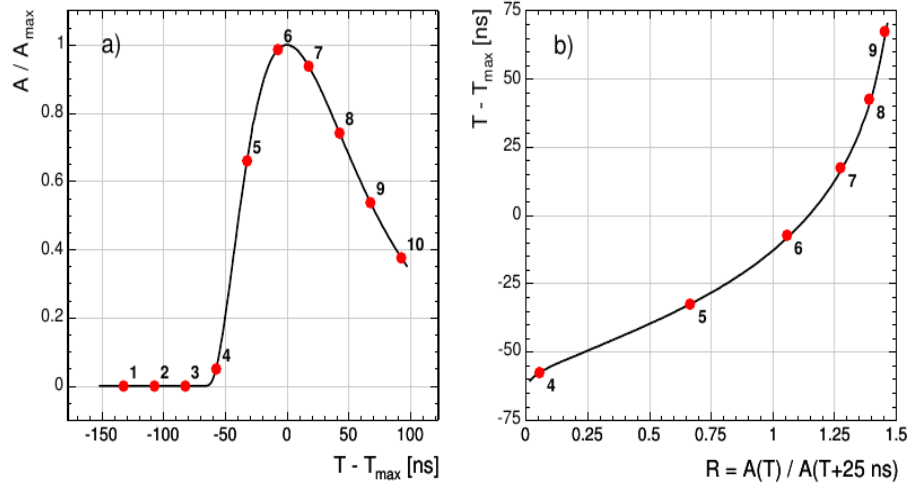


Figure 4.2: (a) A measured ECAL pulse shape for a single channel. (b)  $T - T_{\max}$  Vs  $R(T)$  relationship whose inverse is  $T(R)$ . Solid line is pulse shape from test beam while dots are typical 10 discrete samples corresponding to signal from proton-proton collision.

The pulse shape is used to determine  $\mathbf{T}_{\max}$  in the following way. The height ratio

$$R_i = A(T_i)/A(T_{i+1}), \quad (4.1)$$

where  $T_i$  is the time when the  $i^{\text{th}}$  pulse height sample is taken, is uniquely determined from the pulse shape. The pulse height ratio,  $R_i(T_i - T_{\max})$ , shown in Figure 4.2(b), is a function of the time that the pulse height of the first of a pair of samples is taken relative to the time of the maximum pulse height,  $\mathbf{T}_i - \mathbf{T}_{\max}$ . From the inverse of this function,  $T(R)$ , we obtain  $\mathbf{T}_{\max} = T_i - T(R_i)$  and the uncertainty,  $\sigma_i$ , for each  $R_i$  point. The uncertainty on each measurement is a product of the derivative of the function,  $T(R)$ , and the uncertainty on the value of  $R_i$  which itself depends on three separate uncertainties: the noise fluctuation ( $\sigma_n$ ) of each sample, the uncertainty in the estimation of the pedestal value, which is always subtracted from the measured value, and the truncation during 12-bit digitization.

A precise value for  $\mathbf{T}_{\max}$  is, most of the time, obtained using the ratios  $R_4$  through  $R_7$ . The other ratios,  $R_8$  and  $R_9$  are not used for the estimation of  $T_{max}$  because their associated uncertainties are large due to the large slope of the  $T(R)$  function. A weighted average of each  $T_{max,i}$ , and  $\sigma_i$ , obtained from ratios  $R_4$  through  $R_7$  is given as

$$\mathbf{T}_{\max} = \frac{\sum \frac{T_{max,i}}{\sigma_i^2}}{\sum \frac{1}{\sigma_i^2}} , \quad \frac{1}{\sigma_T^2} = \sum \frac{1}{\sigma_i^2} \quad (4.2)$$

where the sum is from  $i = 4, \dots, 7$ , gives the best estimate of  $\mathbf{T}_{\max}$  and uncertainty.

## 4.3 ECAL Time Performance from Test Beam

### 4.3.1 ECAL Time Resolution

The intrinsic time resolution of ECAL, measured during test a beam study, can be parametrized using the standard deviation of a Gaussian distribution. It consists of three main contributions which can be summed in quadrature since they are uncorrelated. These three contributions are the noise, stochastic and constant terms. The *Noise* ( $N$ ) term arises from the electronic noise, coherent movement of the baseline and effects of overlapping hits. The *Stochastic* term ( $S$ ) arises from fluctuations in the number of photons collected during the sample times. Lastly, the *Constant* term ( $C$ ), whose contribution is independent of the energy deposited and arises from both variations in the point of shower initiation within the crystal, variations in the pulse shape for each channel and calibration effects. The full parametrization of the time resolution with all three contributions is given as

$$\sigma^2(t) = \left( \frac{N}{A/\sigma_n} \right)^2 + \left( \frac{S}{\sqrt{A}} \right)^2 + C^2, \quad (4.3)$$

where  $A$  is the measured amplitude in ADC counts corresponding to the energy deposited and  $\sigma_n$  is the intrinsic noise in the amplitude for an individual channel.  $\sigma_n$  has a value of 42 MeV and 140 MeV in the barrel and endcap, respectively.  $N = 33$  ns has been estimated from Monte Carlo (MC) simulation studies and the contribution from the stochastic term, ( $S$ ) is small, with a value of  $S < 7.9$  ns·MeV<sup>1/2</sup>.

The measured timing resolution was obtained from the Gaussian distribution of the difference in the time of two crystals sharing energy and belonging to the same electromagnetic shower, after about 25% of the barrel and endcap crystals were exposed to electron beams with energy between 15 GeV and 250 GeV at H2 and H4 test beam facilities at CERN. This method of measuring  $\sigma(t)$  using the time difference of two crystals reduces the contribution to the constant term arising from crystal-to-crystal synchronization. And since the stochastic term is small, the parametrization of the time resolution expressed in Equation 4.3 can be reduced to

$$\sigma^2(t_1 - t_2) = \left( \frac{N}{A_{eff}/\sigma_n} \right)^2 + 2\bar{C}^2 \quad (4.4)$$

where  $A_{eff} = A_1 A_2 / \sqrt{A_1^2 + A_2^2}$ , while  $t_{1,2}$  and  $A_{1,2}$  are the times and amplitudes of the two crystals.  $\bar{C}$  is their residual constant term contribution.

In practice, the time resolution is measured from the standard deviation of a Gaussian fit to the time distribution from each slice of  $A_{eff}/\sigma_n$  of the  $A_{eff}/\sigma_n$  distribution. The resulting distribution of  $\sigma(t_1 - t_2)$  of these standard deviations plotted against  $A_{eff}/\sigma_n$  is used to extract the noise and residual constant terms. The result presented in Figure 4.3, of the test beam study gives a noise factor  $N = (35.1 \pm 0.2)$  ns which agrees with our Monte Carlo estimate to within 6%.

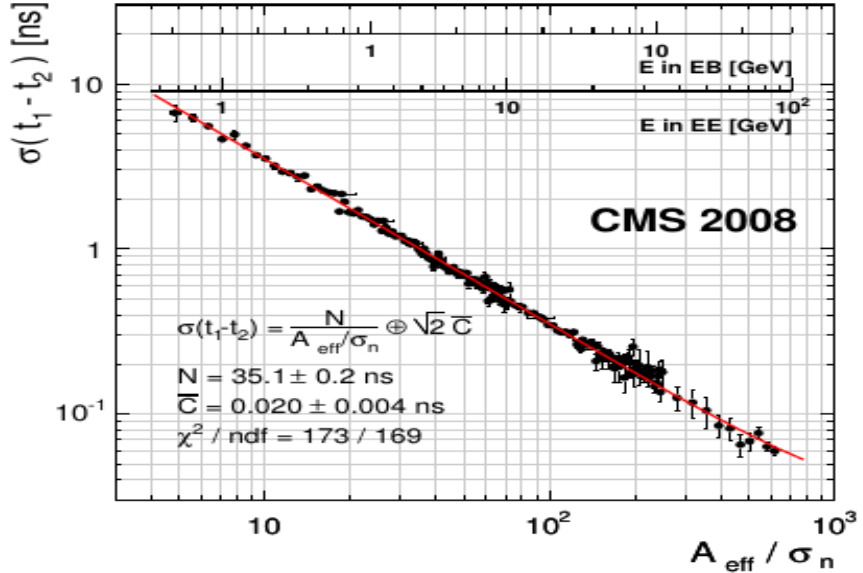


Figure 4.3: Difference in the time measurements as a function of  $A_{\text{eff}}/\sigma_n$  of two crystals sharing an energy and belonging to the same electromagnetic shower obtained during electron test beam measurements. The single crystal energy scales for barrel (EB) and endcap (EE) is overlaid. The fitted results give  $N = (35.1 \pm 0.2)$  ns and  $\bar{C} = (20 \pm 4)$  ns.

Knowing that it takes on average 4.3 ns for a photon to reach the ECAL surface produced from the proton-proton interaction point, this demonstrates an intrinsic time resolution of 2% for photons with energy  $E > 20$  GeV in the barrel.

#### 4.4 ECAL Time Performance from Collision

The time resolution during LHC proton-proton ( $pp$ ) collisions is expected to be worse than what the test beam study show since factors present only during LHC  $pp$  like LHC clock time variations over extended time, timing bias with energy due to gain transition and loss in crystal transparency due to radiation, which leads to difference in pulse shape, can affect the time resolution. To reduce the impact of these effects on the time resolution, we synchronize all the ECAL crystals using  $pp$  collision data.

#### 4.4.1 Time Calibrations

Variations in the crystal time may be caused by the difference in pulse shape or by clock drift over time or time shifts introduced during CMS detector repairs. These variations, about 1 to 3 ns on average, can be removed by aligning in time or synchronizing all 75,848 PbWO<sub>4</sub> crystals in ECAL. The crystal time alignment is performed once or twice every month and ensures that there is a uniform response by all the crystals to photons produced from  $pp$  collisions, at interaction point, and traveling along a straight path with speeds close to the speed of light to ECAL. Crystal time alignment equally guarantees the synchronization of most particles of an event and assigns each event to the correct LHC proton bunch crossing at the trigger level.

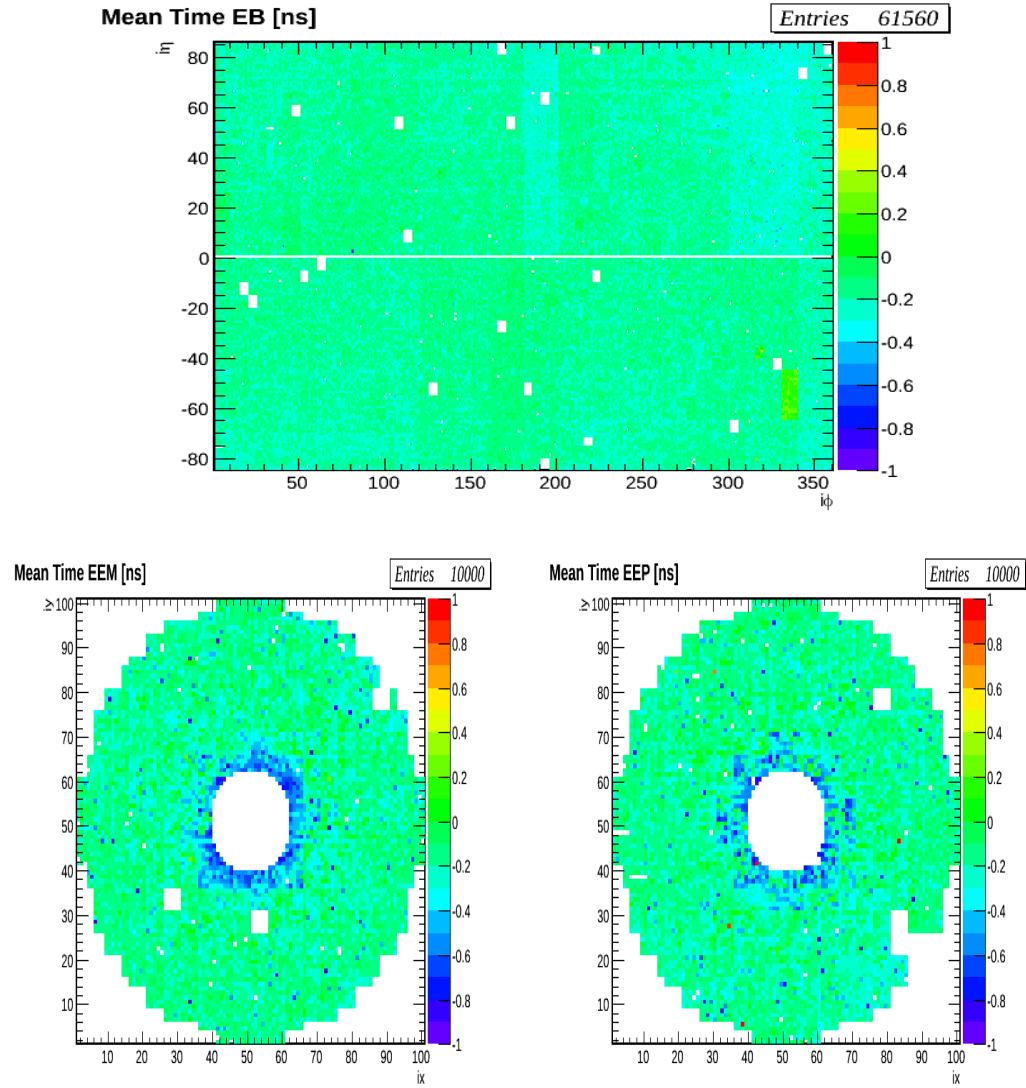
The presence of the “ $T_{max}$  Phase”, the difference in pulse shape between each crystal, variation in the time of flight by a few nanosecond (ns) and the different intrinsic delays in each channel motivates a time calibration at two separate levels. At the FE electronics, a timing synchronization is performing by adjusting the time of  $5 \times 5$  crystals or trigger tower in steps of 1.04 ns. This process, known as *Hardware Synchronization*, involves determining the trigger tower time constants needed for time aligning all the trigger towers using  $pp$  collision data.

At offline, during energy hits reconstruction or rechits in the transition from uncalibrated to calibrated hits, a time constant, which is the average of the measured time by a crystal over many events, is used to time align individual crystals in ECAL.

#### Offline Time Calibration

The offline time aligning is performed during event reconstruction in CMS. The time constant used by each crystal is the reverse sign of the average time of all the reconstructed energy deposits (rechits) by the crystal. New sets of time constants are produced each month throughout the entire LHC run period. Each set of time constants produced has an *interval of validity* (IOV). A total of 17 IOV time constants were produced for the entire LHC run in 2011 and 44 IOV time constants for 2012. The time constant for each crystal is produced using  $pp$  collision data of mostly triggered photons so as to minimize any time of flight delay that might affect the average time over events for each crystal. The maps in Figure 4.4, show two dimensional distribution of the average time (time

calibration constants) for each of the 61,200 crystals in EB and 14648 crystals in EE. The figure shows each crystal average time before (*top 3 plots*) and after (*bottom 3 plots*) calibration. More information about crystal time calibration for the entire LHC Run 1 is found in [45].



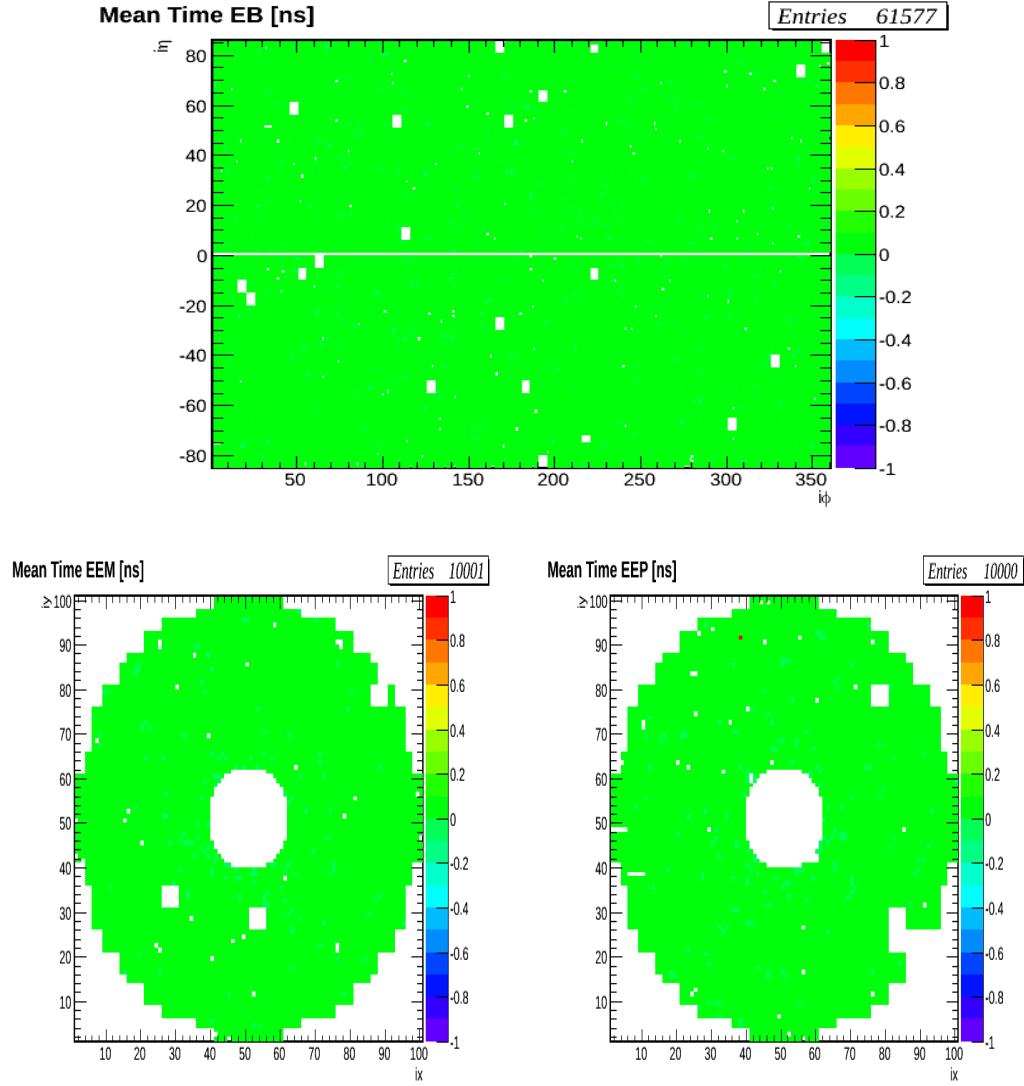


Figure 4.4: *Top 3*: Time calibration maps showing the distribution of mean time for each channel/PbWO<sub>4</sub> crystal in EB (top) and EE (below: EE-(left), EE+(right)) before calibration. *Bottom 3*: Time calibration maps showing the distribution of mean time after calibration. After calibration most crystals have an average time of zero(GREEN).

### Hardware Time Calibration

Time alignment at the trigger tower level using the average time of  $5 \times 5$  crystals for events from  $pp$  collision or laser is performed during data recording by the CMS detector.

### Hardware Time Calibration With Collision

Using  $pp$  collision data, the time alignment is performed during CMS data recording using time constants derived from data recorded by the CMS detector. The frequent down times of the CMS detector during stable  $pp$  beam collision needed for the FE or trigger tower time adjustments to be made is one of the causes for the difference between the luminosity recorded by CMS detector compared to luminosity delivered by the LHC. This makes hardware time adjustments using collision data less desirable and as a result a laser based time alignment method which requires no CMS detector downtime can be used.

### Hardware Time Calibration With Laser

The ECAL laser system comprise of two lasers, a 440 nm wavelength (close to peak emission for PbWO<sub>4</sub> crystals) laser for monitoring crystal transparency losses and a 796 nm wavelength laser for monitoring readout electronics chain from photodetectors to the electronics (i.e. APDs to ADCs). Both lasers have a jitter of less than 4 ns and as a result, the time from the lasers is averaged over 600 event pulses. The time for each crystal from the laser is expected to be the same as the time from collision data and is represented as  $T_{\text{MAX}}^{\text{APD}}$ . The laser system is also equipped with a fast acquisition card called MATACQ. The time for each channel recorded using the Matacq is also averaged over 600 event pulses and is denoted  $T_{\text{MATACQ}}$ . The difference,  $T_{\text{MAX}}^{\text{APD}} - T_{\text{MATACQ}}$ , of the two times, averaged over the 25 crystals of a Clock and Control Unit (CCU) is used as the time for each CCU,  $t_{\text{CCU}} = \langle T_{\text{MAX}}^{\text{APD}} - T_{\text{MATACQ}} \rangle$ . To obtain the time shift of 25 crystals belonging to the same Front End (FE) electronics, we monitor for change of this average time before ( $t_{\text{CCU}}^B$ ) and after ( $t_{\text{CCU}}^A$ ) hardware intervention during detector maintenance. The time difference,  $\Delta t_{\text{CCU}} = t_{\text{CCU}}^A - t_{\text{CCU}}^B$ , averaged over all the 25 crystals, i.e.  $\langle t_{\text{CCU}}^A - t_{\text{CCU}}^B \rangle_{25}$ , gives the time shift, and the time calibration constant for the CCU is of opposite sign so that after correcting, the average time of the CCU is zero. This is done for all the 68 CCUs in a given supermodule (SM) or front end detector (FED). The global time shift of a given FED is caused by the non-homogeneous laser light distribution on all CCU or trigger towers. Each FED has 1,700 PbWO<sub>4</sub> crystals and we produced laser based time calibration constants for all its crystals. Time alignment using laser data is described in detail here [46].

#### 4.4.2 Time Bias

The time reconstruction algorithm assumes smooth performance for all energy values of the incident particle. However, during data recording in LHC Run 1, it was observed that for very energetic particles with energy above 160 GeV in EB and 250 GeV in EE, an inherent bias in the time is introduced by the multi-gain pre-amplifier electronics at gain transition points due to not-quite-high-enough slew rate of the amplifiers. The time bias was also observed for very low energy values of less than 2 GeV. The first gain transition point (Gain-1) of the multi-gain pre-amplifier occurs near 4095 ADC counts corresponding to 159.744 GeV in EB and 258.048 GeV in EE. The subsequent Gain-6 and 12 transitions occur at energy values of TeV. The full conversion of the energy of a particle recorded by a crystal in ADC counts to GeV is expressed as;  $E_i = G \cdot S_i(t) \cdot C_i \cdot A_i$ , where  $A$  is the amplitude from the pulse shape in ADC counts,  $G$  is the ADC-to-GeV conversion factor equal to 0.039(0.063) in EB(EE),  $C_i$  is the inter-calibration coefficients accounting for individual channel response to the electromagnetic shower and  $S_i(t)$  is the correction term obtained from laser accounting for radiation-induced channel response.  $S_i$  changes over time.

The observed time bias is corrected on an energy dependent basis during event reconstruction and is CMS event reconstruction software (CMSSW) release dependent. Figure 4.5 show the comparison between two CMS event reconstruction software releases, CMSSW44X, where these time bias corrections were made for the first time and CMSSW53X, where the second set of time bias corrections were applied. Evidently, the average time displayed in both CMSS44X and CMSS53X show the disappearance of the time bias after the time bias corrections were made again in CMSSW53X for all values of the incident particle's energy.

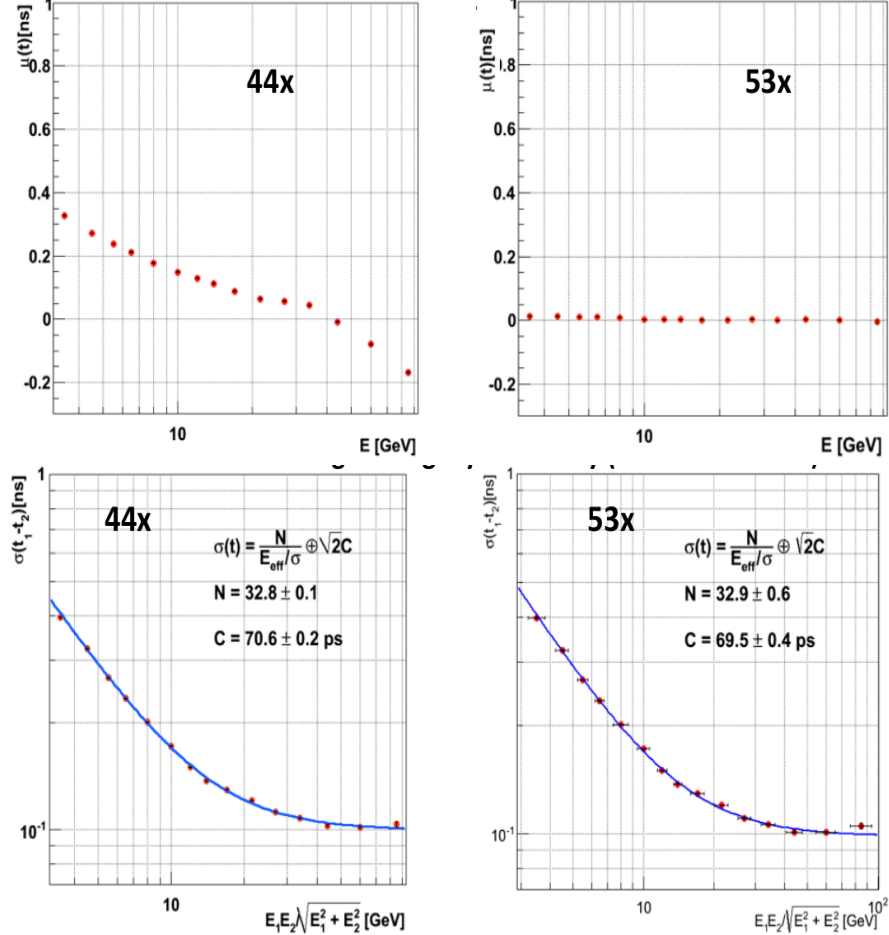


Figure 4.5: Distribution of mean time ( $\mu$ )[top row] and time deviation ( $\sigma$ )[ bottom row] as a function of crystal energy for EB prior (left) and after (right) time bias corrections depending on energy have been applied.

#### 4.4.3 ECAL Time Performance With Z Bosons

We evaluate the precision of ECAL timing measurements, during  $pp$  collisions, by studying the time measurements in events with the decay of the Z boson to an electron pair, i.e.  $Z \rightarrow e^-e^+$ . The selection for Z candidate events require that each electron have a transverse energy above 10 GeV and the reconstructed Z mass is within,  $60 \text{ GeV}/c^2 < m_{e_1, e_2} < 120 \text{ GeV}/c^2$ , to ensure that the sample is pure.

We use the standard deviation,  $\sigma_{\text{eff}}$ , of the difference in arrival time of the two electrons to evaluate ECAL timing performance. This standard deviation is obtained from the

difference in the seed time,  $t_{seed}$ , of each electron's electromagnetic shower after correcting for the extra time due to the bending of the electron's travel path inside the CMS magnetic field of 3.8 T. In Figure 4.6, we present the distribution of the time difference,  $t_{electron1} - t_{electron2} = t_{seed1} - t_{seed2}$ , and the value of the time resolution ( $\sigma_{eff}(t_1 - t_2)$ ) of both electrons with the time of flight adjustments made while in Figure 4.7, we show the absolute time resolution ( $\sigma_{eff}(t_{seed})$ ), obtained from the time distribution of a single electron's seed crystal time without correcting for the time due to the bending of the electron's flight path.

A time resolution of 0.232 ns in EB and 0.384 ns in EE is measured with a single precision resolution of 164 ps in EB and 272 ps in EE shown in Table 4.1.

The absolute time resolution,  $\sigma_{eff}(t_{seed})$ , for a single crystal is measured to be 386 ps for EB and 388 ps for EE. However, if we remove the contribution from the spread in time,  $\sigma(t_{collision})$ , due to the finite time it takes for the two proton bunches of length 5.5 cm to collide; which is about  $\sigma(t_{collision}) = \sigma(t_Z) = 183$  ps, we obtain an improved absolute time resolution of 340 ps in EB and 342 ps in EE.

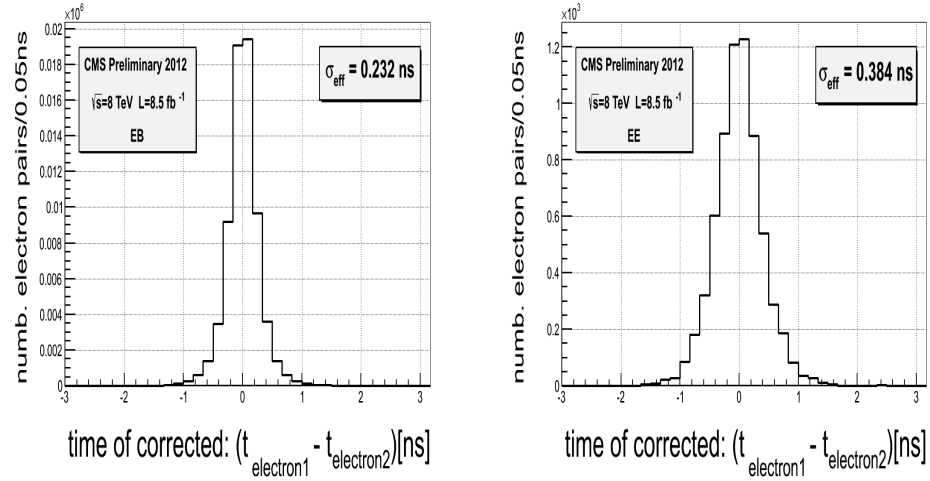


Figure 4.6: Ecal time difference between the two reconstructed electrons in  $Z \rightarrow e^-e^+$  decay. The electron time is the seed (crystal with highest energy deposit) time with additional correction due to the time of flight of the electron in EB and EE.

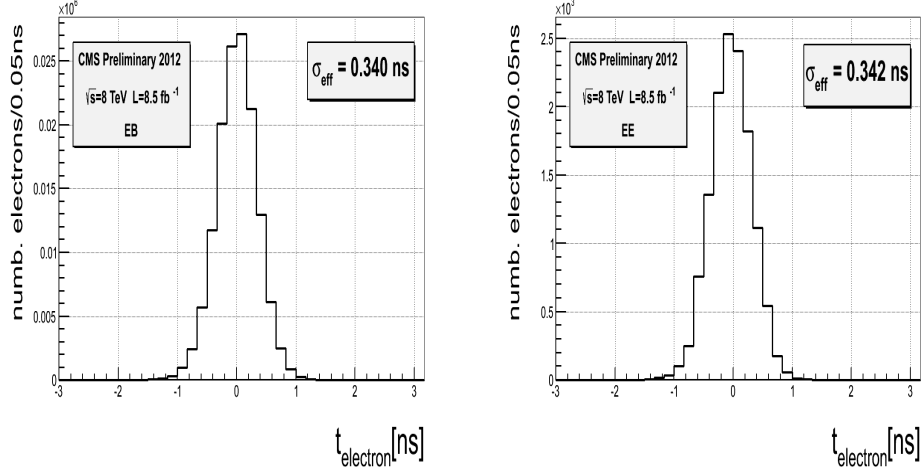


Figure 4.7: Ecal absolute time of a single reconstructed electron in  $Z \rightarrow e^-e^+$  decay. The electron time is the seed (crystal with highest energy deposit) time of the electron in EB and EE.

We also investigate the timing bias attributed to the FE electronics using events with  $Z \rightarrow e^-e^+$  decay. Figure 4.8 (left) show the time resolution measured in the case where the seed crystal time is measured from both crystals belonging to the same FE electronics compared to the other case, shown in Figure 4.8 (right), where the seed crystal time is read from crystals belonging to two different FE electronics. The Constant term,  $C$ , for the same FE electronics is about 67 ps while that for different FE electronics is 130 ps, which indicates that electronic readout de-synchronization contributes to the worsening of the time resolution [47, 48, 49, 50, 51].

The ECAL time resolution for the entire LHC Run 1 of 2011 and 2012, comparing the absolute and single precision time measurements is summarized in Table 4.1.

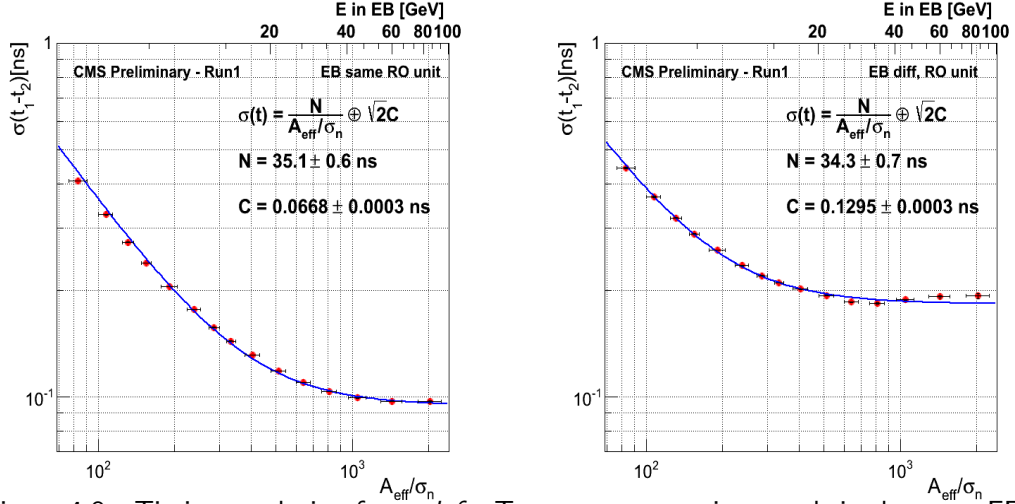


Figure 4.8: Timing resolution from: *left*: Two most energetic crystals in the same FE electronics, *right*: Two most energetic crystals belonging to different FE electronics, as a function of effective amplitude( $A_{eff} = A_1 A_2 / \sqrt{A_1^2 + A_2^2}$ ) normalized to noise in EB. Both crystals are from reconstructed electrons in  $Z \rightarrow e^- e^+$  events.

### ECAL Timing Resolution

2011	
	Absolute Time
	$\sigma_{eff}(t_{seed})[\text{ps}]$
<b>EB</b>	376
<b>EE</b>	356
2012	
	Absolute Time
	$\sigma_{eff}(t_{seed})[\text{ps}]$
<b>EB</b>	340
<b>EE</b>	342

Table 4.1: ECAL timing resolution absolute time and single precision for 2011 and 2012 of LHC Run 1.

# Chapter 5

## Event Reconstruction

### 5.1 Event Reconstruction Overview

Event reconstruction is the process of reconstructing particles and their four momenta using raw data read from the electronics of the different CMS subdetectors. Event reconstruction is archived in CMS using the *Particle Flow* (PF) algorithm which reconstructs all the particles in an event, individually, using information from all CMS subdetectors. It is also possible to reconstruct particles without using the PF algorithm.

### 5.2 Supercluster Reconstruction

A clustering algorithm groups energy deposits from individual crystals to form clusters which are eventually grouped together forming clusters of clusters known as *superclusters*. A cluster is either a  $3 \times 3$  or  $5 \times 5$  crystals energy matrix. About 94% (97%) of the incident photon or electron energy is deposited in the  $3 \times 3$  ( $5 \times 5$ ) crystal matrix in  $(\eta, \phi)$  directions in the barrel and  $(x, y)$  directions in the endcaps.

The 3.8 T magnetic field and material in front of the calorimeter causes electrons and photons radiating off electrons to deposit their energy in a cluster of crystals spread in  $\phi$  and because of the spread in  $\phi$ , the clustering algorithms starts building clusters with a seed crystal (crystal with the maximum energy) and continues within a narrow window in  $\eta$  by summing the crystal energies along  $\phi$ , which is the direction of the energy spread due to the magnetic field. Figure 5.1 is a schematic picture showing the direction (left

Figure) of the clustering process in  $(\eta, \phi)$  directions in the barrel and the fraction (right Figure) of electromagnetic energy in a typical cluster.

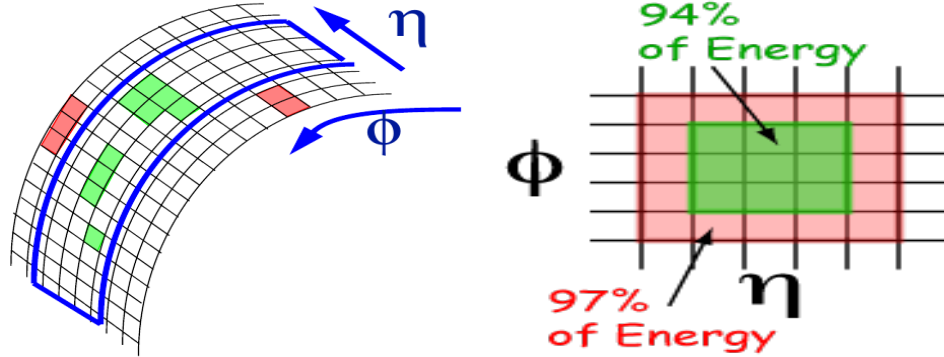


Figure 5.1: Superclustering algorithm direction (left) in the  $(\eta, \phi)$  plane in EB and fraction (right) of electromagnetic shower energy coverage in a crystal energy matrix.

Two major clustering algorithms are used in ECAL: the *hybrid* (EB) and *island* (EE) algorithms.

- **Hybrid Supercluster Algorithm:** This algorithm is used for making super clusters in the barrel (EB). It takes advantage of the  $\eta - \phi$  geometry of barrel crystals by taking a fixed 3 or 5 crystals in  $\eta$  and dynamically search and sum separate crystals energy along  $\phi$ . The Hybrid algorithm takes advantage of the knowledge of the lateral shower shape along the  $\eta$  direction. The supercluster consists of basic clusters which are usually  $3 \times 3$  crystals energy matrix.
- **Island Supercluster Algorithm:** This algorithm is used for making clusters in the endcap (EE). It begins by finding the seed crystal of the electromagnetic shower with maximum energy above a certain energy threshold. Using the seed crystal position, adjacent crystals are examined and added to a cluster until a rise in energy where a crystal belonging to another cluster or crystal that has no energy hit is reached. For each crystal to be added to the cluster, its energy read must be positive, it must not have been assigned to another cluster and the previous crystal added in the same direction must have a higher energy. These non-overlapping clusters (usually a  $5 \times 5$  crystals energy matrix) finally form a supercluster.

### 5.3 Track and Vertex Reconstruction

The track of a charge particle is reconstructed using *hits* which are themselves reconstructed from the ionization left in silicon by the passage of the charge particle. The particle's helical trajectory or track, reconstructed from these hits, is used to measure the it's momentum and direction.

Track reconstruction uses several algorithms with the main algorithm used for reconstructing the tracks of charge particles produced from  $pp$  collisions called the *Combinatorial Track Finder* (CTF). The CTF integrates track fitting and pattern recognition, building tracks from an initial trajectory or seed while taking into account the energy loss and multiple-scattering between the tracker detector layers. It proceeds in three stages: seeding, finding and fitting.

During the seeding, initial trajectories (seeds) made of a pair of pixel hits that are compatible with the beam spot and have a lower  $p_T$  limit are used as possible candidates of the charge tracks. Pixel hits are the best track seeds while in the more forward region of the tracker detector,  $2 < |\eta| < 2.5$ , silicon pixel and inner strips hits are used for better track seeding.

The track finding stage uses a *Kalman Filter* pattern recognition approach (since the tracks can be described as a discrete dynamic *track state*, characterized by some given set of parameters and uncertainties, which is recursively updated one hit at a time on each layer) where, starting with the track parameters determined by the seeds, the track trajectory is extrapolated to outer neighboring tracker layers and compatible hits are assigned to the track.

In the fitting stage, the Kalman Filter algorithm (because the position information of the hit is updated to estimate the track parameters and uncertainties and the fitting process is repetitive) is again applied where each candidate track is fitted using least-squares fitting in two stages. The first stage avoids possible bias on the track parameters from the initial trajectories used in the seeding stage while the next stage yields the best estimates of the track parameters and uncertainties at the original vertex.

Other algorithms like the *iterative tracking algorithm* which is a general purpose tracking algorithm is used in association with customized CTF tracking algorithm to reconstruct the tracks of non-collisions events like cosmic and beam halo.

Similar to track reconstruction, vertex reconstruction involves two stages: vertex finding and vertex fitting. During vertex finding, a set of valid tracks from track reconstruction, represented by a list of track parameter vectors, is fed into a vertex finding algorithm which classifies the tracks into vertex candidates. The type of vertex finding algorithm used depends on whether it is finding a primary vertex (vertex where the particles are produced from the collision of the two proton beams) or secondary vertex (vertex where the particles are produced from the decay of an unstable particle) or the reconstruction of an exclusive particle decay.

The classified vertex candidates from vertex finding are fed into the vertex fitting algorithm. The output of the vertex fitting is a list of vertices, with each vertex having an estimated vertex position and a set of updated track parameter vectors. In vertex fitting, the best estimates of the vertex parameter, co-variance matrix, track parameter and the fit quality (chi-square, number of degrees of freedom, track weights) are used in distinguishing among a given set of tracks and their vertices.

## 5.4 Photon and Electron Reconstruction

Photons are reconstructed using superclusters and since they are neutral and do not leave tracks in the tracker, they are identified as superclusters in ECAL not associated to any tracks or reconstructed hits in the pixel tracker. The photon identification, beyond simply using the ECAL supercluster, is improved through several selection requirements using information from the tracker, ECAL, HCAL and the ratio of the photon candidate's energy deposited in HCAL to ECAL. Photons are supposed to deposit very little or no energy in HCAL and this is one of the main selection requirements to help distinguish photons from hadronic jets with high electromagnetic energy fraction which can easily be misidentified as photons.

For electron reconstruction, electron candidates are found when a supercluster is associated to a track reconstructed in the silicon tracker detector and in particular, its inner most layers (pixel hits). Electron reconstruction begins with a seeding approach which is either driven by ECAL or by the tracker. The ECAL driven seeding approach is very efficient for electrons with  $p_T > 10 \text{ GeV}/c$ . The track driven seeding approach uses a boosted decision tree to perform a pre-selection of the tracker clusters, in order to reduce

fake electrons which are light hadrons with many hits in the tracker. Low- $p_T$  electrons and non-isolated electrons (electrons embedded in jets) are reconstructed efficiently using the tracker driven seeded approach, since most of their energy is deposited in the tracker and very little in the ECAL, as they lose most of their energy through multiple scattering before they reach ECAL. When fitting the electron tracks, we must account for the different energy loss mechanisms of the electron compared to other charged particles. Since electrons lose most of their energy by radiating photons (*bremsstrahlung*, which is non-Gaussian in nature, the *Gaussian Sum Filter* algorithm (combination of several Gaussians) is used to provide good estimate of the track momentum both at the ECAL surface and at the interaction point.

## 5.5 Muon Reconstruction

Muon tracks are reconstructed using the all-silicon inner tracker (tracker tracks) and the muon system (standalone tracks). The standalone tracks are reconstructed using reconstructed positions (hits) in the muon system consisting of the Drift Tubes (DT) in the barrel ( $|\eta| < 0.9$ ), Cathode Strip Chambers (CSC) in the endcaps ( $1.2 < |\eta| < 2.4$ ) and Resistive Plate Chambers (RPC) in the overlap region ( $0.9 < |\eta| < 1.2$ ). There are two independent muon reconstruction approaches: *Global muon reconstruction (Outside-in)* and *Tracker muon reconstruction (Inside-out)*. For Global muon reconstruction, each standalone-muon track is matched to a tracker track by comparing the parameters of the two tracks propagated to a common surface. The global muon track is fitted combining hits from the tracker track and standalone-muon track using the Kalman-filter algorithm. For the tracker muon reconstruction, all tracks with  $p_T > 0.5 \text{ GeV}/c$  and total momentum  $p > 2.5 \text{ GeV}/c$  are considered as possible muon candidates and are extrapolated to the muon system taking into consideration the magnetic fields, the average expected energy loss in the calorimeters and multiple Coulomb scattering in the detector material to locally reconstruct segments in the muon system. A combination of different muon algorithms depending on the muon  $p_T$ , provides a robust and efficient muon identification.

Using the beam spot as constraint for the muon's vertex, we can distinguish between muons produced from  $pp$  collisions from *cosmic muons* and *beam halo muons* (muons

produced from the interaction of the proton beam with the gas in the beam pipe). Figure 5.2 show an illustration of the trajectories of different muon sources interacting with the CMS detector.

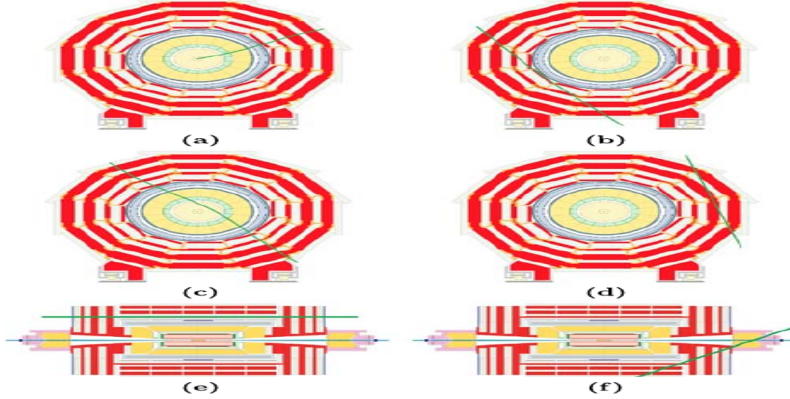


Figure 5.2: Illustration of muons from proton-proton collision, cosmic rays and beam halo. (a) Muons from collision propagating from the center and moving outwards, (b) Cosmic muons traveling through the detector leaving signals in opposite hemispheres of the muon system, (c) Cosmic muons leaving signals in the tracker and opposite hemispheres, (d) cosmic muons entering and leaving the detector without passing through the muon detector layers, (e) beam halo muons penetrating the detector and leaving signals in the endcaps and (f) Cosmic muons entering the detector through the endcap (EE) and leaving through the barrel (EB). This can happen in the reverse way; EB to EE.

## 5.6 Particle Flow Algorithm

The *Particle Flow* (PF) algorithm is an algorithm for reconstructing particles using detector information from the tracker, ECAL, HCAL and muon chambers of the CMS detector [52, 53]. It uses a combination of different algorithms comprising of calorimeter clustering, tracking and extrapolation to calorimeters, muon identification, electron pre-identification and linking local reconstructed elements, for reconstructing a list of particles which include photons, charge hadrons, neutral hadrons, muons and electrons. The same list of particles is subsequently used to reconstruct composite “particles” like jets,  $E_T^{\text{miss}}$  and taus. The versatility of the PF algorithm is the reason why it was introduced for reconstructing Jets and missing transverse energy ( $E_T^{\text{miss}}$ ), where complete information of the event content from every subdetector is needed for best performance.

The PF algorithm uses tracks, electron energy seeds, 4-momentum, super cluster energy calibration, bremsstrahlung tracks for electron and photon reconstruction making it extremely efficient at minimizing electron and photon misidentification. For  $E_T^{\text{miss}}$  reconstruction where full reconstruction of all the particles belonging to an event is necessary, the PF algorithm is very reliable.

## 5.7 Jet Reconstruction

A jet is a spray of particles arising from the hadronization of colored particles. Because jets are made of many particles like hadrons and photons from  $\pi^0$  decay, they are best reconstructed using the particle flow algorithm. Jets reconstructed using the PF algorithm are called *PF-Jets*.

Using calorimeter towers as input, jets can be reconstructed using the Anti- $k_T$  clustering algorithm which combines four vectors according to their relative transverse momentum ( $p_T$ ) within a standard cone size of  $\Delta R = 0.5$  in the  $(\eta, \phi)$  plane, where,  $\Delta R = \sqrt{\Delta\eta^2 + \Delta\phi^2}$ .

The quality of a reconstructed jet depends on a set of selection variables collectively referred to as the *JetID*. The JetID consist of variables which selects on jets candidate base on the composition of the jets. The jet composition can be described using the following quantities: electromagnetic energy fraction (EMF), the charge hadron fraction (CHF), the neutral hadron fraction (NHF), the charge electromagnetic fraction (CEF), neutral electromagnetic fraction (NEF) the number of calorimeter cells containing more than 90% of jet energy ( $N_{jet}^{90}$ ), the fraction of jet energy in the hottest Hybrid photodetector (HPD) unit in HCAL readout within a jet ( $f_{HPD}$ ) and the  $\eta$  region of the jet. The selection threshold and combination of jetID variables used will depend on a specific analysis and the type of jets involved. In general, jet candidates are required to have an electromagnetic energy fraction (EMF) more than 10% i.e.  $EMF > 0.01$ , must be within the ECAL fiducial region of  $|\eta| < 2.6$ , the number of calorimeter cells containing more than 90% of jet energy ( $N_{jet}^{90}$ ) must be  $> 1$ , the fraction of jet energy in the hottest Hybrid photodetector (HPD) unit in HCAL readout within a jet ( $f_{HPD}$ ) must be  $> 0.98$ , the charge hadron fraction (CHF)  $> 0.0$  if within  $|\eta| < 2.4$ , the neutral hadron fraction (NHF)  $< 1.0$ , the charge electromagnetic fraction (CEF)  $< 1.0$ , and

neutral electromagnetic fraction ( $NEF$ )  $< 1.0$ . These jetID selection requirements have been shown to remove mis-reconstructed jets arising from spurious energy deposition in subdetectors with good efficiency [54].

The jet energy is often mis-measured due to non-linear responses in the calorimeters as the hadronic shower develops, cracks in the detector and additional energy from events with PU. The jet energy is corrected for contributions from the above sources through *Jet Energy Corrections* (JEC) measurements [55]. Applying these corrections during reconstruction guarantee a reliable measurement of the jet energy , however, JEC is one of the sources of uncertainties in most analysis which involve jets.

## 5.8 Missing Transverse Energy Reconstruction

Missing Transverse Energy is defined as the negative vector sum of the transverse energy deposits of all the particle candidates in an event, including the JEC. Its magnitude,  $E_T^{\text{miss}}$  is given as

$$E_T^{\text{miss}} = \left| - \sum_n (E_n \sin \theta_n \cos \theta_n \hat{\mathbf{i}} + E_n \sin \theta_n \sin \theta_n \hat{\mathbf{j}}) \right| = |\not{E}_T^x \hat{\mathbf{i}} + \not{E}_T^y \hat{\mathbf{j}}| \quad (5.1)$$

Where,  $n$  is the sum over all calorimeter energy deposits including energy deposits in towers, reconstructed energies (hits) or generator level particle energies.  $E_T^{\text{miss}}$  is used to infer the presence of a particle which escaped the CMS detector like neutrinos ( $\nu$ ), neutralinos ( $\tilde{\chi}_1^0$ ) and gravitino ( $\tilde{G}$ ).

In order to measure  $E_T^{\text{miss}}$  accurately, a particle detector should be nearly hemispherical i.e. have a  $4\pi$  solid angle coverage, to allow for complete measurement of the transverse momentum of all the particles belonging to an event. The hadronic forward (HF) subdetector of the CMS detector, with little space allowing for the passage of the proton beams, provide this near  $4\pi$  solid angle.

Measuring  $E_T^{\text{miss}}$  is always challenging and is a source of uncertainty in most analysis which involve  $E_T^{\text{miss}}$  as machine induced background processes, mis-measured energy of and from mis-reconstructed particles and anomalous signals like spike can contribute to the measurement of  $E_T^{\text{miss}}$ . By minimizing the contributions from these processes we can measure  $E_T^{\text{miss}}$  better [56, 57].

The use of  $E_T^{\text{miss}}$  in event selection is common in most analysis which involves the search for new phenomena which is a common prediction in models Beyond Standard Model (BSM) like *supersymmetry*. The presence of large  $E_T^{\text{miss}}$  in an event indicates the presence of a new particle not described by standard model interactions which usually have small  $E_T^{\text{miss}}$  as in the case of the neutrino in the W boson decay,  $W \rightarrow e + \bar{\nu}$ .

## 5.9 Anomalous Signals

Sometimes anomalously large signals called “*spikes*” are produced when neutrons or charged hadrons like protons strike directly, ionizing the silicon of the photodiode producing an electronic signal even in the absence of any crystal scintillation.

Because spike signals are not produced through the crystal scintillation process, which takes about 10 ns, their measured arrival time is early and negative. Energy deposits from spikes range from a few GeV to the saturation energy of ECAL which is about 1.7 TeV. Since they are not due to showering particles, most often only one isolated crystal sees such energy. Spikes may occasionally have positive time, appearing late or delayed in their arrival time at ECAL, and populating the tails of the photon’s rechit time distribution. The late arrival time may be due to the slow propagation (takes an indirect route) of neutrons through the CMS detector.

Numerous test beam, collision data and simulation studies [58, 59], have been carried out towards understanding the properties of events with spikes and how they can be tagged and removed. These studies reveal that most spikes can be identified using a topological energy sharing variable called “*Swiss-Cross*” (SX) constructed as  $1 - \frac{E_4}{E_1}$ .  $E_1$  is the energy deposit of the central (highest energy) crystal and  $E_4$  is the sum total of the energy of the neighboring four crystals in the  $(\eta, \phi)$  plane. A selection cut  $\text{SX} > 0.95$  rejects more than 99% of isolated spikes with transverse energy greater than 10 GeV with very little impact on the efficiency of selecting electromagnetic (EM) showers. Other topological energy sharing variables like  $1 - \frac{E_6}{E_2}$  and  $1 - \frac{E_9}{E_2}$ , where  $E_2$  is the sum of the energy of two crystals sharing the energy deposited from simultaneous spikes and  $E_6(E_9)$  is the sum of the neighboring 6(pairs-of)(9) crystals in the  $(\eta, \phi)$  plane. The  $1 - \frac{E_6}{E_2}$  variable is used to identify isolated spikes whose energy deposit spread in two adjacent crystals while the  $1 - \frac{E_2}{E_9}$  is used to identify non-isolated spikes i.e. spikes which

are found embedded in a supercluster.

It has also been shown that applying selection cuts on the rechit time of  $\pm 3$  ns leads to more than 90% efficiency for rejecting spikes. However, in this thesis, we do not require such selection cuts on the rechit time as these rechits include rechits of possible delayed electromagnetic particles produced during  $pp$  collisions with arrival time beyond 3 ns.

## Chapter 6

# Search for Long-Lived Neutral Particles

### 6.1 Analysis Strategy

A search for events with at least a single late arrival time photon at the Electromagnetic Calorimeter (ECAL) and large missing transverse energy ( $E_T^{\text{miss}}$ ) is described. The search uses a counting method, in which an excess number of events with photon time above a timing threshold to the expected number of background events, hint at the presence of a new physics phenomena. Such a phenomena is expressed through the decay of a Long-Lived Neutral Particle (LLNP) into a late photon and large  $E_T^{\text{miss}}$ , which is not common with standard model interactions. We expect most of the background events to arise from non-collision rather than proton-proton ( $pp$ ) collision events.

#### 6.1.1 Signal and Background Events

The late photon ( $\gamma$ ) and large missing transverse momentum ( $E_T^{\text{miss}}$ ) are from the decay of the lightest neutralino ( $\tilde{\chi}_1^0$ ), i.e.  $\tilde{\chi}_1^0 \rightarrow \gamma + \tilde{G}$ , which serves as the LLNP. Because the  $\tilde{\chi}_1^0$  is produced indirectly through the cascade decay of heavier supersymmetric particles like gluino ( $\tilde{g}$ ) or squark ( $\tilde{q}$ ), i.e.  $gg \rightarrow \tilde{g}\tilde{g} \rightarrow q\bar{q}q\bar{q}\tilde{\chi}_1^0\tilde{\chi}_1^0$  or  $q\bar{q} \rightarrow \tilde{q}\bar{\tilde{q}} \rightarrow \bar{q}q\tilde{\chi}_1^0\tilde{\chi}_1^0$ , in addition to the late photon and large  $E_T^{\text{miss}}$ , the signal event topology includes multiple high- $p_T$  jets. The large  $E_T^{\text{miss}}$  is due to the undetected gravitino ( $\tilde{G}$ ) at the CMS

detector. We, thus expect a typical signal event to comprise of at least one late high- $p_T$  photon, large  $E_T^{\text{miss}}$  and multiple high- $p_T$  jets. Such an event composition is not expected of standard model events. The multiple high- $p_T$  jets also provide an added handle in the event selection to help suppress background events with no jets.

Our background events are events from either  $pp$  collisions or non-collisions which mimic the late photon, large  $E_T^{\text{miss}}$  and multiple jets signal.

The non-collision background events include the so-called *Beam Induced Backgrounds* or beam halo, cosmic rays and spikes. Most of these events have a late high- $p_T$  photon and large  $E_T^{\text{miss}}$ .

Collision background events can mimic the  $\tilde{\chi}_1^0$  decay signal producing late photons and large  $E_T^{\text{miss}}$  in cases where the photon time and/or  $E_T^{\text{miss}}$  are mis-measured. Other collision events might have real  $E_T^{\text{miss}}$  and a misidentified photon object. For example, inclusive Z+jets/W+jets events, inclusive top-anti-top ( $t\bar{t}$ )+jets events and inclusive ZZ/WW/WZ+jets events can have true  $E_T^{\text{miss}}$  through the  $Z \rightarrow \nu\bar{\nu}$  and  $W \rightarrow e\bar{\nu}_e$  decays, where the undetected neutrino ( $\nu$ ) give rise to  $E_T^{\text{miss}}$ . Multijets and QCD events, on the other hand, give rise to fake  $E_T^{\text{miss}}$  (instrumental  $E_T^{\text{miss}}$ ), where there is no undetected particle pertaining to the event but rather  $E_T^{\text{miss}}$  arising because of poor reconstruction of the energy of particles. The late photon arises when one of the jets or an electron is misidentified as a photon and it's ECAL time is mis-measured. The other jets in the event satisfy the high- $p_T$  multiple jets requirement.

### 6.1.2 Samples

#### Datasets

The data sample we use for this search contain events passing the HLT trigger with at least one photon. These events were produced during LHC Run 1 in 2012 of  $pp$  collisions at the center of mass energy,  $\sqrt{S} = 8$  TeV. The data is equivalent to a total integrated luminosity of  $19.1 \text{ fb}^{-1}$  recorded by the CMS detector.

#### Monte Carlo Samples

The MC samples were produced with *Summer 2012* prescription of the calibration and alignment status of the CMS detector and pile up conditions at 8 TeV.

The GMSB SPS8 signal samples have 50,000 events for each mean lifetime ( $c\tau$ ) and effective SUSY breaking scale ( $\Lambda$ ) or mass of  $\tilde{\chi}_1^0$  ( $m_{\tilde{\chi}_1^0}$ ). These samples are produced for different  $c\tau$  ranging from 50 cm to 1000 cm for each  $\Lambda$  or  $m_{\tilde{\chi}_1^0}$  point. We vary  $\Lambda$  from 100 TeV to 220 TeV which is equivalent to  $m_{\tilde{\chi}_1^0}$  ranging from  $139 \text{ GeV}/c^2$  to  $314 \text{ GeV}/c^2$ . Table 6.1 shows a summary of our signal MC samples used in this analysis. For each sample, the number of events, cross-section and branching ratio for  $\tilde{\chi}_1^0$  production and decay to  $\gamma$  and  $\tilde{G}$  for each SUSY breaking scale is also given.

The  $\gamma$ +jet MC samples were generated for different momentum of the photon with respect to the colliding partons and normalized to the  $19.1 \text{ fb}^{-1}$  of integrated luminosity. The cross-sections,  $p_T$  of the photon ( $\hat{p}_T$ ) radiated by the colliding parton and the number of events in each sample is summarized in Table 6.2. The  $\hat{p}_T$  range is from  $50 \text{ GeV}/c$  to  $800 \text{ GeV}/c$ .

$\Lambda$ [TeV]	$c\tau$ (mm)	$\sigma_{LO}$ (pb)	Number of Events	Branching Ratio
100	500-10,000	0.368	50,000	0.9444
120	500-10,000	0.133	50,000	0.9042
140	500-10,000	0.0574	50,000	0.8711
160	500-10,000	0.0277	50,000	0.8464
180	500-10,000	0.0145	50,000	0.8282
220	500-10,000	0.0044	50,000	0.8282

Table 6.1: Signal GMSB SPS8 Monte Carlo samples for different  $\Lambda$  with  $50 \text{ cm} < c\tau < 1000 \text{ cm}$  and Branching Ratios (BR).

$\hat{p}_T$	$\sigma_{LO}$ (pb)	Number of Events
$50 \sim 80$	3322.3	1995062
$80 \sim 120$	558.3	1992627
$120 \sim 170$	108.0	2000043
$170 \sim 300$	30.1	2000069
$300 \sim 470$	2.1	2000130
$470 \sim 800$	0.212	1975231

Table 6.2: The  $\gamma$ + jets samples for  $\hat{p}_T$  from  $50 \text{ GeV}/c$  to  $800 \text{ GeV}/c$

## 6.2 ECAL Timing

In this section, we describe how the photon arrival time is measured and the adjustments we made on the MC time so that it captures the same conditions as data. We discuss the ghost/satellite proton bunches and argue that they are a possible background source to late photons.

### 6.2.1 Photon Time Measurement

The electromagnetic shower of a photon spreads across several crystals, and as a result, the photon's energy and time measurements are read from several crystals belonging to the photon's supercluster, which contains all of its energy. The presence of anomalous signals from spikes, noisy crystals and pile-up events, demand a robust method for measuring the photon arrival time at ECAL, and since the photon's ECAL time is our main observable for distinguishing background from signal events, we employ a method, which is capable of reducing timing bias that could arise from such anomalous signals, for measuring the photon's arrival time.

Using the photon's supercluster, the photon's arrival time at ECAL can be defined using either the reconstructed time ( $t_{reco}$ ) of a single crystal which is the *seed crystal* (crystal with the highest energy deposit), or a weighted average time calculated using the reconstructed time and its uncertainty, of each crystal of the photon's supercluster. We write,  $t_{seed}$ , for the seed time and,  $t_{Ave}$ , for the average time defined as

$$t_{Ave} = \frac{\sum_{i=1}^N \frac{t_{reco}^i}{\sigma_i^2}}{\sum_{i=1}^N \frac{1}{\sigma_i^2}}, \quad (6.1)$$

where,  $N$  is the total number of crystals of the supercluster,  $t_{reco,i}$  and  $\sigma_i$  are the time and uncertainty on the reconstructed time of each crystal, respectively. Figure 6.1 shows a comparison of the seed time,  $t_{seed}$ , and the average time,  $t_{Ave}$ , to be the photon ECAL time. Both distributions are normalized to total number of events.

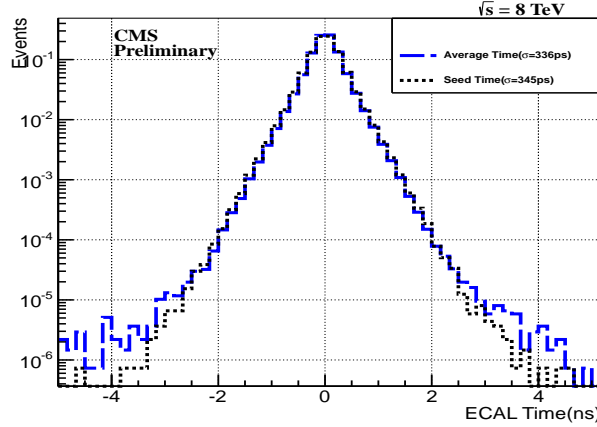


Figure 6.1: Seed (black) and Average (blue) times as the measured photon time.

The width ( $\sigma$ ) of both Gaussian distributions are similar. We observed  $\sigma = 345$  ps for the seed time compared to  $\sigma = 336$  ps for the average time. The average time is susceptible to timing bias. For example, if one or more of the crystals in the supercluster is poorly time calibrated or embedded with a spike, the photon time, because of the spike or mismeasured time from a single crystal, can be very biased.

In this analysis, we use the seed time for the photon's arrival time in ECAL and also use the  $\chi^2$  computed using the average time to identify photons with anomalous signals like spikes.

The  $\chi^2$  on the average time is computed as

$$\chi^2 = \sum_{i=0}^N \frac{(t_{reco}^i - t_{Ave})^2}{\sigma_i^2} \quad (6.2)$$

where,  $N$  is the number of crystals in the photon supercluster,  $t_{reco}^i$  and  $\sigma_i$ , are the time and uncertainty for each crystal, and  $t_{Ave}$ , is the mean time defined in Equation 6.1. The  $\chi^2$  can be used to distinguish spikes from true photons. A distribution of the normalized  $\chi^2$  against the photon ECAL time is shown in Figure 6.2. Spikes misidentified as photons have large values of  $\chi^2$  and usually have large negative ECAL time.

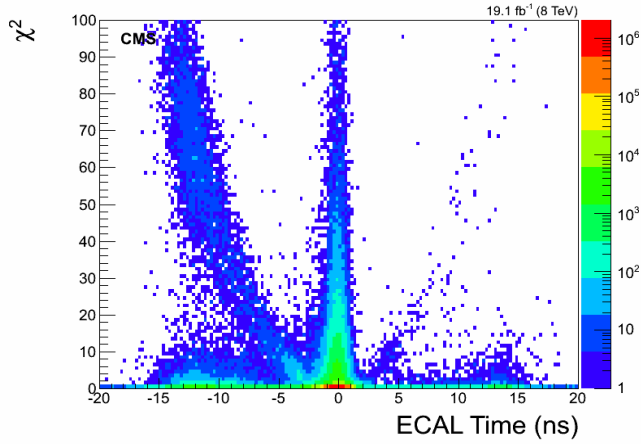


Figure 6.2: The  $\chi^2$  Vs photon ECAL time plot showing spikes misidentified as photons have very large  $\chi^2$  and negative ECAL time. The region of  $\chi^2 > 4$  is mostly dominated by spikes events.

From the  $\chi^2$  Vs ECAL time plot (Figure 6.2), we observe that, most of the true photons have ECAL time around zero, but, there are many photons with large ECAL time which equally have large normalized  $\chi^2$  values. We expect large  $\chi^2$  values in cases where the time measurements from non-seeded crystals is inconsistent with the time measurement from the seed crystal. We also observe that, a cut in  $\chi^2 < 4$ , can reduce with 99.2% efficiency, photon contributions from spikes (where a neutron, embedded in a jet, hits directly the photo-detectors and produces a spike) and photons with mis-measured ECAL time.

### Monte Carlo Time

It is challenging to properly simulate ECAL time for MC events so that it captures the conditions of the ECAL detector during data recording. As a result, the mean time and root mean squared (RMS) from MC events does not agree with those in data. We account for this disagreement by shifting the mean time and smearing the RMS, by an additional Gaussian convolution, on the photon time of MC events so that it matches the mean time and RMS of data. The amount of shifting and smearing required is obtained using selected 1 or 2 jets events. To ensure that true photon events are used, we select 1 or 2 jets events with in-time photons,  $|t_\gamma| < 2$  ns, with photon  $p_T > 80$  GeV, for both data and MC  $\gamma+jets$  samples. Shown in Figure 6.3, is the in-time photon

time distributions for data and MC  $\gamma$ +jets samples before (left plot) and after (right plot) the mean time shifting and RMS smearing were done on the photon time of MC  $\gamma$ +jets events. We see good agreement in MC and data photon time after the mean time shifting and RMS smearing on the MC is done.

### 6.2.2 Satellite Bunches

Ghost/Satellite proton bunches trail the main proton bunch at the LHC with a time spacing of 2.5 ns. These ghost/satellite bunches are the source of Beam halo-induced photons produced observed in ECAL. Figure 6.4 shows the photon time for photons with  $p_T > 50 \text{ GeV}/c$  in ECAL. The 2.5 ns discrete pattern in the photon ECAL time confirm the presence of ghost/satellite beam halo-induce photons. Because of the beam intensity, most of these out-of-time photons are in the endcap ( $1.47 < \eta < 3.0$ ) with a few in the barrel ( $|\eta| < 1.47$ ). We consider halo-induced photons a major background to late photons.

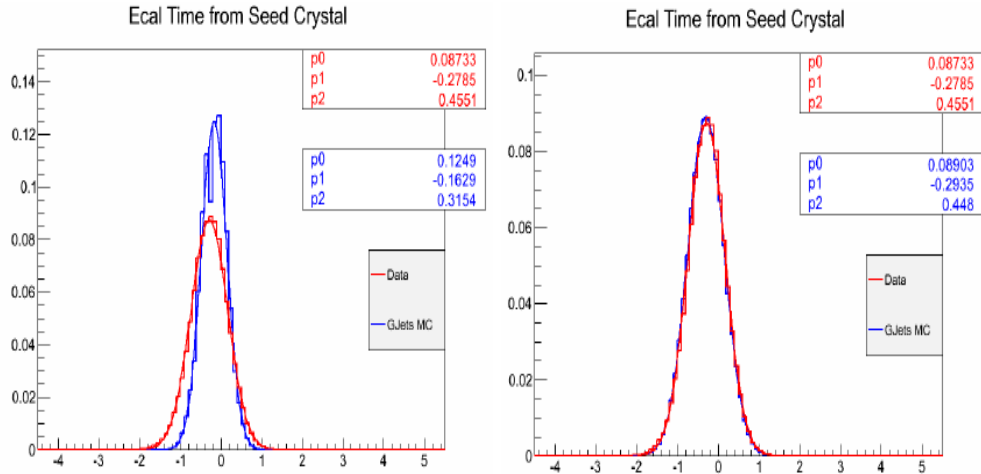


Figure 6.3: ECAL time distributions of in-time photons from MC  $\gamma$ + jets (blue) and data (red) samples before (left) and after (right) we adjusted the photon time from MC.

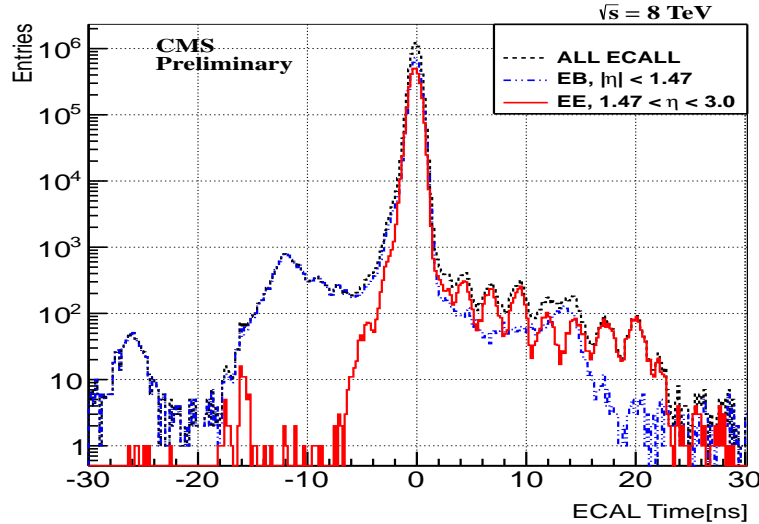


Figure 6.4: ECAL timing distribution of photons in barrel (EB), endcap (EE) and all of ECAL (ALL ECAL) with  $p_T > 50$  GeV from data. A 2.5 ns delay timing structure is observed in endcaps.

### 6.2.3 $E_T^{\text{miss}}$ Adjustments

In the formation of energy clusters, which are used for event reconstruction by the particle flow (PF) algorithm, “out-of-time” energy deposits in ECAL are excluded. The reason is because, the PF algorithm avoids energy deposits from particles which are not produced from the main proton-proton bunch collisions, like cosmic muons and machine-induced backgrounds, as these are normally out-of-time. Because of the exclusion, the out-of-time photon’s transverse energy,  $E_T$ , is not included in the calculation of missing transverse energy or  $\cancel{E}_T$  (from now on, we will be using for convenience,  $\cancel{E}_T$  instead of  $E_T^{\text{miss}}$  as the symbol for missing transverse energy) of the event. This exclusion introduces some differences in the calculation of  $\cancel{E}_T$  for in-time ( $|t_\gamma| < 3.0$  ns) and for out-of-time photon events.

Since the energy deposits from events with out-of-time photons could be from a possible signal event, and we are searching for events with late arrival time photons, we correct for the  $E_T$  exclusion, by adding back the out-of-time photon’s  $E_T$  vector to the particle flow reconstructed  $\cancel{E}_T$  (PF-MET) vector, for events with out-of-time photons. We avoid

any bias in our event selection, particularly for events with out-of-time photons, by introducing an additional missing transverse energy variable defined as  $\vec{E}_T^{\gamma} = \vec{E}_T + \vec{E}_T$ , which we use in our final event selection.

### 6.3 Event Selection

Our event selection happens in two stages. The first stage, consisting of L1 trigger at online and an HLT software trigger of multiple selection modules, selects only triggered single photon events. The second stage happens offline, where, our signal-like event selection requirements are applied.

The offline event selection criteria is designed to select signal-like events whose event topology comprise of at least a single photon, multiple jets and large  $\cancel{E}_T$ . The multiple jets arise from the cascade decay of gluino or squark to other quarks or gluons, in addition to the lightest neutralino. We require multiple jets in our event selection as part of the signal event topology, but, also as a way of suppressing non-collision background events like cosmic and beam halo muons, which are usually not associated with jets. Collision background events like multijets and QCD events, where a jet can be misidentified as a photon, are equally suppressed by selecting purely hadronic jets i.e. jets containing a greater portion of hadronic energy fraction from pions and kaons.

The single late photon and large  $\cancel{E}_T$  is from  $\tilde{\chi}_1^0 \rightarrow \gamma + \tilde{G}$  decay and we select only photons in the barrel ( $|\eta_\gamma| < 1.479$ ) with high transverse momentum. This suppresses out-of-time photons from the so-called halo-induced photons produced by ghost/satellite proton bunches. The high- $p_T$  photon requirement also helps suppress out-of-time photons due to timing mismeasurements of photons from QCD and multiple jets events.

The large  $\cancel{E}_T$  requirement is useful for suppressing  $\gamma+$ jets and QCD events with apparent  $\cancel{E}_T$  or *fake*  $\cancel{E}_T$  which arise from energy misreconstruction and cracks in the detector. Out-of-time photon contribution from spikes is also reduced by applying electromagnetic shower shape selection on  $S_{Minor}$  at the HLT trigger level.

#### 6.3.1 Trigger Selection

During the online event selection, only events passing our online higher level trigger (HLT): `HLT_DisplacedPhoton65_CaloIdVL_IsoL_PFMET25`, which is seeded by a L1

trigger: `HLT_L1SingleEG12`, are accepted. The HLT trigger is a combination of selection modules triggering events with at least one calorimeter identification standards of a very loose isolated photon with  $p_T$  of atleast  $65\text{ GeV}/c$  and  $\cancel{E}_T$  (without any out-of-time energy deposit bias) above  $25\text{ GeV}$ . The minor axis of the photon electromagnetic shower must not spread across many crystals in any direction. This is implemented as  $0.1 < S_{Minor} < 0.4$  of the photon.

We study the HLT trigger efficiency and turn-on (efficiency becomes nearly 100%) curve separately for the photon  $p_T$  and event  $\cancel{E}_T$ , using, as the denominator of the event ratio events with at least one jet and a photon also triggered by the HLT trigger: `HLT_Photon50_CaloIdVL_IsoL`. This trigger selects events with photon candidates also satisfying the calorimeter identification standards of a very loose isolated photon with  $p_T$  of at least  $50\text{ GeV}/c$ . The HLT event selection efficiency in  $p_T$  is defined as the fraction of events passing our HLT trigger to events with at least one jet and a photon triggered by the `HLT_Photon50_CaloIdVL_IsoL` trigger within  $\Delta R < 0.5$ , while the efficiency in  $\cancel{E}_T$  is defined as the ratio of events passing our HLT trigger (`HLT_DisplacedPhoton65_CaloIdVL_IsoL_PFMET25`) over events with at least one jet and a photon passing the `HLT_Photon50_CaloIdVL_IsoL` trigger, with no  $\cancel{E}_T$  selection cut applied. Photons selected by both triggers must also satisfy the loose selection cuts, excluding the photon  $p_T$  and  $\cancel{E}_T$  selection cuts, of our offline photon selection requirement summarized in Table 6.3.

The results of the trigger efficiency measurements in photon  $p_T$  and event  $\cancel{E}_T$  shown in Figure 6.5, indicate that the event selection efficiency is 100% for events with photon  $p_T > 80\text{ GeV}/c$  and  $\cancel{E}_T > 60\text{ GeV}$ . The slight difference between the  $\gamma+\text{jets}$  (black) and the GMSB (red) MC samples is because the events in  $\gamma+\text{jets}$  samples have no real  $\cancel{E}_T$ , and it is difficult to simulate apparent or fake ( $\cancel{E}_T$  from detector crack and unclustered energy deposits)  $\cancel{E}_T$  in MC simulation.

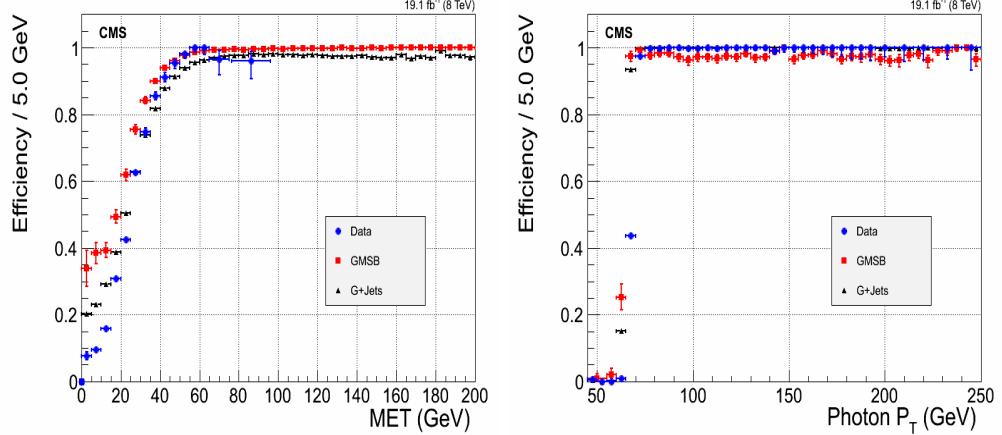


Figure 6.5: Our HLT trigger efficiency turn-on curves in event  $\cancel{E}_T$  (left) and photon  $p_T$  (right). The  $\gamma + \text{jets}$  samples require photon  $p_T > 170$  GeV/c.

### 6.3.2 Offline Selection

Our offline event selection, applied on the HLT triggered single photon events, require that the leading photon have  $p_T > 80$  GeV/c and if the event has more than one photon, the sub-leading photon have  $p_T > 45$  GeV/c. Electromagnetic showers initiated by charged hadrons are rejected by requiring  $E^{\text{HCAL}}/E^\gamma < 0.05$ , where  $E^{\text{HCAL}}$ , is the sum of the energy in the HCAL towers directly behind the ECAL photon supercluster within a  $\Delta R < 0.15$ , with  $\Delta R = \sqrt{(\eta - \eta^\gamma)^2 + (\phi - \phi^\gamma)^2}$ , and  $E^\gamma$  is the photon energy in ECAL.

Electrons are rejected by requiring the absence of hits in the first two layers of the pixel detector that is consistent with an electron track matching the observed location and energy of the photon candidate (this is known as pixel veto requirement).

The photon candidates must satisfy three *isolation* requirements that reject photons produced in hadronic decays: (1)  $Iso_{\text{TRK}} < 0.2$  GeV, where  $Iso_{\text{TRK}}$ , is the sum of the  $p_T$  of tracks compatible with the primary event vertex in an annulus  $0.015 < \Delta R < 0.40$ , excluding a strip half  $\eta$  width of 0.015 and the additional inner cone of size 0.04, optimized to exclude reconstructed tracks from  $Z \rightarrow e^+e^-$  events, centered around the line of vertex pointing to the photon supercluster. The exclusion is to remove the photon's own energy if it converts into an  $e^+e^-$  pair; (2)  $Iso_{\text{ECAL}} < 4.5$  GeV, where  $Iso_{\text{ECAL}}$ , is the transverse energy deposited in ECAL in an annulus  $0.045 < \Delta R < 0.4$ , centered

around the photon ECAL supercluster, excluding the strip half  $\eta$  width of 0.02 and the additional inner cone of size 0.045 centered around the ECAL supercluster position; (3)  $I_{\text{soHCAL}} < 4.0 \text{ GeV}$ , where  $I_{\text{soHCAL}}$  is the transverse energy of HCAL tower in an annulus of  $0.15 < \Delta R < 0.40$ , centered about the ECAL supercluster position. If the photon is very close to a track within a range in  $\Delta R(\gamma, \text{track}) < 0.6$ , it is rejected. This is to avoid misidentifying charge particles as photons and to prevent double counting jets with high electromagnetic energy component as photons. The photon must also be isolated from any other particle in a cone size of  $\Delta R(\gamma, \text{particle}) < 0.4$ . The size of the photon electromagnetic shower along the minor axis ( $S_{\text{Minor}}$ ) must be within 0.12 to suppress photons embedded in hadronic jets.

Only photons belonging to the barrel (EB) region i.e.  $|\eta_\gamma| < 1.479$ , are accepted, to avoid many out-of-time halo-induced photon candidates from ghost/satellite proton bunches, which belong to the endcap (EE) shown in Figure 6.4, and also since not many signal out-of-time photons go into the endcap.

Topological selection cuts,  $1 - E_6/E_2 < 0.98$  and  $1 - E_4/E_1 < 0.98$ , on the photon energy deposit, help suppress spikes which are caused by the direct interaction of the ECAL APDs by charged particles and neutrons producing anomalous photon signal. A summary of our full photon selection criteria is presented in Table 6.3.

For jets, we select jets with  $\eta_{\text{jet}} < 2.4$ , and require that the leading jet in the event has a  $p_T > 35 \text{ GeV}/c$  with the event having at least 1 jet. This helps suppress non-collision background events without jets. The jets are reconstructed using the PF algorithm and identified based on the identification selection criteria summarized in Table 6.4, where a jet candidate must satisfy the following: the Charge Electromagnetic Fraction (CHF) and the Neutral Electromagnetic Fraction (NEF) must make up a greater portion of the jet sub-structure ( $> 99\%$ ), the Neutral Energy Fraction (NEF) must smaller than 99%, in order that the jet is not easily misidentified as a photon. A jet near a photon object within a cone of 0.3 is rejected.

From our HLT trigger event selection efficiency plot in Missing Transverse Energy (MET) shown in Figure 6.5, and in order to suppress most of the background events with out-of-time photons, we observed that a missing transverse energy of at least  $60 \text{ GeV}$  for  $\cancel{E}_T$  and  $\cancel{E}_T^\gamma$  is enough to suppress  $\gamma + \text{jets}$  and QCD events with apparent missing transverse energy.

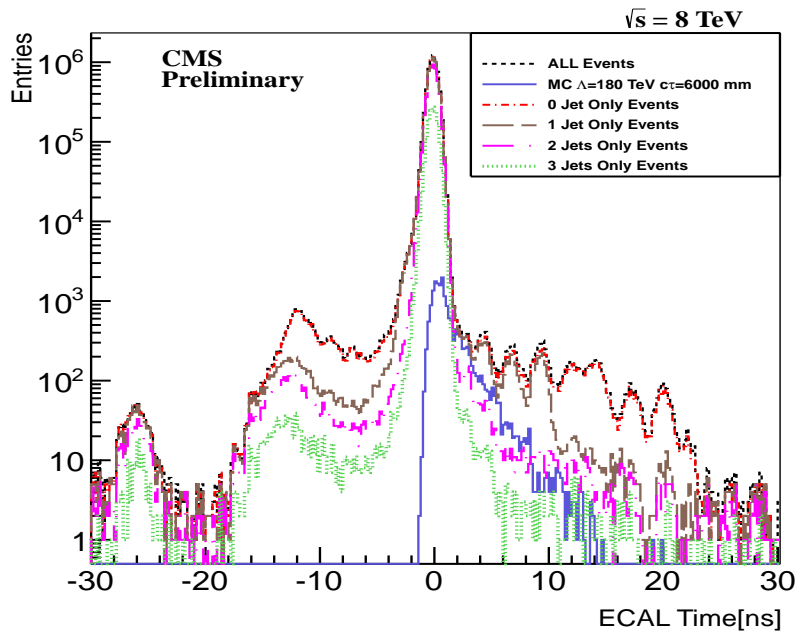


Figure 6.6: Comparing ECAL time distribution of events with different jet multiplicity from small sample of data and a single GMSB  $\Lambda = 180 \text{ TeV}$  and  $c\tau = 6000 \text{ mm}$  sample. Accepted photons must have  $p_T > 60 \text{ GeV}$  and belong to barrel and encaps.

---

**Photon Selection Criteria**


---

Criteria	Requirement
Event leading photon must have $p_T(\gamma^1)$	$> 80 \text{ GeV}$
Other photons in event must have $p_T(\gamma^{2,3,\dots})$	$> 45 \text{ GeV}$
$ \eta_\gamma , (\text{Barrel Only}),$	$< 3.0 (< 1.5)$
$S_{\text{Minor}}$	$0.12 \leq S_{\text{Minor}} \leq 0.38$
$E^{\text{HCAL}}/E^\gamma$	$< 0.05$
$\Delta R(\gamma, \text{track})$	$> 0.6$
$I_{\text{Iso}}^{\text{HCAL}}, I_{\text{Iso}}^{\text{ECAL}}, I_{\text{Iso}}^{\text{TRK}}$	$< 4.0 \text{ GeV}, < 4.5 \text{ GeV}, < 0.2 \text{ GeV}$
Photon Isolation cone size $\Delta R(\gamma, \text{particle})$	$< 0.4$
Topological Spike cuts	$1 - E_6/E_2 < 0.98, 1 - E_4/E_1 < 0.98$

---

Table 6.3: The photon identification and selection criteria used in this analysis

---

**Jet PF identification selection criteria**


---

Criteria	Requirement
Jet $p_T$	$> 35 \text{ GeV}$
Number of Jet constituents	$> 1$
Charge EM energy fraction (CEF)	$> 0.99$
Neutral Hadron energy fraction (NHF)	$< 0.99$
Neutral EM energy fraction (NEF)	$< 0.99$
If $ \eta $ of jet is $> 2.4$ , Charge Hadron energy fraction (CHF)	$> 0$
If $ \eta $ of jet is $> 2.4$ , Charge multiplicity (NCH)	$> 0$
$\Delta R(\gamma, \text{jet}) = \sqrt{(\phi_\gamma - \phi_{\text{jet}})^2 + (\eta_\gamma - \eta_{\text{jet}})^2}$	$> 0.3$
$\cancel{E}_T, \cancel{E}_T^\gamma$	$> 60 \text{ GeV}$

---

Table 6.4: The Jet ID and MET selection used in this analysis

In Figure 6.6, we observed that most of our background events with out-of-time beam halo-induced photons are mostly zero and one jet events. As a result, we use these zero and one jet events as a control sample only to study our background events, while our signal-like events are events with the following topology:  $\geq 1 \gamma + \geq 2 \text{ jets} + \cancel{E}_T > 60 \text{ GeV} + \cancel{E}_T^{\gamma} > 60 \text{ GeV}$ .

## 6.4 Background Estimation

Most of our background events with out-of-time photons are non-collision events produced from different sources. In order to qualify and quantify these different sources, we compare in-time ( $|t_\gamma| < 2 \text{ ns}$ ) photon candidates to out-of-time ( $t_\gamma < -3 \text{ ns}$  and  $t_\gamma > 3 \text{ ns}$ ) photon candidates. By also comparing photons from events with different number of jets, we were able to uncover the different background sources and better quantify the contribution from each source. In Figure 6.7, we present scatter plots of the photon’s ECAL time against  $\eta$  (left) and against  $\phi$  (right) for events with  $\cancel{E}_T > 25 \text{ GeV}$  and photon  $p_T > 60 \text{ GeV}$ , belonging to the barrel and endcap regions.

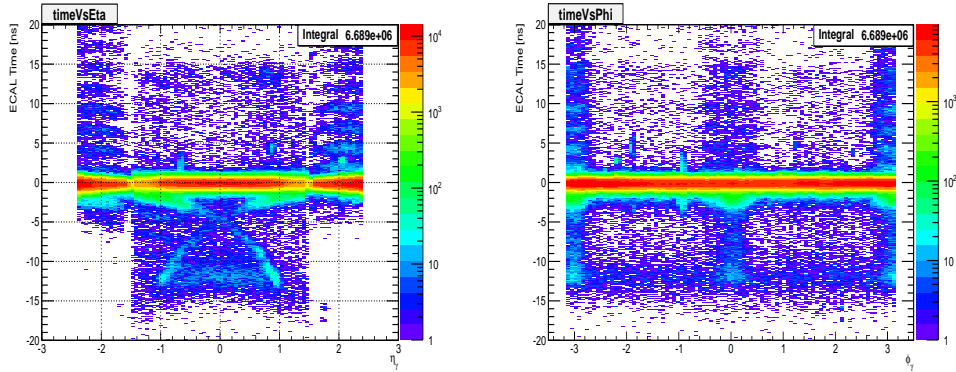


Figure 6.7: ECAL time against  $\eta$  (left) and ECAL time against  $\phi$  (right) for photons with  $p_T > 60 \text{ GeV}$  from data.

These scatter plots show that a good number of photons that are out-of-time belong to very different sources. For example, the “cross-like” feature seen on the left plot, is particular to photons with earlier time and in combination with the time-discrete

pattern, prominent in the endcaps ( $1.479 < \eta_\gamma < 3$ ) regions and the high concentration at  $\phi = 0 \pm \pi$  on the plot on the right, can be interpreted as photons produced by the same so-called proton beam halo. We argue the background out-of-time photon candidates can be split into 4 major categories: (1) Halo-induced photons from main and ghost/satellite beam halo muons, because they have early arrival times, creates the cross-like feature and time-discrete pattern and are also highly concentrated at  $\phi = 0, \pm\pi$ , (2) Cosmic-induced photons produced from cosmic muons, due to the random distribution of out-of-time photons throughout ECAL, (3) Spikes, due to the high concentration of photons with time of about -12.5 ns and Finally, (4) QCD or collision background events with photons with mis-measured ECAL time.

Since spikes are notoriously difficult to identify and eliminate, to reduce their contribution to out-of-time photons, we restrict our event selection to photons with time  $2.0 < t_\gamma < 13.0$  ns and  $-10.0 < t_\gamma < -3$  ns. This reduces our signal search window for events with late photon time to events with photon time between  $2.0 < t_\gamma < 13.0$  ns.

We split the background events into Collision and Non-Collision event categories and study each category separately. We first identify and reject photon candidates from beam halo, cosmic muons and spikes and then estimate the residual non-collision and collision background photon candidates using the **ABCD** background estimation technique.

#### 6.4.1 Collision Background

##### QCD Photons

Events from satellite/ghost proton bunches described in section 3.1.4, produce out-of-time photons which can be present in the barrel. We refer to the events from collisions with out-of-time photons, including QCD events with photons which have mis-measured time, as our *QCD background* events. It is challenging to define a strategy for rejecting this background events. Our approach, after rejecting non-collision events, is to estimate their contribution to signal using the ABCD background estimation method. We also perform a separate background estimation using a control sample of Z events, and show that, these events with out-of-time photons from collisions, are mostly QCD events with photon candidates with time mis-measurements.

### 6.4.2 Non-Collision Background

#### Halo-induced Photons

Protons in the main and sometimes ghost/satellite bunches can, through inelastic scattering with residual gas molecules like H<sub>2</sub> and CO<sub>2</sub> in beam pipe, produce pions which later decay into muons traveling with energy of a few TeV, called *Beam Halo* muons. These energetic muons radiate energetic photons, called *Halo-induced photons*, in the calorimeter through a process called *bremsstrahlung*. Some of the beam halo muons are produced when protons scatter off Tertiary Collimators (TCT), 50 m <  $z$  < 148 m, away from the center of the CMS detector. These halo muons can travel nearly parallel to the main proton bunch but often stir outward from the nominal orbit due to betatron oscillations, in the transverse direction spreading mostly in the horizontal plane, with respect to the CMS detector coordinates. Despite beam cleaning, a sizable population of beam halo muons remains and eventually produce energetic photons in the calorimeters. A scatter plot of the photon ECAL time against  $\phi$  shown earlier in the right plot of Figure 6.7, show that most of these beam halo muons enter the ECAL in the horizontal plane at  $\phi = 0, \pm\pi$ . The rate of halo-induced photons depend on the beam intensity, beam current and the operational conditions of the LHC, like, the machine optics, collimator settings, residual gas densities and LHC proton filling scheme.

The halo muons before entry into ECAL, produce tracks hits which can be reconstructed into muon tracks using segments in the Cathode Strip Chambers (CSC) Endcap muon detectors. The reconstructed tracks hits in the CSC segments can be associated with a halo-induce photon supercluster in ECAL within some narrow opening angle in  $\phi$ .

Due to the beam intensity, most of the halo muons end up in the endcaps, but, some can also end up in the barrel. The resulting halo-induced photons are usually out-of-time compared to photons produced directly from nominal  $pp$  collisions. All of halo-induced photons have early arrival time, since the beam halo muons arrive at the crystals in ECAL before those photons produced at the interaction point in  $pp$  collisions. The halo-induced photon's arrival time can be estimated from the unique flight path of the beam halo muons, with respect to the arrival time of photons from  $pp$  collisions, as

$$t_{\text{ECAL}}^{\text{expected}} = -1/c \left( \pm Z_{\text{cluster}} + \sqrt{Z_{\text{cluster}}^2 + R_{\text{cluster}}^2} \right), \quad (6.3)$$

where,  $Z_{\text{cluster}}$  is the point where the halo muon hits ECAL or the longitudinal distance along  $z$ -axis of the halo-induced photon supercluster position measured from the nominal interaction point,  $R$  is the radial distance of the supercluster from the beam line, which is equal to 1.29 m in the barrel, and  $c$  is the speed of light in vacuum. The estimated halo-induced photon arrival time can be re-arranged to become

$$t_{\text{ECAL}}^{\text{expected}} = -\frac{R}{2c} \exp(-\eta) \quad (6.4)$$

showing the direct dependence on  $\eta$ . In Figure 6.8, the halo-induced photon estimated time is shown as the two red lines, agreeing well with observation from data. This gives us confidence that we understand the source of halo-induced photons and can develop a method of identifying events with halo-induced photons.

By matching halo muon hit positions in CSC segments to photon supercluster positions in the ECAL in  $\phi$ , since halo muons spread mostly in the horizontal plane, we are able to match halo muons to their corresponding halo-induced photons. We use the quantity,  $\Delta\phi(\text{CSC Seg}, \gamma)$ , which is defined as the difference in  $\phi$  between the CSC segment and the photon supercluster position in ECAL, to express this matching. A plot of  $\Delta\phi(\text{CSC Seg}, \gamma)$  for in-time and out-of-time photons is shown in the left plot of Figure 6.8. We find that out-of-time photons often have small  $\Delta\phi(\text{CSC Seg}, \gamma)$ , further confirming that some out-of-time photons are produced by beam halo muons.

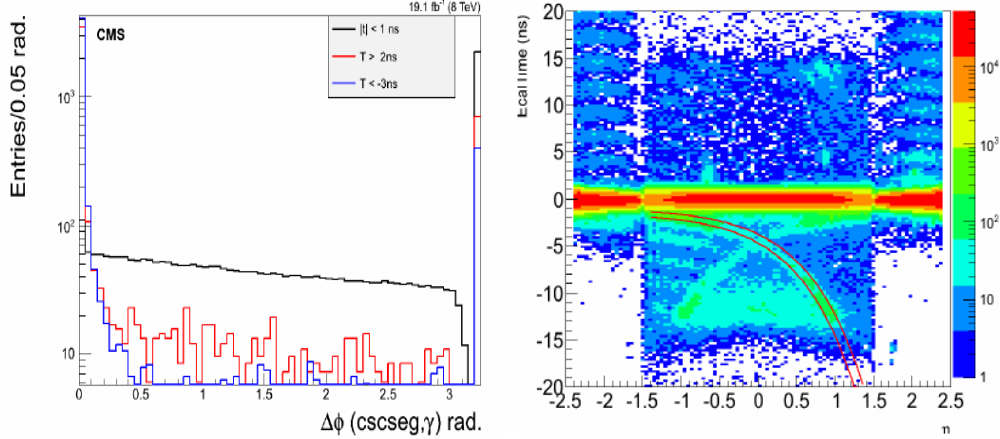


Figure 6.8: ECAL time *vs*  $\Delta\phi(\text{CSC Seg}, \gamma)$  (left) for in time (black) and out-of-time (red and blue) photons. Photon ECAL time *V.s*  $\eta$  (right), expected halo-induced photon time is shown as two red lines.

### Cosmic-induced Photons

Muons produced in cosmic rays with sufficient energy, traveling through the CMS detector, will radiate (bremsstrahlung) photons in ECAL. We refer to these photons as *cosmic-induced photons*. Unlike halo muons, muons from cosmic rays can arrive at ECAL from any direction at any time. We expect the cosmic-induced photons in the barrel to leave track hits, produced by the associated muons from cosmic, in the Drift Tubes (DT) segments found in the muon barrel behind the calorimeters.

Using DT segments and photon supercluster position, in  $\eta - \phi$  directions, in ECAL, we can match cosmic muon track hits in DT segments to ECAL photon superclusters within a narrow window in  $\Delta\eta$  and  $\Delta\phi$ . The DT position, used in the calculation of  $\Delta\eta$  and  $\Delta\phi$ , is a projection of the muon trajectory, using the direction of the DT segment, to the outer surface of ECAL; because of the large space between the muon barrel and the ECAL. A scatter plot for  $\Delta\eta(\text{DT Seg}, \gamma)$  and  $\Delta\phi(\text{DT Seg}, \gamma)$  of the matching, for events with out-of-time photons;  $t_\gamma > 2 \text{ ns}$  and  $t_\gamma < -3 \text{ ns}$ , is shown on the right plot of Figure 6.9. We compare these scatter plots of  $\Delta\eta(\text{DT Seg}, \gamma)$  and  $\Delta\phi(\text{DT Seg}, \gamma)$  to the scatter plots for in-time ( $|t_\gamma| < 1 \text{ ns}$ ), shown on the left plot, of the same Figure 6.9, and find that most out-of-time photons have a small  $\Delta\eta$  and  $\Delta\phi$ .

If we compare these scatter plots of  $\Delta\eta$  and  $\Delta\phi$ , for these out-of-time photons, to

the scatter plots for cosmic-induced photons from a pure cosmic muons sample (data recorded by the CMS detector without proton-proton collisions happening), shown in Figure 6.10, we find a similar small  $\Delta\eta$  and  $\Delta\phi$  occupancy for the true cosmic muons events from the pure cosmic sample. We conclude that, it is possible to use small  $\Delta\eta(\text{DT Seg}, \gamma)$  and  $\Delta\phi(\text{DT Seg}, \gamma)$ , to tag and reject events with cosmic-induced photons.

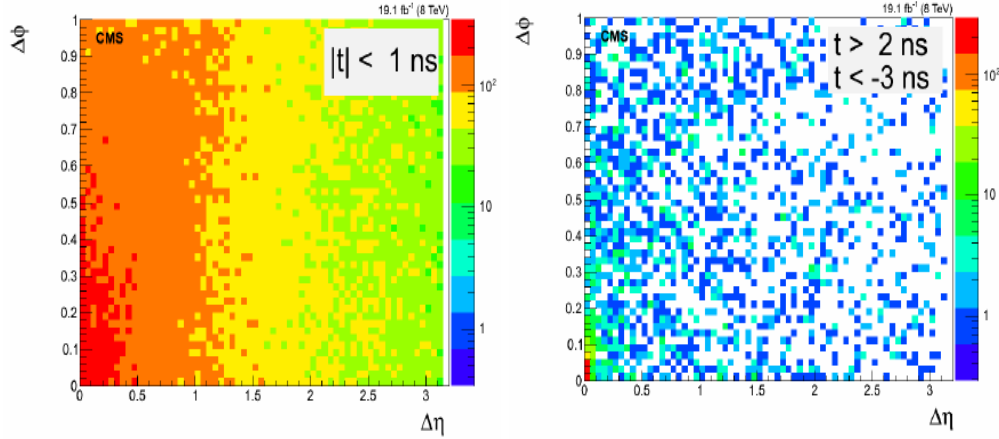


Figure 6.9: Scatter plot showing  $\Delta\eta(\text{DT Seg}, \gamma)$  against  $\Delta\phi(\text{DT Seg}, \gamma)$  for out-of-time ( $t_\gamma > 2 \text{ ns}$  and  $t_\gamma < -3 \text{ ns}$ ) photons (right) compared to in-time ( $|t_\gamma| < 1 \text{ ns}$ ) photons (left). Cosmic photon candidates have small  $\Delta\eta$  and  $\Delta\phi$ .

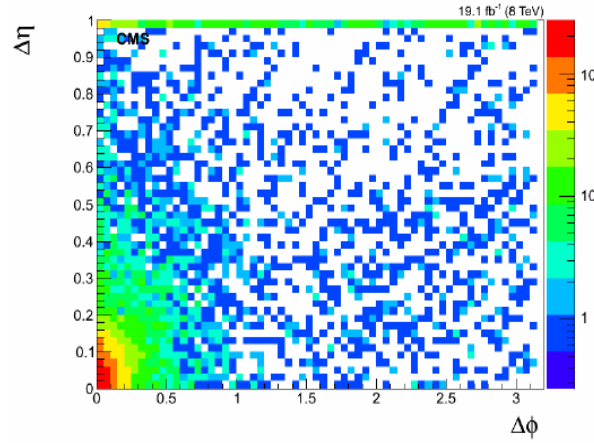


Figure 6.10: Scatter plot of  $\Delta\eta(\text{DT Seg}, \gamma)$  against  $\Delta\phi(\text{DT Seg}, \gamma)$  for photons from pure cosmic muon data. Small  $\Delta\eta$  and  $\Delta\phi$  are cosmic photons.

## Spike-Seeded Photons

Neutrons and charge hadrons can at times deposit their energy directly on the APDs in addition to going through the crystal scintillation process. Such signals, read from the APDs, are *anomalous* and referred to as *spike-seeded photons* or simply *spikes*. Spikes produced from  $pp$  collisions and passing our photon selection requirements, can easily be identified as good photon candidates. A spike supercluster consist of very few crystals; most often one or two crystals. Because spikes occupy few crystals, they can overlapped with good photon candidates, embedded in the photon's supercluster, or buried inside jets. Such embedded spikes cannot be easily identified.

The arrival time of spikes is much earlier (negative), usually about  $t = -12.0$  ns, than for photons produced in nominal  $pp$  collisions and depositing their energy, through crystal scintillation, on the APDs. This is because for spikes, there is the absence of the crystal scintillation process; which takes on average 10 ns. The few crystals holding the spike energy deposits, make it possible for spikes to be identified using a energy topological selection quantity, know as *swiss-cross* and defined as  $1 - \frac{E_4}{E_1}$ . A distribution of swiss-cross for in-time photon events, compare to events from a spike sample (events with photon time  $t = -12$  ns) is shown on the right plot of Figure 6.11. We find that most spikes have about 98% of their energy deposited in a single crystal.

Using the number of crystals in a photon supercluster and comparing the number of crystals belonging to in-time photons, halo-induced photons and spike-seeded photons (photons with  $1 - \frac{E_4}{E_1} > 0.98$ ), shown on the left plot of Figure 6.11, we conclude that most spikes, including spikes embedded in photon candidates, have less than 7 crystals belonging to their supercluster. A combination of the swiss-cross, number of crystals belonging to the supercluster, calculated  $\chi^2$  (defined in Equation 6.2) of ECAL time, and  $S_{\text{Minor}}$  ( $S_{\text{Minor}}$  describes the spread in width, in terms of number of crystals, of the photon electromagnetic shower), is useful for identifying and rejecting events with spike-seeded photons.

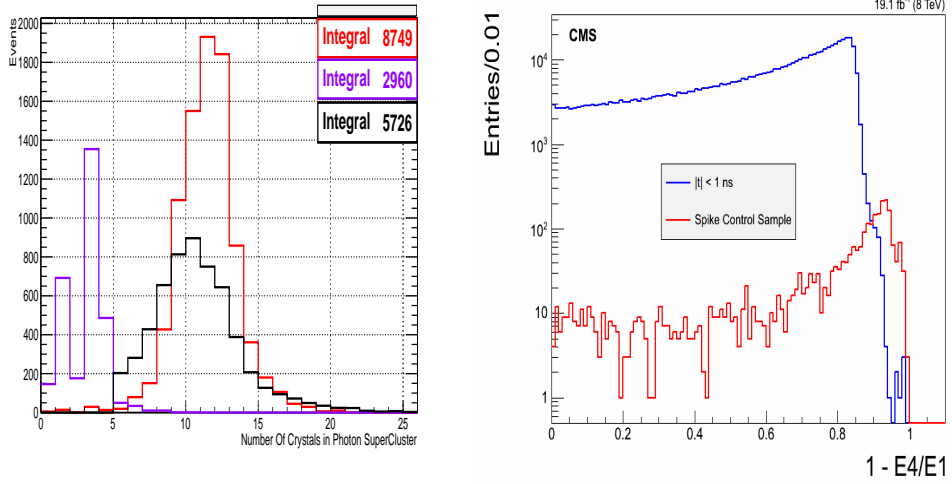


Figure 6.11: *Number of crystals* belonging to a photon supercluster (left) plot for in-time photon candidates (black), spike-seeded photon candidates (magenta) and halo-induced photon candidates (red). The spike-seeded photon candidates are selected using a swiss-cross variable ( $1 - E_4/E_1$ ) (right), shown comparing in-time photons ( $|t_\gamma| < 1.0$ ) to spike candidate sample selected using  $S_{Minor}$ .

### 6.4.3 Event Vetoing

We tag and veto events with halo-induced, cosmic-induced and spike-seeded photons as follows:

- An event with a halo-induced photon is tagged and vetoed, if a CSC segment for  $|\eta| > 1.6$ , is found within 0.05 radian of angle  $\phi$ , with the photon supercluster, i.e. a photon found within  $\Delta\phi(\text{CSC Seg}, \gamma) < 0.05$ , is vetoed.
- An event with cosmic-induced photon is tagged and vetoed, if the photon can be matched to a DT segment within  $\Delta\eta(\text{DT Seg}, \gamma) < 0.1$ , and  $\Delta\phi(\text{DT Seg}, \gamma) < 0.1$ .
- An event with spike-seeded photon is vetoed, if the photon has ECAL time  $\chi^2 > 4$ , number of crystals  $< 7$ ,  $1 - E_4/E_1 > 0.98$ , and  $S_{Minor} < 0.17$ .

The result of the event tagging is shown in Figure 6.12. We observe that most of the non-collision background events are events with halo-induced photons. Very few late arrival time photons are produced from spikes. There is also some significant contribution from cosmic-induced photons. The most interesting observation is the residual out-of-time background (in red) which could not be tagged.

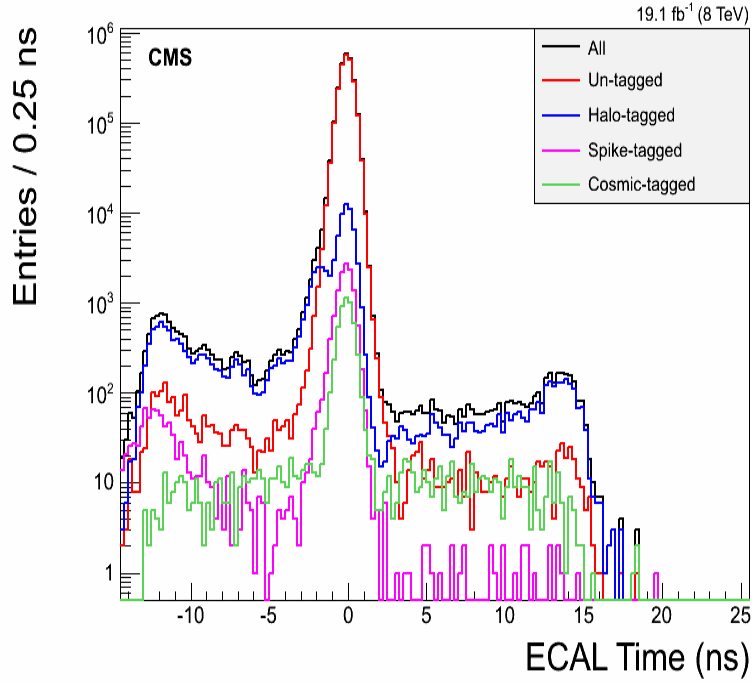


Figure 6.12: Photon ECAL time, for a data sample of 0 and 1-jet events, showing our tagging performance for non-collision background events.

These residual untagged events comprise of some non-collision events, since the tagging and vetoing are not 100% efficient, and mostly collision events with mis-measured time photons. In order to quantify our estimates of these different sources contributing to the untagged background events, we use control samples defined with  $\cancel{E}_T^\gamma$  and  $\cancel{E}_T$ .

We expect signal events, because of the undetected gravitino from the decay of  $\tilde{\chi}_1^0$ , to have large  $\cancel{E}_T^\gamma$  and  $\cancel{E}_T$ ; by large, we mean above 60 GeV. The non-collision (cosmic-induced, halo-induced, spike-seeded photons) and collision (ghost/satellite and QCD) background events can be categorized into high- $p_T$  and low- $p_T$  events. For high- $p_T$  non-collision events, we expect these events to have large  $\cancel{E}_T$ , due to the exclusion of the energy deposits from the out-of-time photons in the missing transverse energy reconstruction, and small  $\cancel{E}_T^\gamma$ , when the large transverse energy contribution from the energy deposits, of the out-of-time photons, is re-introduced, while for low- $p_T$  non-collision events, we expect these events to have both  $\cancel{E}_T^\gamma$  and  $\cancel{E}_T$  small, since the out-of-time photon transverse energy, which was excluded, was in the first place small.

For high- $p_T$  out-of-time collision events, which under normal circumstances should have large missing transverse energy, we expect their  $\cancel{E}_T$  to be large and after re-introducing the energy deposits from out-of-time high- $p_T$  photons, we expect their  $\cancel{E}_T^\gamma$  to be small, while, using the same argument made for low- $p_T$  non-collision events, we expect low- $p_T$  collision events to have both small  $\cancel{E}_T^\gamma$  and  $\cancel{E}_T$ . A summary of our expectations for  $\cancel{E}_T^\gamma$  and  $\cancel{E}_T$  for the different expected background events sources, with possible contribution to the residual untagged events with out-of-time photon, is presented in Table 6.5.

Event Sample	$\cancel{E}_T$	$\cancel{E}_T^\gamma$
Signal Events	Large	Large
High- $p_T$ Non-Collision(Mostly Beam Halo) Events	Large	Small
Low- $p_T$ Non-Collision Events	Small	Small
High- $p_T$ Collision(QCD/Ghost) Events	Large	Small
Low- $p_T$ Collision Events	Small	Small

Table 6.5: Summary of missing transverse expectation for events with out-of-time photons.

Using control samples defined using  $\cancel{E}_T$  and  $\cancel{E}_T^\gamma$  for events with in-time ( $|t_\gamma| < 2.0$  ns) photons, events with out-of-time photons,  $t_\gamma > 3.0$  ns and  $t_\gamma < -3.0$  ns, where each control sample is defined purposely to enhance the contribution of either collision or non-collision background events in the control sample, and simultaneously suppressing contributions from the other, we perform a background estimation in the signal sample ( $t_\gamma > 3.0$  ns,  $\cancel{E}_T^\gamma > 60$  GeV and  $\cancel{E}_T > 60$  GeV), using the so-called ABCD background estimation method and verify that the background estimation method is performing as expected using a data sample of zero and one jet events.

#### 6.4.4 Background Estimation with ABDC Method

Since we expect most of our background events to come from non-collision events, we estimate the number of events we expect from non-collision events in the signal control sample using the ABCD technique. We also estimate the possible contamination, we expect from collision events, to the control samples used in the ABCD method.

##### Non-Collision Background Estimation

To estimate the number of background events from non-collision events, we define regions labeled as ABCD, in photon ECAL time and  $\cancel{E}_T$ , for selected events with  $\cancel{E}_T^\gamma > 60$  GeV. Events with  $\cancel{E}_T^\gamma > 60$  GeV, defines a Control Sample (CS) in which the contribution from collision (QCD) background events is suppressed, since most collision background events have small  $\cancel{E}_T^\gamma$ , as we saw in Table 6.5. The regions: A and B, shown in Table 6.6, contain events with, respectively,  $\cancel{E}_T < 60$  GeV and  $\cancel{E}_T > 60$  GeV, and photon ECAL time,  $-10.0 < t_\gamma < -3.0$  ns, and region C, contain events with  $\cancel{E}_T < 60$  GeV and photon ECAL time,  $3.0 < t_\gamma < 13.0$  ns.

Non-Collision	$\cancel{E}_T < 60$ GeV	$\cancel{E}_T > 60$ GeV
$3.0 < t_\gamma < 13.0$ ns.	C	D
$-10.0 < t_\gamma < -3.0$ ns	A	B

Table 6.6: Definition of ABCD regions used for estimating non-collision background events in the signal region D. Events must satisfy the  $\cancel{E}_T^\gamma > 60$  GeV selection requirement, which reduces collision background events significantly.

The remaining collision background events, which may have some contribution in the B and D regions, are estimated in the next section and also corrected for.

Since the arrival time of photons is independent of the missing transverse energy in the event and since we are selecting events with out-of-time photons (where the definition of  $\cancel{E}_T$ , is the same for all events) in defining the ABCD regions, we expect the ratio in the number of events with high- $\cancel{E}_T$  and low- $\cancel{E}_T$ , for both out-of-time regions, to be the same, provided the contribution from collision events with mis-measured photon time is not large, i.e.  $\frac{N_D}{N_C} = \frac{N_B}{N_A}$ . With this, the number of non-collision background events, with out-of-time photons, expected in the signal region D, is given as

$$N_D^{non-col} = \left( \frac{N_B}{N_A} \right) \cdot N_C, \quad (6.5)$$

where,  $N_B$ ,  $N_A$  and  $N_C$ , are the number of events observed in B, A and C regions, in that order, and  $N_D^{non-col}$ , is the number of non-collision background events we expect in the signal region D.

### Collision Background Estimation

We want to estimate the contribution from collision background events to regions B and D of Table 6.6. Using the ABCD technique again, we define regions in photon ECAL time and  $\cancel{E}_T^{\gamma}$ , for selected events with  $\cancel{E}_T > 60 \text{ GeV}$ . The events with  $\cancel{E}_T > 60 \text{ GeV}$  define a control sample, where the contribution from collision events is dominant, as seen in Table 6.5. Since most collision events have in-time ( $|t_\gamma| < 2 \text{ ns}$ ) photons, the few collision events with out-of-time photons contributing to the B and D regions, because the photon time is mis-measured, can be estimated using regions with in-time photons. The definition of each region used in the ABCD method, to estimate the out-of-time photon collision background, is given in Table 6.7.

Collision	$\not{E}_T < 60 \text{ GeV}$	$\not{E}_T > 60 \text{ GeV}$
$3.0 < t_\gamma < 13.0 \text{ ns.}$	C	D
$-2.0 < t_\gamma < 2.0 \text{ ns}$	E	F
$-10.0 < t_\gamma < -3.0 \text{ ns}$	A	B

Table 6.7: A,B,C,D,E,F regions used for estimating collision background events with out-of-time photons contamination the regions B and D of Table 6.6. Here, events must satisfy  $\not{E}_T > 60 \text{ GeV}$ , selection requirement.

Using a similar argument that the photon arrival time is independent of the missing transverse energy, the number of collision events contributing to the region B,  $N_B^{col}$ , is estimated as

$$N_B^{col} = N_B = \left( \frac{F}{E} \right) \cdot N_A, \quad (6.6)$$

and the number of events contributing to the signal region D,  $N_D^{col}$ , is estimated as

$$N_D^{col} = N_D = \left( \frac{F}{E} \right) \cdot N_C, \quad (6.7)$$

where,  $N_i$ , is the number of events in each region,  $i = A, B, C, D, E, F$ .

### Combined Background Estimation

Now that we have estimates for both collision and non-collision event contributions, we can estimate the total number of background events expected in the signal region D (Events with  $\not{E}_T > 60 \text{ GeV}$ ,  $\not{E}_T > 60 \text{ GeV}$  and  $3.0 < t_\gamma < 13.0 \text{ ns}$ ), as

$$N_D^{Total} = \left( \frac{N_B - N_B^{col}}{N_A} \right) \cdot N_C + N_D^{col} = N_D^{non-col} + N_D^{col} \quad (6.8)$$

where,  $N_D^{Total} = N_D^{non-col} + N_D^{col}$ , is the total background events estimated in our signal region D from non-collision and collision background events.

### Background Estimation Method Validation

We verify that our background estimation method performs as expected using a data sample of 0 and 1-jet events. We do not expect signal events in this sample. A statistical agreement between the expected number of background events, obtained using our background estimation method, and the number of events observed in our signal region D, affirms that the method is reliable. The accepted 0 and 1-jet events used must pass the same event selection requirements as potential signal events described in Tables 6.3 and 6.4, in addition to vetoing non-collision background events. The event yields in each control sample including tagged events with halo-induced, cosmic-induced and spike-seeded photons is shown in Table 6.8.

Control Sample	Yield	Beam Halo	Cosmic	Spike
A	851	5075	237	65
B	38	300	17	1
C	359	1508	368	9
D	10	22	30	0
<hr/>				
A	8	1	1	0
C	2	0	0	0
F	35271	-	-	-
E	1445254	-	-	-
B	-	-	-	-
D	-	-	-	-

Table 6.8: Event yields used in validating the ABCD background estimation method using 0 and 1-jet events sample. Halo/cosmic/spikes yields are obtained from tagged events. All events must pass photon, jet and  $E_T^{\text{miss}}$  selection requirements.

Using the event yields in Table 6.8 for each region, and Equations 6.6, 6.7 and 6.8,

we obtain the following estimates for the expected number of events in signal region D:

$$\begin{aligned} N_B^{col} &= \frac{35271}{1445254} \times 8 = 0.64^{+0.35}_{-0.34}, \\ N_D^{col} &= \frac{35271}{1445254} \times 2 = 0.46^{+0.11}_{-0.09}, \\ N_D^{Total} &= \left( \frac{38 - 0.64}{851} \times 359 \right) + 0.46 = 16.41^{+3.00}_{-2.59}. \end{aligned}$$

The uncertainty are statistical uncertainties based on the event statistics in each region. Our expected number of background events in signal region D is  $16.41^{+3.00}_{-2.59}$ , which is, within the statistical uncertainties, agreeable with the 10 events we observe, satisfying all our event selection requirements, in the signal region D. This give us confidence in our background estimation method and the impetus to use the method in our background estimation of signal events.

#### 6.4.5 Background Estimation Cross Check

Another method for estimating our background events with out-of-time electromagnetic particles from collision, is using  $Z \rightarrow e^+e^-$  events, since we expect the electron candidates from Z decay to be in-time because of the prompt nature of the decay of Z bosons. We use events with electron candidates from a **SingleElectron** (single electron triggered events) and **DoubleElectron** (double electron triggered events) data samples, where we expect contributions from non-collision events to be very small. These events are selected such that out-of-time energy deposits in ECAL, from electron candidates, are accepted. The background events to the Z-boson events are events with candidate electrons from collision with mis-measured electron time. An out-of-time electron can be randomly matched with another candidate electron to give a di-electron mass which is of the order of the mass of Z. These background events also include events with poorly reconstructed out-of-time energy deposits in ECAL.

To reduce any out-of-time event from beam halo and cosmic events, occurring simultaneously with true  $pp$  collision events, we accept only events satisfying the following event selection requirements: the two electron candidates for the Z boson must each have a  $p_T > 30 \text{ GeV}/c$ , the di-electron mass,  $|m_{e^+e^-} - 91| > 61 \text{ GeV}/c^2$ , both electrons must be in the barrel, i.e.  $|\eta_{e^-}| < 1.479$  and  $|\eta_{e^+}| < 1.479$  and the electron ECAL arrival time

$\chi^2 < 4$ . The electron's arrival time is taken to be the seed crystal time, and corrected to account for the electron's time of flight, which is different from photons. The chosen seed crystal must satisfy the recommended crystal (reconstructed hit) cleaning criteria; which requires that the seed crystal is not a spike, is not noisy and has been properly time calibrated.

From the accepted events with Z candidates, we define a signal event sample for which the di-electron mass is between  $76 \text{ GeV}/c^2 < |m_{e^+e^-}| < 100 \text{ GeV}/c^2$ , i.e.  $76 \text{ GeV}/c^2 < m_{e^+e^-} < 100 \text{ GeV}/c^2$ , and a background or sideband event sample where the di-electron mass is either between  $50 \text{ GeV}/c^2 < m_{e^+e^-} < 76 \text{ GeV}/c^2$  or  $100 \text{ GeV}/c^2 < m_{e^+e^-} < 130 \text{ GeV}/c^2$ . The di-electron mass (left plot) and electron arrival time (right plot) of both electron candidates of the Z boson (signal (blue)) together with the total Z boson candidates is shown in Figure 6.13.

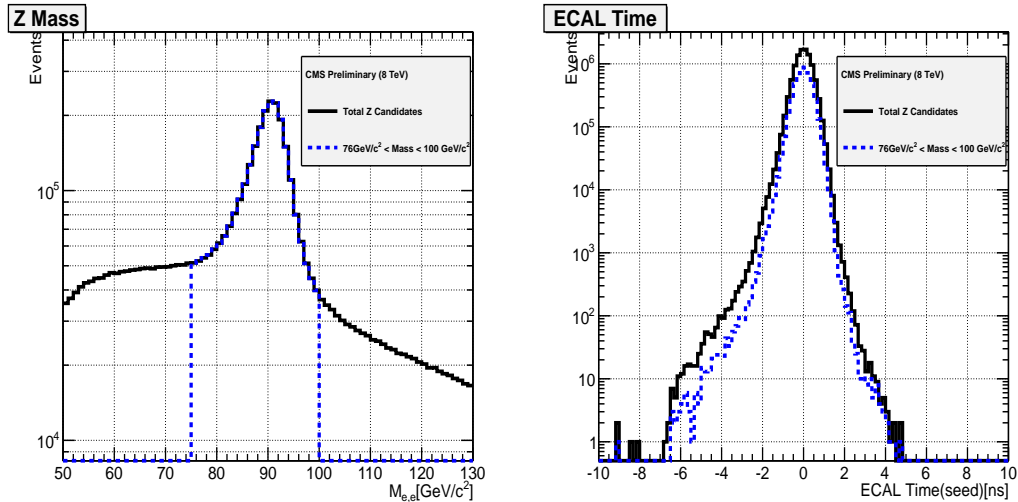


Figure 6.13: Di-electron mass distribution (left) and the time (right) of the two electron candidates for the signal,  $76 < m_{e^+e^-} < 100 \text{ GeV}/c^2$ , of Z boson sample. Events are from the Single/DoubleElectron data sample.

A scatter plot of the arrival ECAL time against  $\eta$  (top right plot) and  $\phi$  (bottom right plots) of both electrons of the Z is shown in Figure 6.14. A clear difference in the scatter plots is seen comparing events from the Single/DoubleElectron data sample (plots on the right), which do not have the familiar beam halo features (the “cross-shape” and

high event concentration at  $\phi = 0, \pm\pi$ ), to events from **SinglePhoton** data sample (plots on the left). We conclude that, the candidate Z event sample is free from contamination from non-collision events and is useful for estimating out-of-time background events from collisions.

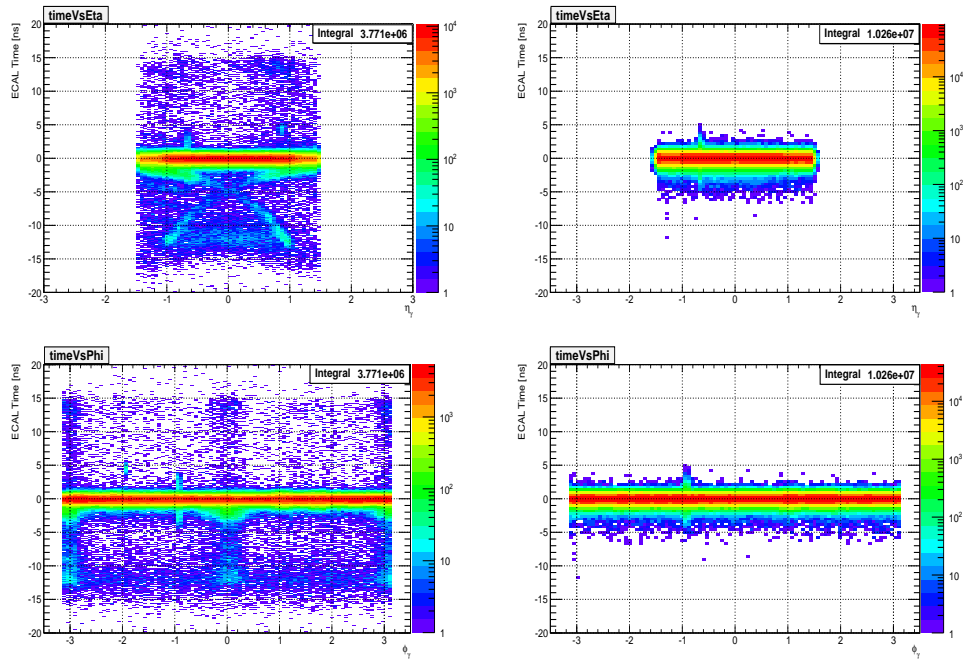


Figure 6.14: ECAL time  $Vs \eta$  (top plots) and  $Vs \phi$  (bottom plots) for electromagnetic particle candidates from **SinglePhoton** data sample (left) compared to electromagnetic particle candidates from the **Single/DoubleElectron** data sample (right). All electromagnetic particle candidates are in barrel. Most of the electromagnetic particles with “cross-shape” and at  $\phi = 0, \pm\pi$ , are halo-induced photons.

In order to estimate the out-of-time background events from collision, we estimate the probability for an in-time ( $|t| < 2$  ns) event to become out-of-time ( $t < -3$  ns or  $t > 3$  ns) because of the mis-measurement of the time of the electron candidates.

We estimate this probability by dividing the Z candidate events according to their arrival time as follows:

- In-time Z boson events: Both electrons of the Z boson candidate have arrival time,  $|t| < 2$  ns. Their di-electron mass is shown on the top right plot of Figure 6.15,

- Early time Z boson events: Both electrons of the Z boson candidate have arrival time,  $t < -3$  ns. Di-electron mass shown in the bottom left plot of Figure 6.15,
- Late time Z boson events: At least one of the electrons of the Z boson candidate have arrival time,  $t > 3$  ns. The di-electron mass is shown in the bottom right plot of Figure 6.15.

The true Z boson events in each of the three Z boson event samples, defined above, is estimated as follows: we first fit, with a polynomial function, a sideband ( $50 < m_{e^+e^-} < 76 \text{ GeV}/c^2$  and  $100 < m_{e^+e^-} < 130 \text{ GeV}/c^2$ ) of the di-electron mass distribution (see top left plot of Figure 6.15). Using the side band fit function, we subtract the integral of the fit function from the total number of Z boson candidates in the Z boson mass peak ( $76 < m_{e^+e^-} < 100 \text{ GeV}/c^2$ ) in each of the three samples. The result of the subtraction gives an estimate of the true Z boson events in the in-time and out-of-time Z boson event samples.

Table 6.9 show the resulting number of Z boson events.

Event Sample	Early Time ( $t < -3$ ns)	In-time ( $ t  < 2$ ns)	Late Time ( $t > 3$ ns)
Total	378	2349187.0	41.0
Estimated Z boson Background	329	996803.6	8.6
Estimated signal Z bosons	49	1352383.4	32.4

Table 6.9: Number of Z boson events with di-electron invariant mass,  $76 < m_{e^+e^-} < 100 \text{ GeV}/c^2$  in the in-time and out-of-time Z boson samples.

The 32.4 events for the late time Z boson events consist of 3 Z events with both electrons with time,  $t > 3$  ns. These 3 Z events could be attributed as produced from ghost/satellite bunch collisions since the ratio of these 3 events to in-time Z events (1.35 million) from main proton bunch collisions is of the order  $10^{-6}$ , which is consistent expected luminosity at collision for ghost/satellite bunches. The intensity of ghost/satellite proton bunch is about  $10^3$  less than that for the main proton bunch [38, 39].

The probability for in-time events becoming out-of-time for proton bunch collision is  $P_1$ , and can be estimated as  $29.4/1352383.4 = 1.09^{+0.28}_{-0.23} \times 10^{-5}$ , while the probability

for in-time events becoming out-of-time for ghost/satellite bunch collisions is  $P_2$ , and can be estimated as  $3/1352383.4 = 2.22_{-0.96}^{+1.7} \times 10^{-6}$ .

Using these probabilities we can predict the number of collision background events in out analysis, which have late time ( $t > 3.0$ ), as

$$N = n_1 \times P_1 + n_2 \times (2P_1(1 - P_1) + P_1^2) + n_1 \times P_2 + n_2 \times P_2 \quad (6.9)$$

where  $n_1$  is the number of in-time one photon events (28208) and  $n_2$  is the number of two photon in-time events (38) taken from the F region of the final results of our background estimation, shown in Table 6.11.

The estimated the number of background events from collisions in the signal region D,  $N_D^{col} = 0.370_{-0.072}^{+0.092}$ , events. Comparing this to the estimated background from collision, using the ABCD method, which is  $28283/1446522 = 0.093_{-0.047}^{+0.093}$ , events, we find that the two methods of estimating the number of background events from collision are not exactly equal. However, both method agree that the background contribution from collision events with out-of-time electromagnetic particles is almost negligible (less than a single event) such that the uncertainties on the ratio of out-of-time to in-time events used in our ABCD collision background estimation does not affect the final results.

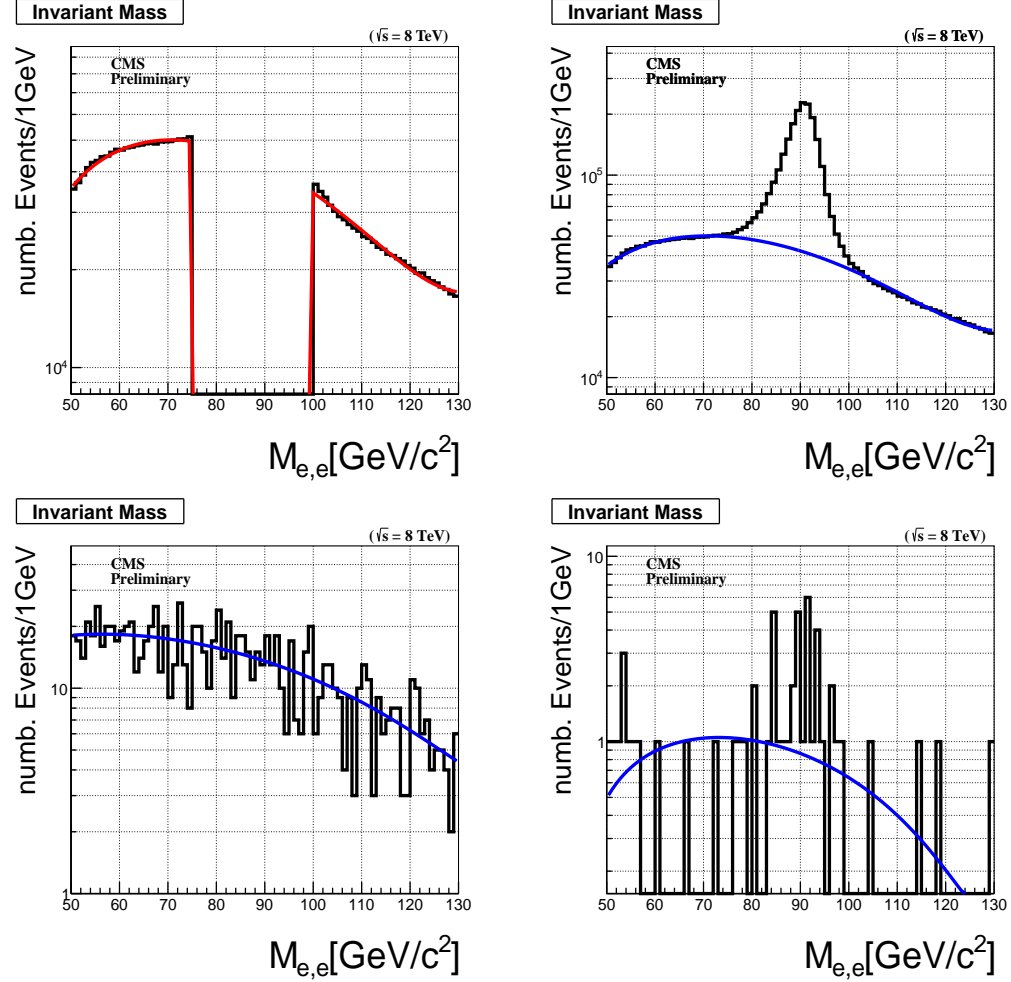


Figure 6.15: Di-electron invariant mass and polynomial fit (red) for sideband sample ( $50 < m_{e+e-} < 76 \text{ GeV}/c^2$  and  $100 < m_{e+e-} < 130 \text{ GeV}/c^2$ ). Di-electron invariant mass and polynomial fit (blue) for in-time ( $|t| < 2 \text{ ns}$ ) Z candidates (*top right*). Di-electron invariant mass and polynomial fit for out-of-time ( $t < -3 \text{ ns}$ ) Z candidates (*bottom left*). Di-electron invariant mass and polynomial fit for out-of-time ( $t > 3 \text{ ns}$ ) Z candidates (*bottom right*). The fits are used to estimate the number of true Z bosons in the int-time and out-of-time Z candidate samples.

## 6.5 Systematic Studies

We have required in our event selection that the photon  $p_T$  is greater than  $80\text{ GeV}/c$ , the jet  $p_T$  is greater than  $35\text{ GeV}/c$  and the missing energy is greater than  $60\text{ GeV}$ . The same selection requirements applied to our MC signal event sample should guarantee a good event selection efficiency estimate. Any difference in the photon  $p_T$ , jet  $p_T$  and missing transverse energy between MC and data, will be a source of systematic uncertainties on the efficiency of selecting signal events. These uncertainties can come from quantities like jet energy scale (JES), jet energy resolution (JER), electron-photon energy scale, instrumentation related and energy deposits not clustered during missing transverse energy reconstruction, photon ECAL arrival time bias and ECAL time resolution.

Table 6.10 presents the sources of uncertainties considered in this analysis. These uncertainties are computed by varying the nominal values of each quantity, while keeping the others fixed, by  $1\sigma$  deviation and counting the number of events passing our event selection requirements. ECAL timing bias which has to do with the absolute reference time (zero ns) of the ECAL timing, is the source of our largest uncertainty. The photon arrival time is measured with respect to this reference time. This ECAL time uncertainty has the largest impact on our analysis, since our analysis is based on counting the number of events with photon ECAL time above 3 ns. The next largest uncertainties are from energy deposits missed by the clustering algorithm. This affects the photon energy scale, missing energy scale, jet energy scale and resolution. The uncertainty on the photon energy scale in the barrel was estimated to be 4.0% which is based on measuring the photon energy of events with  $Z \rightarrow \mu\mu\gamma$  decay, where the muon radiates a photon in a process known as the final-state radiation (FSR) [61].

The uncertainty on the  $E_T^{\text{miss}}$  resolution uses a conservative estimate from  $E_T^{\text{miss}}$  measurements in QCD events [62], where the  $E_T^{\text{miss}}$  uncertainty is calculated using the fraction of events passing an event selection based on  $E_T^{\text{miss}}$  for varying thresholds of  $E_T^{\text{miss}}$ .

The uncertainty on the ECAL time resolution was obtained by comparing the mean time of photons of events from  $\gamma +$  jet MC sample to events from data with photon ECAL time,  $|t_\gamma| < 2\text{ ns}$ . The difference is found to be of the order of 200 ps per event.

Meanwhile, the systematic uncertainty on luminosity measurement has the recommended value of 2.2% provided by CMS and LHC luminosity measurements while the uncertainty from Parton Density Functions (PDF) is evaluated using the re-weighting technique which uses the Master Equation of CTEQ65 model set described in [63].

Since our background estimation is data-driven, the systematic uncertainties do not impact our results in a significant way. The statistical uncertainty in the ABCD background estimation method is our largest source of uncertainty in this analysis and we estimate it to vary upward by 223% and downward by 51%. This large background statistical uncertainty is because of the very low event yields. Our final result is affected by the signal selection efficiency only, despite the large background estimation uncertainty. These signal selection uncertainties are used as nuisance parameters in the calculation of the upper limit on the observed signal cross section ( $\sigma_{UL}$ ).

Source	Uncertainty(%)
ECAL absolute time (0.0 ns)	< 10.0%
ECAL time resolution (0.5 ns)	< 5.0%
Unclustered energy deposits	< 9.0%
Photon energy scale	< 4.0%
Jet energy scale (JES)	< 9.0%
Jet energy resolution (JER)	< 9.0%
$E_T^{\text{miss}}$ resolution	< 2.8%
PDF uncertainty	< 1.70%
Background estimation uncertainty	51.0% to 223%
Luminosity (4.5%)	< 2.2%

Table 6.10: Summary of systematic uncertainties for signal efficiency and background estimation in this analysis and applied to our final results.

## 6.6 Results

After running our analysis on the SinglePhoton data samples requiring events with at least 2 jets, at least one photon with ECAL time  $3.0 < t_\gamma < 13.0$  ns,  $\cancel{E}_T^\gamma > 60$  GeV, and  $\cancel{E}_T > 60$  GeV, we observed a single event passing all our event selection requirements as a signal candidate. This event has one photon and two jets. The photon has a transverse momentum of  $224$  GeV/c and an ECAL time of  $12.17$  ns.

Our expected number of background events estimated is  $0.093^{+0.301}_{-0.047}$ . This number was computed as

$$\begin{aligned} N_B^{col} &= \frac{28246}{604958} \times 3 = 0.140^{+0.108}_{-0.061} \\ N_D^{col} &= \frac{28246}{604958} \times 2 = 0.093^{+0.093}_{-0.047} \\ N_D^{Total} &= \left( \frac{1 - 0.14}{3} \times 0 \right) + 0.093 = 0.093^{+0.301}_{-0.047} \end{aligned}$$

using the event yields presented in Table 6.11.

In our final result, we use the collision background estimated using the  $Z \rightarrow e^+e^-$  method which gave us the following:

$$\begin{aligned} N_B^{col} &= 0.51^{+0.28}_{-0.27} \\ N_D^{col} &= 0.37^{+0.09}_{-0.07} \\ N_D^{Total} &= \left( \frac{1 - 0.51}{3} \times 0 \right) + 0.37 = 0.37^{+0.39}_{-0.07}. \end{aligned}$$

Control Sample	Yield
<b>Total Events</b>	
D	1
C	0
B	1
A	3
<b>Collision Background Events</b>	
A	2
C	4
F	28246
E	604958

Table 6.11: Event yields used in our final background estimation for signal candidate events with at least a single photon and at least 2 jets,  $\cancel{E}_T^{\gamma} > 60 \text{ GeV}$ , and  $\cancel{E}_T > 60 \text{ GeV}$ .

With no significant excess over expected number of background events, we find upper limits on the number of event counts at 95% confidence limit using the statistical CLs limit finding method.

## Chapter 7

# Statistical Analysis

### 7.1 Limit Computation

The upper limit calculation procedure used in this analysis is the CLs technique. We fed carefully estimated amounts of background and signal with systematic to obtain the limit. The variable for which the 95% upper limit is set unlike previous experiments is based entirely on the neutralino proper decay length,  $c\tau_{\tilde{\chi}_1^0}$ .

The method we used in our upper limit calculation is by first performing a Hypothesis test and then use the result of this test to derived our confidence intervals. We do the following:

- We define a NULL hypothesis ( $H_0$ ) and the Alternate hypothesis ( $H_1$ ). If we had several other hypothesis, we will defined them also.
- Select a Test statistics ( $t(x)$ ), where  $x$  is the data.
- Select a corresponding test statistics calculator.
- Use the result of the hypothesis test to compute the interval by inverting the result of the hypothesis test.

First, we describe the acceptable technique in experimental high energy physics for computing *p-values* used in any search and discovery experiment.

### 7.1.1 CLs Technique

The  $CL_s$  technique [64] is attributed as the standard technique or framework for computing the confidence or exclusion intervals in a search and discovery experiment. It has been shown to work during the search for the Higgs boson at LEP and recently in the discovery of the scalar boson in 2012, by both CMS and ATLAS experiments with the mass of this boson being:  $m_H = 125.36 \pm 0.37(\text{stat.Unc}) \pm 0.18(\text{syst.Unc})$ .

This method has been implemented in a unique statistical software package called *HiggsCombine* with the goal of providing direct access to a variety of robust statistical methods with optimised performance for computing limits or confidence intervals. *HiggsCombine* [66] is the official standard tool recommended by the CMS statistical committee and CMS Higgs group for calculating limits in any CMS search and discovery analysis. It takes as input estimates on the number or distribution of signal and background and the observed number or distribution from data and produces an upper limit in the production cross section of a given physics process for a given value of a parameter of interest (POI). *Higgscombine* tool has the advantage in that, it allows for the possibility to use several different statistical methods of calculating the upper limit. This way, one can make comparison and simple checks for any inconsistency. In this analysis, we used an Asymptotic [67] and HybridNew (a hybrid of Frequentist and Bayesian methods),[66], to calculate our observed upper limits. The purpose of the using the  $CL_s$  method is to compute reliable upper limits in a search scenario when the observed signal is very small compared to the background. In the  $CL_s$  technique, one uses not the p-value ( $CL_{s+b}$ ) but rather divide this by  $CL_b$  (which is 1 minus the p-value for background only hypothesis). The reason for this is to define a conditional probability conditioned to the scenario of observing only background or background only hypothesis. The  $CL_s$  is formally defined as:

$$CL_s = \frac{CL_{s+b}}{CL_b} = \frac{p_{s+b}}{1 - p_b} \quad (7.1)$$

where  $s + b$  means signal and background.

### 7.1.2 Statistical Test Formalism

The Neyman-Pearson Theorem states that the likelihood ratio gives the most powerful hypothesis test. Therefore, we construct our test statistics  $t_\mu$  as a function of the observed data, as a likelihood ratio. In a search analysis, one defines the null hypothesis  $H_0$  describing only known processes, or the background only which is to be tested against an alternate hypothesis  $H_1$  defined as a background and signal. However in the computation of upper limits:

- $H_0$  being the NULL hypothesis includes the background and signal ( $s + b$ ) while
- $H_1$  being the ALTERNATE hypothesis includes only the background ( $b$ ).

Using these, two hypothesis we quantify the level of agreement between our observed data with either of the hypothesis by computing a  $p$ -value ( $p$ -value if the probability under the assumption of a given hypothesis, of finding data of equal or greater incompatibility with the predictions of the given hypothesis). A given hypothesis is then regarded as being excluded if its  $p$ -value is observed below a given threshold. In particle physics, this threshold value for the  $p$ -value is 0.05 corresponding to 95% of confidence level (CL). The CMS accepted method of computing upper upper limit is based on mix of frequentist-hybrid significance test using the profilelikelihood ratio as a test statistics (HybridNew method). The parameter of interests in in our case the rate (cross section) of signal process as well as *nuissance parameters* as systematics for the background and signal models. This parametrized systematics effects results, as is always the case, to loss in sensitivity.

In this search experiment, for each event in the signal, we measured the timing of the photon as our observable. We use this value to construct a histogram  $\mathbf{n} = (n_1, \dots, n_N)$ . The expectation value for each value of  $n_i$  can be written as:

$$E[n_i] = \mu s_i + b_i \quad (7.2)$$

where  $\mu$  is the parameter which determines the signal strength, when  $\mu = 0$  means background-only and when  $\mu = 1$  then we have the signal and background hypothesis.

The the mean number of entries in the  $i$ th bin from signal and background are given as:

$$s_i = s_{tot} \int_{bin,i} f_s(t; \theta_s) \quad b_i = b_{tot} \int_{bin,i} f_b(t; \theta_b) \quad (7.3)$$

with the functions  $f_s(t; \theta_s)$  and  $f_b(t; \theta_b)$  being the probability density functions (Pdfs) of the variable  $t$  for the signal and background events and  $\theta_s$  and  $\theta_b$  representing the parameters which characterise the shapes of the pdfs.  $s_{tot}$  and  $b_{tot}$  represents the total mean numbers of signals and backgrounds while the integrals represent the probabilities for an event to be found in bin  $i$ .  $\theta = (\theta_s, \theta_b, b_{tot})$  denote all nuisance parameters (systematic uncertainties) while  $s_{tot}$  is the signal normalization is fixed to the value predicted by the nominal signal model.

The likelihood function is the product of the Poisson probabilities for all bins:

$$\mathcal{L}(\mu, \theta) = \prod_{r=1}^N \frac{(\mu s_r + b_r)^{n_r}}{n_r!} e^{-(\mu s_r + b_r)} \cdot \mathcal{G}(\theta) \quad (7.4)$$

where  $\mathcal{G}(\theta)$  is a discrete (Poisson) distribution of the nuisance parameters. This distribution can be different for different nuisance parameter.

Using the likelihood function, the profilelikelihood ratio is then defined as:

$$\lambda(\mu) = \frac{\mathcal{L}(\mu, \hat{\theta})}{\mathcal{L}(\hat{\mu}, \hat{\theta})} \quad (7.5)$$

Here  $\hat{\theta}$  is the the value of  $\theta$  that maximizes  $\mathcal{L}$  for a specified  $\mu$ , thus, it is referred to as the *conditional maximum-likelihood estimator* (CMLE) of  $\theta$  (given as a function of  $\mu$ ). While  $\mathcal{L}(\hat{\mu}, \hat{\theta})$  is the maximized (unconditional) likelihood function with  $\hat{\mu}$  and  $\hat{\theta}$  being its *maximum likelihood* (ML) estimators. The nuisance parameters broadens the profilelikelihood as a function of  $\mu$  relative to what is expected if their values where fixed and this reflects in the loss of sensitivity or information about  $\mu$  due to the systematic uncertainties.

### 7.1.3 Test Statistics and $p$ -values

The above expression for  $\lambda(\mu)$  shows that  $0 \leq \lambda \leq 1$ , where  $\lambda$  close to 1 indicates a very good agreement between the data and hypothesis value of  $\mu$ . The test statistics to be used for our statistical test is defined as:

$$t_\mu = -2 \ln \lambda(\mu) \quad (7.6)$$

It is important to note that the test statistics approach to any statistical test is favourable because just by looking at the values of the test statistics, higher values corresponds to increasing incompatibility between the data and the value of  $\mu$  which is from the signal hypothesis. This incompatibility or disagreement between the data and a given hypothesis is quantified by calculating the probability or  $p$ -value as:

$$CL_{s+b} = p_u = \int_{t_{\mu,obs}}^{\infty} f(t_\mu|\mu) dt_\mu \quad (7.7)$$

where,  $t_{\mu,obs}$  is the value of the test statistics  $t_\mu$  obtained from the data and  $f(t_\mu|\mu)$  is a pdf constructed from  $t_\mu$  depending on the signal strength  $\mu$ . The set of values for  $\mu$  that are rejected because their  $p$ -value is below a specified threshold value  $\alpha$  lying on either sides of those not rejected gives a two sided confidence interval of  $\mu$  and if just on one side of the ones not rejected gives an upper limit on the rejected values of  $\mu$ .

In the background only scenario i.e  $\mu = 0$ , the test statistics is defined as:

$$q_\mu = \begin{cases} -2 \ln \lambda(0), & \hat{\mu} \geq 0 \\ 0, & \hat{\mu} \leq 0 \end{cases}$$

where  $\lambda(0)$  is the profilelikelihood ratio for  $\mu = 0$  defined in 7.5. and again to quantify the disagreement between the background-only hypothesis ( $\mu = 0$ ) and the data is given by the  $p$ -value as:

$$CL_b = p_0 = \int_{q_{0,obs}}^{\infty} f(q_0|0) dq_0 \quad (7.8)$$

where  $f(q_0|0)$  denotes the pdf if the test statistics  $q_0$  under the background-only ( $\mu = 0$ ) hypothesis. Figure 7.1 shows a sampling distributions of the test statistics and how the

*p*-values can be extracted from these distributions.

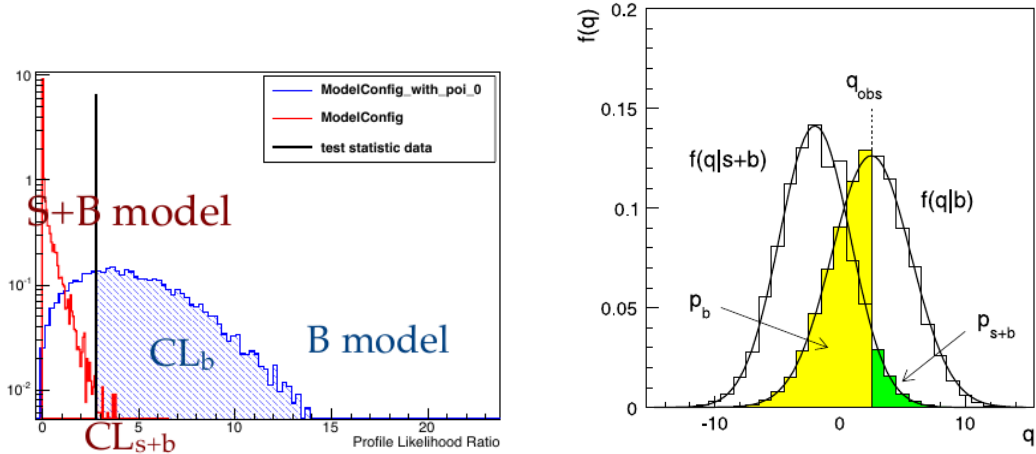


Figure 7.1: Sampling distributions for  $f(t_\mu|\mu)$  showing how one extracts the  $p$ -values. left: is the using a analytic of the Asymptotic method and right: is from the HybridNew method.

In addition to the  $p$ -value, for expressing the disagreement between the data and a given hypothesis, the Higgscombine tool also provides a quantity known as the *significance* ( $\mathcal{Z}$ ).  $\mathcal{Z}$  and the  $p$ -value have a very non-linear relation. Once can defined that relation using a two-sided fluctuation if a Gaussian variable  $\sigma$ , with  $5\sigma$  significance corresponding to a  $p$ -value of  $p = 5.7 \times 10^{-7}$  to denote a discovery. Since, we have not observed any significant excess of events over our standard model background, we will not mention a lot about significance in this thesis, but rather talk about  $p$ -values as they are indispensable in computing limits.

The important question is always, how does one obtain an expression or a distribution of the test statistics and  $f(t_\mu|\mu)$  from the likelihood function? To answer this question, the HiggsCombine tool was developed which consist of various ways of both analytically (e.g the Asymptotic statistical method [67]) or through numerical integration or Monte Carlo computation ( e.g the HybridNew statistical method) obtain the test statistics and  $f(t_\mu|\mu)$ . We have shown the limit computation results of both methods as used in this analysis. As an example, the pdf  $f(q_\mu|\mu)$  of the test statistics ( $q_\mu$ ) obtained though the **Asymptotic** statistical method as given in [67] is:

$$f(t_\mu|\mu') = \Phi\left(\frac{\mu - \mu'}{\sigma}\right)\delta(t_\mu) + \frac{1}{2}\frac{1}{\sqrt{2\pi}}\frac{1}{t_\mu}\exp\left[-\frac{1}{2}\left(\sqrt{t_\mu} - \frac{\mu - \mu'}{\sigma}\right)^2\right] \quad (7.9)$$

where result to a half-chi-square distribution when  $\mu = \mu'$ .

In subtle point worth mentioning is that in the HybridNew approach, systematics uncertainties are taken into account through the Bayesian prior density  $\pi(\theta)$ , and the distribution of the test statistics is computed under the assumption if the Bayesian model of average given as:

$$f(q) = \int f(q|\theta)\pi(\theta)d\theta$$

and the prior pdf  $\pi(\theta)$  is obtained from some measurements characterised by a given likelihood function  $\mathcal{L}_\theta(\theta)$  which is then used to find the prior using Bayes' Theorem. Unlike other cases where systematic uncertainties are taking as being part of the data and incorporated directly through  $\mathcal{G}(\theta)$  as shown in equation 7.4. Nevertheless, they arrive at the same result.

In summary, the hypothesis test is performed using a given statistical method on each value of a chosen parameter of interest (POI)(usually denoted  $\mu$ ). The  $p$ -value if obtained from the sampling distribution of the test statistics being used. Can either obtain this test statistics analytically or through Monte Carlo computation and numerical integration. By plotting the p-value as a function of the POI, we obtain the p-value curve (in this case the  $CL_s = \frac{CL_{s+b}}{CL_b}$ ). The value of  $\mu$  which has a p-value  $\alpha$  ( e.g 0.05) is the upper limit (for 1-dimensional limits,2-dimensional limits gives lower and upper limits) of  $1 - \alpha$  confidence interval (e.g 95%).

## combined result

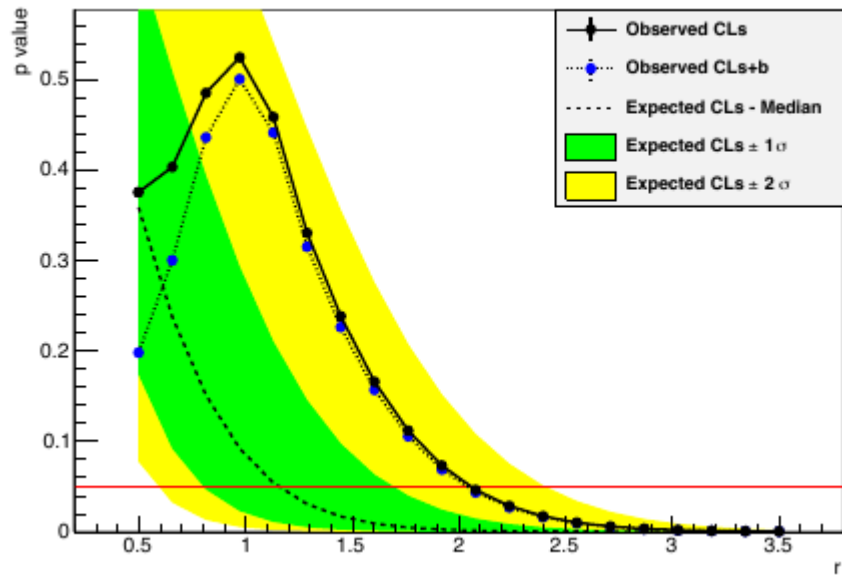


Figure 7.2: Distribution of  $p$ -values showing how upper limit on  $\mu$  is extracted for a given threshold probability.

## Chapter 8

# Limit Interpretation

Using the  $CL_s$  technique, the HiggsCombine tool produces an upper limit along with the expected limit at different quantiles as the signal strength computed which is a ratio of Number of Signal events over the Number of Expected signal events i.e

$$r = \frac{N^{Obs}}{N_{expect}} \quad (8.1)$$

and using the equation as given in chapter 3 on the cross-section  $\sigma = \frac{N}{\varepsilon \cdot A \cdot \mathcal{L}}$  and hence the observed cross-section upper limit is given as:

$$\sigma_{UL}^{Obs} = \frac{r \cdot N^{expect}}{\varepsilon \cdot A \cdot \mathcal{L}} \quad (8.2)$$

where  $\mathcal{L}$  is the integrated luminosity ( $19 \text{ fb}^{-1}$ ) and  $\varepsilon$  and  $A$  are the signal selection efficiency and Acceptance respectively. In addition to the observed limits (Solid black line), the uncertainties on the expected limits at 68%/16% ( $\pm 1\sigma$ ) and at 98%/2.5% ( $\pm 2\sigma$ ) provide the **GREEN** and **YELLOW** respectively, the error from the median (50%) expected limits (dashed red line) shown in figure 8.2.

### 8.1 Signal Efficiency and Acceptance

After our final selection on MC signal sample, the number of signal events passing our selection requirements for different neutralino lifetime and same mass,  $\Lambda = 180 \text{ TeV}$ , is

given in table 8.1. We use these numbers and those for other neutralino lifetimes and masses to compute our exclusion limits.

SPS8 GMSB Signal	Number of Events
GMSB(SPS8) ( $\Lambda = 180$ TeV, $c\tau = 250$ mm)	0.2096
GMSB(SPS8) ( $\Lambda = 180$ TeV, $c\tau = 500$ mm)	4.5423
GMSB(SPS8) ( $\Lambda = 180$ TeV, $c\tau = 1000$ mm)	6.3646
GMSB(SPS8) ( $\Lambda = 180$ TeV, $c\tau = 2000$ mm)	6.3968
GMSB(SPS8) ( $\Lambda = 180$ TeV, $c\tau = 4000$ mm)	6.1442
GMSB(SPS8) ( $\Lambda = 180$ TeV, $c\tau = 6000$ mm)	4.6498
GMSB(SPS8) ( $\Lambda = 180$ TeV, $c\tau = 12000$ mm)	2.918

Table 8.1: Final number for  $\Lambda = 180$  TeV GMSB SPS8 MC signal events events passing our selection cuts.

The efficiency times acceptance ( $\varepsilon \times A$ ) combined as one is seen the figure 8.1.

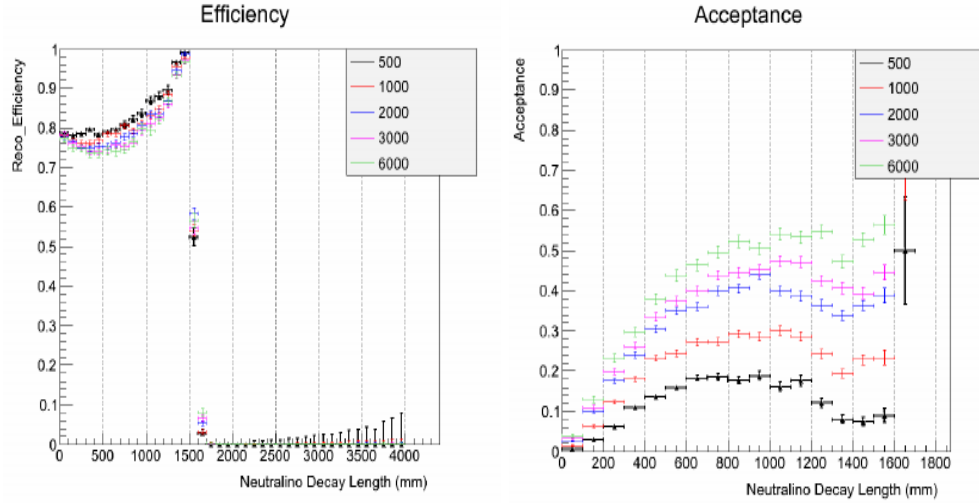


Figure 8.1: The reconstruction and selection efficiency (left)  $\times$  Acceptance ( $t > 3$  ns) (right) against transverse decay length in laboratory frame for different  $c\tau$  points.

The  $\frac{N_{expect}}{\mathcal{L}}$  defines the expected signal cross section which is obtained from a given signal model. In our scenario, our choice of signal model we want to produce exclusion limits on the possible production and decay of a long-lived particle described by this signal model is GMSB. Thus the interpretation of our search analysis is given within the context of any GMSB model with a long-live neutral particle decaying to a photon and gravitino. Such a model is the minimal GMSB or the SPS8 model and the general GMSB model. However, the results provided are based on interpretation within the context of the SPS8 model. In GMSB, the neutralino  $\tilde{\chi}_1^0$  is the NLSP and decays to the gravitino  $\tilde{G}$  the LSP (as a result of R-parity conservation) in association with a very energetic photon  $\gamma$ . Because of the smallness in mass difference between the  $\tilde{\chi}_1^0$  and the  $\tilde{G}$  as well as the coupling, the  $\tilde{\chi}_1^0$  decay to  $\tilde{G}$  is delayed and as a result, the photon emitted can arrive late in the calorimeter crystals. Measuring the arrival time of the photon on ECAL crystals, we can extract important parameters of theory of GMSB.

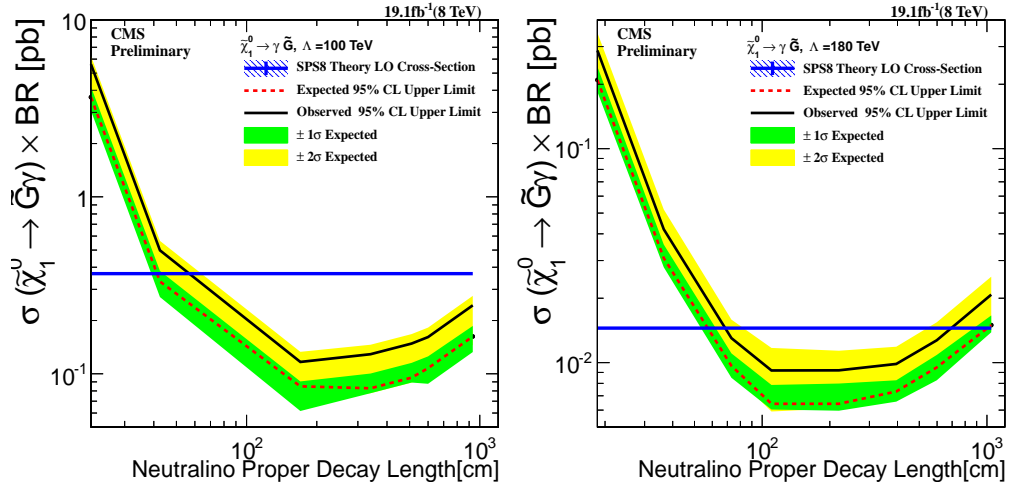


Figure 8.2: Neutralino production cross section against proper delay length upper limit interpretation in SPS8 model. (Left)  $\Lambda = 100$  TeV, (Right)(left)  $\Lambda = 180$  TeV

In the SPS8 model, the parameter space for long-live neutralinos is govern by  $\Lambda_m - c\tau$  2-dimensional parameter space. For each  $\Lambda_m$  point, we have a fixed neutralino mass with different proper lifetimes  $c\tau$ . We have obtained limits for  $\Lambda_m$  ranging from 100 TeV

to 180 TeV corresponding to lightest neutralino mass  $m_{\tilde{\chi}_1^0}$  between 90 to 255  $GeV/c^2$  and proper lifetime  $c\tau$  ranging from 250 to 12000 mm corresponding to  $\tau_{\tilde{\chi}_1^0}$  from 0.8 ns to 40 ns.

For a given value of  $\Lambda_m = 180$  TeV, we have a lightest neutralino production cross section times branching ratio plot shown in figure 8.2, showing that the ECAL detector is sensitive to lightest neutralinos of mass  $m_{\tilde{\chi}_1^0} = 255$   $GeV/c^2$  and life time upto 30 ns and we are 95% confident that we have not missed any neutralino whose mass is  $m_{\tilde{\chi}_1^0} = 255$   $GeV/c^2$  and lifetime is  $\tau \leq 30$  ns.

For a given lifetime of  $\tau = 20$  ns, we can also obtain upper limits on the production cross section times branching ratio when compared against their theoretically expected values for a lightest neutralino with mass ranging from  $m_{\tilde{\chi}_1^0} = 90$   $GeV/c^2$  to  $m_{\tilde{\chi}_1^0} = 255$   $GeV/c^2$ . The observed upper limit on this cross section is  $\sigma_{\tilde{\chi}_1^0}^{UP} \geq XX$  pb with proper lifetime of  $\tau = 30$  ns.

Using both the mass and proper lifetime of the lightest neutralino, we present possible 2-dimensional limits simultaneously on  $m_{\tilde{\chi}_1^0}$  or  $\Lambda_m$  and  $c\tau$  or  $\tau$  in the SPS8 model, comparing this with the result of previous experiments. This is shown in Figure 8.3.

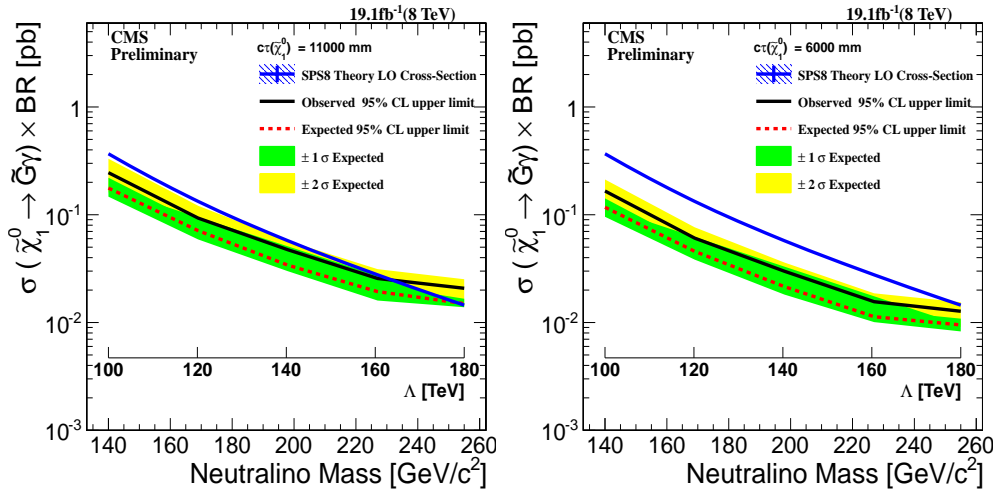


Figure 8.3: Neutralino production cross section against neutralino mass upper limit at 95% confidence levels interpretation in SPS8 model.(Left)  $C\tau = 11000$  mm, (Right)  $C\tau = 6000$  mm

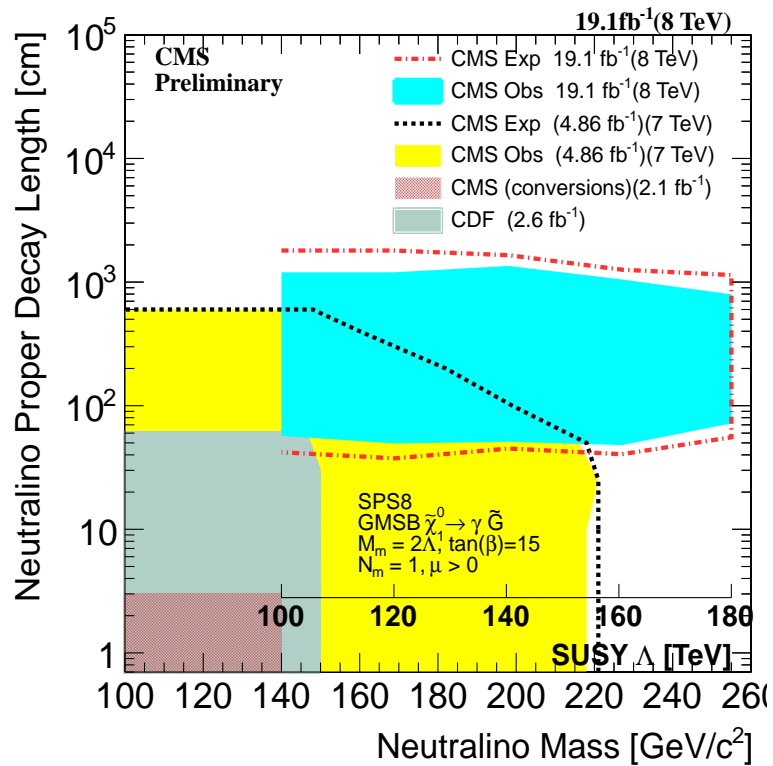


Figure 8.4: Neutralino two dimensional exclusion limit of neutralino mass ( $\Lambda$ ) against proper delay length upper limit interpretation in SPS8 model in the decay  $\tilde{\chi}_1^0 \rightarrow \gamma + \tilde{G}$  with limits from previous experiments shown.

# Chapter 9

## Conclusion

We have performed a search analysis for NMLLP decaying to photons using the time of arrival of the photon as measured by the ECAL sub detector of the CMS detector. Haven fail to find any significant signal of delayed photons over the standard model background, we interpreted our results in SUSY models with NMLLP like SPS8 of minimal GBSM or general GMSB models. We showed that, neutralinos whose production and decay mechanism is described in the SPS8 mGMSB model, with  $m_{\tilde{\chi}_1^0} \leq 235 \text{ GeV}/c^2$  and  $\tau_{\tilde{\chi}_1^0} \leq 35 \text{ ns}$  are ruled out of existence at 95% confidence level using the 2012 8 TeV LHC dataset. This corresponds to an upper limit of  $\sigma_{\tilde{\chi}_1^0}^{UP} \geq 0.02 \text{ pb}$  on the production cross section times branching ratio in a hadron collider. In addition, we mention some of the limitations in this particular analysis from a detector point of view and how in future studies can be improved. We hope that in the future, with increase in center of mass energy of the LHC collider as well as luminosity and an improve in timing resolution beyond what is already very reliable, we will surely find a new fundamental particle whose dynamics cannot be described by the already very successful standard model of particle physics.

# Bibliography

- [1] N. Jarosik et al. (WMAP), *Astrophys. J. Suppl.* **192**, 14 (2011); Overview: K.A. Olive et al.(PDG), *Chin.Phys.C***38**,090001(2014).
- [2] Ellis John, Olive Keith A. (2010). *Supersymmetric Dark Matter Candidates*. arXiv:1001.3651 [astro-ph]
- [3] Laura Covi, *Gravitino Dark Matter confronts LHC* Journal of Physics: Conference Series 485 (2014) 012002
- [4] M. Kuhlen, M Vogelsberger, R. Angulo, *Phys.Dark Univ.***1**,50(2012).
- [5] J.Ellis, J.Hagelin, D. Nanopoulos, K.A. Olive and M. Srednicki; *Nucl. Phys.* B238 (1984) 453; H. Goldberg, *Phys. Rev. Lett* 50 (1983) 1419; J. Ellis, T. Falk, G. Ganis, K.A. Olive and M. Srednicki, *Phys. Lett. B* 510 (2001) 236, arXiv: hep-ph/0102098.
- [6] K.A. Olive et al. (Particle Data Group), *Chin. Phys. C*, 38, 090001 (2014).
- [7] Steven Weinberg, *A Model of Leptons*, *Phys. Rev. Lett.* 19, 12641266 (1967)
- [8] Peter W. Higgs *Broken symmetries and the masses of gauge bosons*, *Phys.Rev.Lett.* 13.508,19 October, 1964;
- [9] *Observation of a new boson at a mass of 125 GeV with the CMS experiment at LHC*, *Phys. Lett. B* 716 (2012) 30-61
- [10] Haag, Rudolf; Sohnius, Martin; opuszaski, Jan T. *All possible generators of supersymmetries of the S-matrix*, *Nuclear Physics B* 88: 257274 (1975),

- [11] Salam, A.; Strathdee, J. (1974). *Super-gauge transformations*. Nuclear Physics B 76 (3): 477201,
- [12] Ian J R Aitchison, *Supersymmetry and the MSSM: An Elementary Introduction*, arXiv:hep-ph/0505105,
- [13] S.Mathin,*Supersymmetry Primer*, arXiv:hep-ph/9709356,
- [14] Howard Baer, Xerxes Tata, *Weak Scale Supersymmetry:From Superfields to Scattering Events.*
- [15] H. Nilles, *Supersymmetry, Supergravity and Particle Physics*, Phys. Rept. 110(1984) 1.
- [16] G.F. Giudice and R. Rattazzi *Theories with Gauge-Mediated Supersymmetry Breaking* arXiv:hep-ph/9801271v2.
- [17] S. Ambrosanio 1 , Graham D. Kribs 2 , and Stephen P. Martin hep-ph/9703211  
arXiv:hep-ph/9703211v2.
- [18] B.Allanach et al,arXiv:hep-ph/0202233v1.
- [19] D.del Re et al, *An algorithm for the determination of the flight path of long-lived particles decaying into photons*, CMS AN -2010/212.
- [20] ISAJET 7.84, F.E. Paige, S.D. Protopopescu, H. Baer and X. Tata,  
<http://www.nhn.ou.edu/~isajet/>
- [21] T. Sj ostrand, S. Mrenna, and P. Skands, *PYTHIA 6.4 physics and manual*, JHEP 05 (2006) 026, doi:10.1088/1126-6708/2006/05/026, arXiv:hep-ph/0603175
- [22] GEANT4 Collaboration, *GEANT4a simulation toolkit*, Nucl. Instrum. Meth. A 506(2003) 250, doi:10.1016/S0168-9002(03)01368-8.
- [23] J.Dann et al.(LEPSUSY Working Group), Internal note LEPSUSYWG/97-04(1997), P. Janot, talk at the EPS Conference, Jerusalem, 1997.
- [24] CDF Collaboration, *Search for Supersymmetry with Gauge-Mediated Breaking in Diphoton Events with Missing Transverse Energy at CDFII*,Phys. Rev. Lett.

- [25] ATLAS Collaboration *Search for Diphoton Events with Large Missing Transverse Momentum in 1  $fb^{-1}$  of 7TeV Proton-Proton Collision Data with the ATLAS Detector*, arXiv:1111.4116v1, 17th Nov 2011.
- [26] CMS Draft Analysis, *Search for Long-Lived Particles using Displaced Photons in PP Collision at  $\sqrt{S} = 7$  TeV*, CMS AN AN-11-081 104(2010)011801,
- [27] ATLAS Collaboration, J. High Energy Phys. 1212, 124 (2012), arXiv:1210.4457 [hep-ex]
- [28] The LHC Machine, Lyndon Evans and Philip Bryant *Jinst*,
- [29] CMS Collaboration, *CMS Physics: Technical design report*, Volume 1 CERN-LHCC-2006-001.
- [30] CMS Collaboration, *CMS Physics: Technical design report, Volume 2* CERN-LHCC-2006-001.
- [31] The CERN Brochure 2009-003-Eng.
- [32] CMS Collaboration, *The CMS experiment at the CERN LHC*, JINST 0803:S08004, 2008.
- [33] CMS Collaboration, *CMS trigger and data taking in 2010*, CMS CR-2011/051.
- [34] *Timing Distribution at the LHC*, B.G. Taylor Colmar, 9-13 September 2002
- [35] *An FPGA based multiprocessing CPU for Beam Synchronous Timing in CERNs SPS and LHC*. Proceedings of ICAL EPICS 2003, Gyeongju, Korea ICAL EPICS 2003
- [36] *Timing and Synchronization in the LHC Experiments*, Varela, J. Krakv, 11-15 September 2000.
- [37] <http://ttc.web.cern.ch/TTC/intro.html>
- [38] *Study of the LHC ghost charge and satellite bunches for luminosity calibration.*, CERN-ATS-Note-2012-029 PERF
- [39] *LHC bunch current normalization for the April-May 2010 luminosity calibration measurements.*, CERN-ATS-Note-2011-004 PERF

- [40] CMS Collaboration, *The electromagnetic calorimeter. Technical design report.*, CERN-LHCC-97-33.
- [41] Bo Lofstedt, *The digital readout system for the CMS electromagnetic Calorimeter*, *Nucl. Inst. Methods in Physics Research*, A 453 (2000) 433-439.
- [42] CMS Electromagnetic Calorimeter Collaboration, *Energy resolution of the barrel of the CMS Electromagnetic Calorimeter*, *JINST* 2(2007)P04004.
- [43] CMS Collaboration, *Reconstruction of the signal amplitude of the CMS electromagnetic Calorimeter*, *Eur.Phys.J.* C46S1(2006)23-35.
- [44] CMS Collaboration, *Time Reconstruction and Performance of the CMS Crystal Electromagnetic Calorimeter*, *CFT-09-006*, 2009.
- [45] <https://twiki.cern.ch/twiki/bin/viewauth/CMS/ECALDPGTimeCalibration>
- [46] <https://twiki.cern.ch/twiki/bin/viewauth/CMS/ECALDPGHwTimeCalibration>
- [47] CMS Collaboration, *The CMS ECAL performance With examples*, *JINST* 9 C02008, 2014.
- [48] Daniele Del Re for CMS Collaboration, *Timing performance of the CMS electromagnetic calorimeter and prospects for the future.*, CMS-CR-2014/074
- [49] CMS-DP-2014/011: *ECAL Timing Performance Run1*
- [50] <https://twiki.cern.ch/twiki/bin/view/CMSPublic/EcalDPGResultsCMSDP2014011>
- [51] <https://twiki.cern.ch/twiki/bin/view/CMSPublic/EcalDPGResultsCMSDP2014012>
- [52] Florian Beaudette (the CMS Collaboration), *The CMS Particle Flow Algorithm*, arXiv:1401.8155 [hep-ex].
- [53] CMS Collaboration, *Particle-Flow Event Reconstruction in CMS and Performance for Jets, taus and  $\cancel{E}_T$*  CMS Physics Analysis Summary CMS-PAS-PFT-09-001(2009).
- [54] CMS Collaboration, *Jet Performance in pp Collisions at  $\sqrt{S} = 7$  TeV*, CMS PAS JME-10-003 (2010).

- [55] CMS Collaboration, *8 TeV Jet Energy Corrections and Uncertainties based on 19.8  $fb^{-1}$  of data in CMS*, CMS-DP-2013-033 ; CERN-CMS-DP-2013-033, *Jet Energy Corrections and Uncertainties*, CMS Public Note CMS-DP-2012/012.
- [56] CMS Collaboration, *Missing Transverse Energy Performance in Minimum-Bias and Jet Events from Proton-Proton Collisions at  $\sqrt{s} = 7$  TeV*, CMS Physics Analysis Summary CMS-PAS-JME-10-004 (2010).
- [57] CMS Collaboration, *Missing transverse energy performance of the CMS detector*, arXiv:1106.5048v1., Missing Transverse Energy, JINST ,arXiv:1106.5048.
- [58] *Characterization and treatment of anomalous signals in the CMS Electromagnetic Calorimeter* CMS AN AN-10-357.
- [59] *Mitigation of Anomalous APD signals in the CMS ECAL*,2013, JINST 8 C03020, W.Bialas and D.A. Petyt.
- [60] CMS Collaboration,*Determination of Jet Energy Scale in CMS with pp collisions at  $\sqrt{S} = 8$  TeV*, JME-10-010(2012).
- [61] “<https://twiki.cern.ch/twiki/bin/viewauth/CMS/EGamma2012>.”
- [62] CMS Collaboration, *Search for ADD Extra-dimensions with Photon + MET signature*, AN-11-319(2011).
- [63] *Parton distributions for the LHC*, Eur.Phys.J C63(2009) 189-285 or arXiv:0901.0002.
- [64] *Presentation of search results: the CLs technique*,A L Read 2002 J. Phys. G: Nucl. Part. Phys. 28 2693.
- [65] *Computation of confidence levels for search experiments with fractional event counting and the treatment of systematic errors*, Peter Bock JHEP01(2007)080.
- [66] <https://twiki.cern.ch/twiki/bin/viewauth/CMS/>
- [67] *Asymptotic formulae for likelihood-based tests of new physics*,G. Cowan et al, arXiv:1007.1727v3.

## Appendix A

# Glossary and Acronyms

Care has been taken in this thesis to minimize the use of jargon and acronyms, but this cannot always be achieved. This appendix defines jargon terms in a glossary, and contains a table of acronyms and their meaning.

### A.1 Glossary

- **Cosmic-Ray Muon (CR  $\mu$ )** – A muon coming from the abundant energetic particles originating outside of the Earth’s atmosphere.
- **SUSY** – A theoretical model based on a fundamental symmetry called supersymmetry in which the fermions and bosons can exchange their spin, extending the standard model to account for the stability in the observed Higgs boson mass and to also predicting the existence of many extra new particles which could be candidates of dark matter.
- **CMS Coordinate System** – CMS uses a right-handed coordinate system, with the origin at the nominal interaction point, the  $x$ -axis pointing to the center of the LHC, the  $y$ -axis pointing up (perpendicular to the LHC plane), and the  $z$ -axis along the counterclockwise-beam direction. The polar angle,  $\theta$ , is measured from the positive  $z$ -axis and the azimuthal angle,  $\phi$ , is measured in the  $x$ - $y$  plane.
- **Eta** –

$$\eta = -\ln \tan(\theta/2) \tag{A.1}$$

- **Transverse Energy and Momentum** – The transverse energy and momentum are defined as

$$E_T = E \sin \theta \quad (\text{A.2})$$

$$p_T = p \sin \theta \quad (\text{A.3})$$

where  $p$  is the momentum measured in the tracking system and  $E$  is the energy measured in the calorimeters.

- **Missing Transverse Energy** or  $E_T^{\text{miss}}$

$$E_T^{\text{miss}} = \left| - \sum_i E_T^i \vec{n}_i \right| \quad (\text{A.4})$$

where  $\vec{n}_i$  is a unit vector that points from the interaction vertex to the transverse plane.

## A.2 Acronyms

Table A.1: Acronyms

LLNP	Long-Lived Neutral Particle.
DM	Dark Matter.
DE	Dark Energy.
SM	Standard Model
BSM	Beyond Standard Model
SUSY	Supersymmetry
GMSB	Gauge Mediated Supersymmetry Breaking
LHC	Large Hadron Collider
CMS	Compact Muon Solenoid
CR $\mu$	Cosmic-Ray Muon

## A.3 Analysis How To and Data Samples

### A.3.1 Check Out Software Packages

To check out the analysis packages, do the following steps:

- `cmsrel CMSSW_5_3_29`
- `cd CMSSW_5_3_29\src`

### A.3.2 Data Samples

In Table A.2 show the data samples and the corresponding integrated luminosity.

The *jason* file with the list of certified good luminosity sections is

`Cert_8TeVPromptReco_Collisions12_JASON.txt`.

Data Sample	Recorded Luminosity [ fb <sup>-1</sup> ]
/Run2012B/SinglePhoton/ EXODisplacedPhoton-PromptSkim-v3	5.1
/Run2012C/SinglePhoton/ EXODisplacedPhoton-PromptSkim-v3	6.9
/Run2012D/SinglePhoton/ EXODisplacedPhoton-PromptSkim-v3	7.1
/SingleElectron/Run2012A-22Jan2013-v1/AOD	5.2
/DoubleElectron/Run2012C-22Jan2013-v1/AOD	4.8

Table A.2: Data samples and their corresponding integrated luminosity totaling 19.1 fb<sup>-1</sup> used in the our delayed photon search analysis